SEARCH FOR SUPERSYMMETRY IN JET TOPOLOGIES WITH THE CMS DETECTOR

A THESIS SUBMITTED TO
THE GRADUATE SCHOOL OF NATURAL AND APPLIED SCIENCE
OF
MIDDLE EAST TECHNICAL UNIVERSITY

BY

KADİR ÖCALAN

IN PARTIAL FULFILLMENT OF THE REQUIREMENTS
FOR
THE DEGREE OF MASTER OF SCIENCE
IN
PHYSICS

FEBRUARY 2009

Approval of the thesis:

SEARCH FOR SUPERSYMMETRY IN JET TOPOLOGIES WITH THE CMS DETECTOR

submitted by **KADİR ÖCALAN** in partial fulfillment of the requirements for the degree of **Master of Science in Physics Department, Middle East Technical University** by,

Prof. Dr. Canan Özgen
Dean, Graduate School of **Natural and Applied Sciences**

Prof. Dr. Sinan Bilikmen
Head of Department, **Physics**

Assoc. Prof. Dr. Ali Murat Güler
Supervisor, **Physics Department, METU**

Examining Committee Members:

Prof. Dr. Ali Ulvi Yılmazer
Physics Engineering Dept., Ankara University

Assoc. Prof. Dr. Ali Murat Güler
Physics Dept., METU

Prof. Dr. Ramazan Sever
Physics Dept., METU

Prof. Dr. Gürsevil Turan
Physics Dept., METU

Prof. Dr. Osman Yılmaz
Physics Dept., METU

Date:

I hereby declare that all information in this document has been obtained and presented in accordance with academic rules and ethical conduct. I also declare that, as required by these rules and conduct, I have fully cited and referenced all material and results that are not original to this work.

Name, Last Name: KADİR ÖCALAN

Signature :

ABSTRACT

SEARCH FOR SUPERSYMMETRY IN JET TOPOLOGIES WITH THE CMS DETECTOR

Öcalan, Kadir
M.S., Department of Physics
Supervisor : Assoc. Prof. Dr. Ali Murat Güler

February 2009, 119 pages

Supersymmetry (SUSY) is the most motivated scenario beyond the Standard Model (SM) addressing the problems of the SM in an elegant way by establishing a symmetry which relates matter particles to interaction particles and vice versa. The simplest phenomenologically viable supersymmetric theory is the Minimal Supersymmetric Standard Model (MSSM) which can be accommodated to minimal Supergravity (mSuGra) theory in order to both take gravity into account and constrain its parameter space. CMS detector is one of the general purpose detectors constructed at LHC (Large Hadron Collider) which targets to search for SUSY signal. This thesis presents a search strategy for SUSY in three different fully hadronic jet topologies with the CMS detector. Di-jet, 3-jet, and 4-jet event topologies offer clear signatures for SUSY searches and the key SUSY decay modes of these jet topologies appear to be squark pair production, squark-gluino production, and gluino pair production, respectively. In these jet topologies, an important kinematical variable named alpha, α is used to separate SUSY signal test points from the SM background events including QCD, EWK (Electroweak), and invisible decay of Z boson processes. Alpha variables are found to be very useful in terms of enhancing SUSY signal while rejecting all QCD events. Discriminating power of alpha variables are shown in terms of signal-to-background and signal significance calculations and the results are found to be promising which further encourage searches for SUSY signal in jet event topologies with the early CMS data at 1 fb^{-1} integrated luminosity.

Keywords: CMS detector, Supersymmetry, Di-jet topology, 3-jet and 4-jet topologies

ÖZ

CMS DEDEKTÖRÜYLE JET TOPOLOJİLERİNDE SÜPERSİMETRİ ARANMASI

Öcalan, Kadir
Yüksek Lisans, Fizik Bölümü
Tez Yöneticisi : Doç. Dr. Ali Murat Güler

Şubat 2009, 119 sayfa

Standard Model (SM) ötesi modellerden biri olan Süpersimetri (SUSY), SM içerisinde yer alan sorunlara madde parçacıkları ve etkileşim parçacıkları arasında simetri kurarak zarif çözümler getirmektedir. Süpersimetrik modellerde en basit teoriye sahip olan En Küçük Süpersimetrik Standard Model (MSSM), en küçük Süper Yerçekimi (mSuGra) teorisiyle birlikte kullanıldığında yer çekiminin dahil edilmesinin yanısıra parametre sayısına da sınırlama getirmektedir. Diğer yandan, Büyük Hadron Çarpıştırıcısında (LHC) inşa edilmiş olan genel amaçlı dedektörlerden biri olan CMS dedektörü SUSY parametre alanının aranmasını hedeflemektedir. Bu tez, tam hadronik kanallarda üç farklı jet topolojilerini kullanarak CMS dedektörüyle SUSY aranmasına dair bir yöntem sunmaktadır. Di-jet, 3-jet ve 4-jet topolojileri temiz sinyal alanı temin etmekte olup bu topolojiler SUSY bozunum kanalları olarak sırasıyla squark çifti, squark-gluino ve gluino çifti üretimlerine tekabül etmektedir. Bu üç farklı jet topolojilerinde, alpha (α) olarak adlandırılan önemli bir kinematik değişkeni kullanılmakta olup, bu değişken SUSY deneme sinyal noktalarını SM arkaplanı olan QCD, EWK (elektrozayıf) ve Z bozonunun görünmez bozunumu olaylarından ayırt etmek için kullanılmıştır. Alpha değişkenleri SUSY sinyalini yükseltmesi ve bütün QCD olaylarını ortadan kaldırması bağlamında çok kullanışlı oldukları görülmüştür. Alpha değişkenlerinin ayırt etme gücü, sinyalin arkaplana oranı ve sinyal önemi hesaplamalarıyla jet topolojilerinde ortaya konulmuş ve çıkan sonuçlar umut verici olarak bulunmuş olup SUSY sinyalinin jet topolojilerinde erken CMS verileriyle, özellikle 1 fb^{-1} lüminosite değerinde aranmasını teşvik etmiştir.

Anahtar Kelimeler: CMS dedektörü, Süpersimetri, Di-jet topolojisi, 3-jet ve 4-jet topolojileri

to my father, mother, and sisters

ACKNOWLEDGMENTS

I would like to acknowledge that this thesis would not have been possible without the help and support of many special people around me, to only some of whom it is possible to give particular mention here.

I would like to express profound gratitude to my supervisor, Assoc. Prof. Dr. Ali Murat GÜLER for his moral support, continuous guidance, teaching me a great deal of knowledge for my research interest, and his trust in me. I have been amazingly fortunate to have such a supervisor who gave me the freedom to explore on my own, and at the same time the guidance to recover when my steps faltered. His patience and support helped me overcome many difficulties.

I would like to thank my CERN project manager, Prof. Dr. Ramazan SEVER. He has been always there to listen and give advice. I am deeply grateful to him for the helps and supports whenever I needed.

I indebted to the members of the CMS Collaboration SUSY group with whom I have interacted during the course of my research studies. Particularly, I would like to thank Henning Flaecher (CERN) from him I learned many things and he helped me to understand my research interests better. I am grateful to Markus Stoye (Imperial College, London) for the helps concerning the implementation of SUSY PAT algorithm that much of my research was based on. I am also grateful to Tanja Rommerskirchen (University of Zürich) for useful discussions during my research. I have special thanks to my dear friend Benjamin Sinclair (CERN) for his helps throughout scripting-coding and continuous friendship when I was alone at CERN. My sincere thanks to the CMS Collaboration SUSY group convener, Oliver Buchmuller (CERN) for his motivation and support whenever I needed.

My special thanks go to the convener of Fermilab LPC (LHC Physics Center) di-jet topology convener, Jane Nachtman (University of Iowa) for providing me support and valuable feedbacks that shaped my thesis in the early stages of my research.

Many special friends have helped me stay sane through difficult years of my master education. M. Fatih BAY (University of Bern) for his endless friendship and being always ready to offer solutions to my problems, Serhan TUFANLI (METU) for his continuous friendship, and Ferhat ÖZÖK (İstanbul University) for his friendship at CERN. Their support and care helped me overcome setbacks and stay focused on my graduate study. I greatly value their friendships and deeply appreciate their belief in me.

Most importantly, not only my thesis but also the whole life of me would not have been possible without the love, support, and patience of my family. My family to whom this thesis is dedicated to, has been a constant source of love, concern, support and strength for my life. I would like to express my heart-felt gratitude to my father, my mother, and my sisters: Sermin ÖCALAN, Seval ORHAN, and Serpil OKTAY.

TABLE OF CONTENTS

CHAPTERS

APPENDICES

LIST OF TABLES

TABLES

LIST OF FIGURES

FIGURES

CHAPTER 1

INTRODUCTION

This thesis presents a search strategy for Supersymmetry (SUSY) in fully hadronic jet channels with the CMS (Compact Muon Solenoid) detector at LHC (Large Hadron Collider). The chapters of the thesis are organized in such a way to begin with reviewing the Standard Model (SM) of Elementary Particle Physics. Following the descriptions of the theories which contribute to the basis of the SM theory, the limitations to the SM are linked to the need of SUSY and hence to SUSY theory. SUSY theory is explained in terms of its algebra, particle content, and accompanying submodels. Following the description of SUSY, CMS experiment is presented in terms of its subdetector systems and the computing model. In order to understand the analysis chapters of this thesis, an introductory chapter is developed in which analysis algorithm, data samples, and SUSY triggers are presented. In the analyses chapters, the analysis results for di-jet, 3-jet, and 4-jet event topologies are presented. The contents of the chapters of this thesis can be given in detail.

In Chapter 2, particle content of the SM including both fermionic and bosonic sectors are summarized. Quantum Electrodynamics (QED), Electroweak (EWK), and Quantum Chromodynamics (QCD) theories are reviewed in terms of their lagrange equations. The lagrange equations enabled gaining a better insight into the SM particles and the interactions among them. The Higgs Mechanism is also reviewed in this chapter in order to explain the origin of the SM particle masses. The limitations to the SM including the hierarchy problem are finally presented in this chapter which encouraged to search for theories beyond.

In Chapter 2, introduction of SUSY as a new theory is given in terms of its algebra. The hierarch problem of the SM is addressed in the context of SUSY. The Minimal Supersymmetric Standard Model (MSSM) is then introduced as being the simplest SUSY submodel which also has theoretical treatments similar to the SM. The MSSM particle content which are supersymmetric particles is given and the interactions governing among the SUSY particles are discussed in terms of the MSSM lagrangian. Soft MSSM lagrangian is given to explore the mechanism which offers masses to supersymmetric particles. Minimal Supergravity model (mSuGra) is then introduced accompanying to the MSSM with its use cases in suppression of the SUSY parameter space and containment of gravity. Among all varieties of the supersymmetric particles, squarks and gluinos have special relevance to the decay channels of the analysis chapters of this thesis are described with their productions and possible decay paths in the CMS experiment.

In Chapter 3, CMS experiment is reviewed as being one of the detectors contructed at LHC. Starting from the LHC overview, physics goals, and its design and operation, the coordinate system and the subdetectors of the CMS detector are explained. The Tracker, The Electromagnetic Calorimeter, The Hadronic Calorimeter, and The Muon System are the major components of the CMS detector overviewed in turn. In addition to the CMS detector subcomponents, The Trigger System is explanied. Finally, in this chapter, The CMS Computing Model is summarized in terms of its tiered architecture for data storage tasks and Worldwide LHC Grid for data transfer and user data analysis tasks.

In Chapter 4, CMS software framework is presented. CMS software framework is introduced as a large collection of software tools necassary for physics analyses. The framework is introduced in two parts which are Core Software and Physics Software. Physics Analysis Toolkit (PAT) is then explained in terms of its layer-by-layer use case, implementation for SUSY analyses, and object cleaning options which has to be used in order to perform Monte Carlo (MC) physics analyses with the CMS detector software framework. And finally, the MC signal and background data samples which are used with SUSY PAT algorithm in this thesis are explained. The data samples are accompanied with necessary SUSY detector triggers which are also presented in this chapter.

In Chapter 5, the MC analysis results concerning the di-jet topology are presented. Starting from the SUSY motivation for this event topology, event kinematics with alpha variables, event selection, and the signal-to-background and signal significance calculations are presented. Alpha variables are demonstrated to be enhancing SUSY signal against the SM background processes including QCD, EWK, and invisible decay of Z boson. Both normal alpha and transverse alpha variables are shown to have two regions, one is signal enriched in which alphas are greater than 0.55 and the other one is signal depleted region in which alphas are smaller than 0.55 with many SM events. Promising analysis results are supported with the cut flows applied on alpha variables. The results presented in this chapter with di-jet event topology inspired the extension of di-jet case to multijet systems.

In Chapter 6, extensions of di-jet event topology to 3-jet and 4-jet event topologies are considered for the searches of SUSY. These two event topologies differ from di-jet case with definitions of alpha variables and hence their kinematics. SUSY motivations for these decay topologies are given in terms of related SUSY squark and gluon decay channels. Analysis results are shown to be encouraging in terms of signal-to-background and signal significance calculations which are also presented in related tables of this chapter. This chapter also motivates SUSY searches with CMS detector in multijet event topologies.

In Chapter 7, summaries of the analyis results of the three different jet topologies presented in Chapter 5 and Chapter 6 are given. Starting from the di-jet case, discrimination power of alpha variables in terms of their cut flows are revisited. In a similar manner, the cut flows of alpha variables which are calculated for 3-jet and 4-jet cases are revisited in order to imply that alpha variables give promising results for the searches of SUSY with CMS detector. Additionaly, other SUSY signal points are summarized for the jet topologies in order to show how likely they are to be discovered with the CMS detector.

In Appendices, event selector libraries of SUSY PAT algorithm and their corresponding variables are given. CMS collaboration MC data skims and available trigger paths are included. And finally, the kinematics of alpha variable which is used with di-jet topology is explored.

CHAPTER 2

THEORY AND MOTIVATION

2.1 The Standard Model

The Standard Model (SM) of Elementary Partice Physics is the most precise and satisfying model to explain particles and their interactions with a high degree of precision. The SM is a quantum field theory which describes the unification of electromagnetic interaction and weak interaction into an electroweak (EWK) sector, and includes a Quantum Chromodynamics (QCD) sector for the description of the strong interactions. However, the SM cannot be an ultimate theory to describe particles and their interactions, since there are some limitations to the model that will be shown later.

2.1.1 The SM Content

The fermionic sector (matter particles) of the SM consists of three families (generations) of quarks and leptons as shown in Table 2.1 with their properties. Furthermore, the bosonic sector (force carriers) of the SM consists of different gauge bosons being responsible of three of the four main forces present in nature, as shown in Table 2.2. The gravity is the force not included in the SM framework which encourages for searches of theories beyond.

In addition to the elementary particles sector of the SM which are fermions and gauge bosons, collections of quarks and anti-quarks form other, composite particles known as hadrons. Hadrons are divided into mesons and baryons: mesons (including pions, kaons, and so on) comprise a quark and an anti-quark; baryons (including the proton and the neutron) are three quark states.

The SM is based on the gauge symmetry group $SU(3)_C \otimes SU(2)_L \otimes U(1)_Y$. Every group has a coupling constant associated with: g_s (related with α_s) for the strong interactions, g (related with the Fermi constant G_F) for the weak interactions and g' (related with electric charge e) for the electromagnetic interactions.

Many useful books explaining the SM in detail can be found elsewhere ([1], [2], [3], and [4]). In the following subsections, the different theories that contribute to the basis of the SM are explained briefly.

Table 2.1: Fermionic sector ($spin - \frac{1}{2}$) of the SM. Masses without uncertanities are shown based on the evaluations of the Particle Data Group (PDG) [5]. The elementary charge, e, equals to 1.602×10^{-19} C which should not be confused with the representation of the electron, e.

Fermions	$1^{st} family$	$2^{nd} family$	$3^{rd} family$
Quarks	up(u)	charm (c)	top (t)
	m_u= 2.55 MeV	m_c=1.27 GeV	m_t=171.2 GeV
	$q_u = \frac{2e}{3}$	$q_c = \frac{2e}{3}$	$q_t = \frac{2e}{3}$
	down(d)	strange (s)	bottom (b)
	m_d= 5.04 MeV	m_s=104 MeV	m_b=4.20 GeV
	$q_d = -\frac{e}{3}$	$q_s = -\frac{e}{3}$	$q_b = -\frac{e}{3}$
Leptons	electron(e)	muon (μ)	tau (τ)
	m_e= 0.511 MeV	m_μ=105.66 MeV	m_τ=1776.84 MeV
	$q_e = -e$	$q_\mu = -e$	$q_\tau = -e$
	e neutrino (ν_e)	μ neutrino (ν_μ)	τ neutrino (ν_τ)
	$m_{\nu_e} < 2$ eV	$m_{\nu_\mu} < 0.19$ MeV	$m_{\nu_\tau} < 18.2$ MeV
	$q_{\nu_e} = 0$	$q_{\nu_\mu} = 0$	$q_{\nu_\tau} = 0$

Table 2.2: Gauge bosons ($spin$-1) of the SM with their corresponding masses and interactions they appear in.

Gauge Bosons	Mass	Interaction
gluon (g)	0	strong (color) $SU(3)_C$
photon (γ)	0	electromagnetic $U(1)_{em}$
neutral weak boson (Z)	91.1876 GeV	weak neutral
charged weak bosons ($W^{\pm}$)	80.398 GeV	weak charged

2.1.2 Quantum Electrodynamics

Quantum Electrodynamics (QED) was developed in the late 1940s and early 1950s chiefly by Richard P. Feynman, Julian Schwinger, and Sin-Itiro Tomonaga; to describe the electromagnetic interactions of electrons and photons. This is a quantum renormalisable theory which is invariant under a change of phase or gauge, *k(x)*;

$$\Psi(x) \rightarrow \Psi'(x) = e^{iQk(x)}\Psi(x), \tag{2.1}$$

where *Q* is the charge operator (with eigenvalue -1 for the electron), *k(x)* is a function which depends on space and time, and $\Psi(x)$ is the Dirac field (spin-$\frac{1}{2}$ fermions).

In order to promote the global symmetry under *U(1)* transformations, responsible for the conservation of the charge to a local one (*k(x)* would be constant for global transformation), the covariant derivative needs to be introduced:

$$D_\mu \equiv \partial_\mu + iQA_\mu, \tag{2.2}$$

where $\partial_\mu = (\frac{\partial}{\partial t} \cdot \nabla)$ (while, $\partial^\mu = (\frac{\partial}{\partial t} \cdot -\nabla)$) and A_μ is a gauge field satisfying

$$A_\mu \rightarrow A'_\mu \equiv A_\mu + \frac{1}{e}\partial_\mu k, \tag{2.3}$$

Then, the lagrangian can be written in a compact form as

$$L = \overline{\Psi}(i\gamma^\mu D_\mu - m)\Psi = \overline{\Psi}(i\gamma^\mu \partial_\mu - m) - L_I, \tag{2.4}$$

where m is a mass of $spin-\frac{1}{2}$ fermion in free space and γ^μ is known as *four Dirac matrices* to simplify construction of lagrangian in a contravariant form and the last term in the lagrangian corresponds to the interaction between the new field, A_μ and Dirac particle (charge *-e*) (or electromagnetic current density, $j^\mu = -e\overline{\Psi}\gamma^\mu\Psi$):

$$L_I = -e(\overline{\Psi}i\gamma^\mu\Psi)A_\mu. \tag{2.5}$$

In addition, the kinetic energy of the new fields needs to be introduced. From Maxwell's equations, the kinetic term will be of the form [6]:

$$L_K = -\frac{1}{4}F_{\mu\nu}F^{\mu\nu}, \tag{2.6}$$

field strength tensors are $F_{\mu\nu} \equiv \partial_\mu A_\nu - \partial_\nu A_\mu$ and $F^{\mu\nu} \equiv \partial^\mu A^\nu - \partial^\nu A^\mu$.

So one can end up with the lagrangian describing QED as

$$L_{QED} = \overline{\Psi}(i\gamma^{\mu}\partial_{\mu} - m)\Psi - \frac{1}{4}F_{\mu\nu}F^{\mu\nu} + e\overline{\Psi}\gamma^{\mu}A_{\mu}\Psi. \tag{2.7}$$

Here, Ψ and $\overline{\Psi}$ represent electron and positron (anti-particle of electron) fields respectively. The first term in the lagrangian, is known as *electron propogator* describing an electron (or a positron) travelling freely in space. The second term generates a particle travelling through free space, in this case, this is the photon, the quantum of the electromagnetic field. As opposed to the first term, the second term do not have mass, m, indicating that the photon must be massless. Finally, the third term represents an interaction (coupling) between photon field and electron and positron fields as in the case of one electron annihilating one photon ($e^-e^+ \rightarrow e^-e^+$, $e^-e^- \rightarrow e^-e^-$, and so on).

Thus, the electromagnetic interaction is described by two quantum fields: one for the charged particles and one for the photon in QED. The strength of the interaction is usually described by the coupling constant α_{em} whose value depends on the momentum transfer q^2 in an interaction. For $q^2 \rightarrow 0$ (at low energies), the coupling constant value is that of the fine structure constant, $\alpha_{em} = \frac{e^2hc}{4\pi} = \frac{1}{137}$. At the scale of the Z boson, its value increases: $\alpha_{em}(m_Z) \approx \frac{1}{128}$.

2.1.3 Electroweak Theory

The weak theory was proposed by Enrico Fermi in 1934 in order to explain neutron β-decay. In this theory, four fermions directly interacted with one another in such a way that a neutron (or a down-quark) could be directly separated into an electron, an anti-neutrino, and a proton (an up-quark). The strength of the Fermi's interaction is given by the Fermi constant, G_F.

Though Feynman diagrams described the interaction well at tree level, loop diagrams cannot be calculated since Fermi's interaction was not renormalisable. The solution came in 1967 when the electromagnetic and weak interactions were unified by Sheldon Lee Glashow, Abdus Salam, and Steven Weinberg [7]. This unification formed the electroweak theory (EWK) which became the core of the SM. The idea of this unification is to incorporate both interactions into a single theoretical framework in which they would appear as two manifestations of the same fundamental interactions. These interactions are unified under the group of $SU(2)_L \otimes U(1)_Y$, where the subscript L is a reminder that *SU(2)* group couples only left-handed fermions and the subscript Y, which will be given in Eq. 2.18, is to remind that *U(1)* group couples to weak *hypercharged* particles. The first part of the group has dimension of three such that three generators are needed: $t_i = \frac{\sigma_i}{2}$ (i=1, 2, and 3), where σ_i are the Pauli matrices. These generators, due to the global gauge invariance under *SU(2)*, introduce a new quantum number called the weak isospin, *T*. This number is given to different spin-like multiplets. Since weak force only interacts with left-handed particles (right-handed antiparticles), the left-handed fermions transform as doublets while the right-handed ones transform as singlets [6]:

$$f_L^i = \begin{pmatrix} \nu_L^i \\ l_L^i \end{pmatrix}, \begin{pmatrix} u_L^i \\ d_L^i \end{pmatrix}, \tag{2.8}$$

$$f_R^i = l_R^i, u_R^i, d_R^i, \tag{2.9}$$

where i=1, 2, and 3 corresponds to family index. Hence the weak interaction divided into a charged part (that is, exchanging the components of the doublet) and a neutral part (that is, leaving the doublets as they are). Since *SU(2)* is a *non-Abelian* group, it allows self-interactions of these gauge fields.

The structure of the group of $U(1)_Y$ is more simple with only one generator called the hypercharge operator, $\hat{Y}$. Once the $SU(2)_L \otimes U(1)_Y$ group is defined, the standard model EWK lagrangian is obtained by requiring invariance under local gauge transformations to obtain an interacting field theory, following the analogy with QED. This can be achieved by replacing the derivatives of the fields by the corresponding covariant derivative, which now has the form:

$$D_\mu \equiv \partial_\mu - ig\overrightarrow{T} \cdot \overrightarrow{W}_\mu - ig'\frac{Y}{2}B_\mu, \tag{2.10}$$

where $\overrightarrow{W}_\mu$ and g are vector gauge field and coupling constant corresponding to $SU(2)_L$ and B_μ and g' are scalar gauge field and coupling constant referring to $U(1)_Y$, respectively.

Then, the EWK lagrangian can be written as:

$$L_{EWK} = L_f + L_G + L_{SSB} + L_{YW}, \tag{2.11}$$

The first term in the lagrangian corresponds to fermions (matter particles) and can be expressed in a compact form of [8]:

$$L_f = i(\bar{l}_L \mathfrak{D} l_L + \bar{e}_R \mathfrak{D} e_R + \overline{Q}_L \mathfrak{D} Q_L + \bar{u}_R \mathfrak{D} u_R + \bar{d}_R \mathfrak{D} d_R), \tag{2.12}$$

where the new covariant derivative, $\mathfrak{D} = \gamma^{\mu} D_{\mu}$. In addition, l_L is the left-handed lepton doublet, e_R is the right-handed charged lepton singlet, Q_L is the left-handed quark doublet and u_R and d_R are the right-handed quark singlets in each of the three generations.

The second term in the EWK lagrangian comes from the contributions of gauge fields:

$$L_G = -\frac{1}{4}(W^i_{\mu\nu} W^{\mu\nu}_i + B_{\mu\nu} B^{\mu\nu}) + L_{GF} + L_{FP}, \tag{2.13}$$

where $W^i_{\mu\nu}$ (with i=1, 2, 3) and $B_{\mu\nu}$ are, respectively, the field strength tensors for $SU(2)_L$ and $U(1)_Y$ defined as:

$$W^i_{\mu\nu} \equiv \partial_\mu W^i_\nu - \partial_\nu W^i_\mu + g\epsilon^{ijk} W^j_\mu W^k_\nu, \tag{2.14}$$

$$B_{\mu\nu} \equiv \partial_\mu B_\nu - \partial_\nu B_\mu, \tag{2.15}$$

and and L_{GF} and L_{FP} are *the gauge mixing* and *Faddeev Popov* lagrangians, respectively which are explained in [9].

The last two terms of the EWK lagrangian (Eq. 2.11) are the symmetry breaking sector and the Yukawa lagrangian, respectively, which will be described in the next subsection.

The gauge fields presented at Eq. 2.14 and Eq. 2.15 can be combined in the forms of:

$$\begin{aligned} W^\pm_\mu &= \frac{1}{\sqrt{2}}(W^1_\mu \mp W^2_\mu), \\ Z_\mu &= cos\theta_w W^3_\mu - sin\theta_w B_\mu, \\ A_\mu &= sin\theta_w W^3_\mu + cos\theta_w B_\mu, \end{aligned} \tag{2.16}$$

where, A_μ represents the photon field as it was in QED, θ_w is the weak mixing angle with $cos\theta_w = \sqrt{\frac{g}{g^2+g'^2}}$, and $tan\theta_w$ which relates both couplings by a simple relation as $tan\theta_w = \frac{g'}{g}$. In addition, $W^\pm_\mu$ and Z_μ fields are associated to the physical $W^\pm$ and Z^0 boson particles. In this framework, the elementary charge, $e = gsin\theta_w$ and the Fermi constant can be written through the following relation:

$$G_F = \frac{\sqrt{2}}{8}\frac{g^2}{m_w^2}, \tag{2.17}$$

The electric charge q, the third component of the weak isospin, T_3, and the hypercharge Y are linearly related by the Gell-Mann Nishijima formula:

$$q = T_3 + \frac{Y}{2}. \tag{2.18}$$

Therefore, the global and local conservation of weak isospin and hypercharge naturally implies charge conservation, as required by QED, and the electromagnetic and the weak interactions are unified under the same theoretical framework in this theory.

2.1.4 The Higgs Mechanism

In the previous subsection, it was shown that the SM formalism achieves the unification of electromagnetic and weak interactions through a local gauge symmetry. Nevertheless, this gauge symmetry requires massless $W^{\pm}$ and Z^0 bosons. This requirement is in contradiction with the observation and one needs to introduce a mechanism for generating non-zero masses while keeping the renormalisability of the theory. In the SM, the Higgs mechanism of Spontaneous Symmetry Breaking (SSB) is proposed.

In the SSB, one introduces a new field, the Higgs field, such as:

$$\Phi = \begin{pmatrix} \varphi^+ \\ \varphi^0 \end{pmatrix}. \tag{2.19}$$

This is the so-called Higgs doublet, wherein φ^+ and φ^0 are charged scalar complex and neutral scalar complex fields, respectively.

The corresponding kinetic and potential terms of the SSB lagrangian (or the Higgs lagrangian) that appeared in Eq. 2.11 have the form:

$$L_{SSB} = (D_\mu \Phi)^\dagger (D^\mu \Phi) - V(\Phi), \tag{2.20}$$

where D_μ defined before in Eq. 2.10 and $V(\Phi)$ is the Higgs potential:

$$V(\Phi) = \mu^2 \Phi^\dagger \Phi + \lambda (\Phi^\dagger \Phi)^2. \tag{2.21}$$

If $\lambda > 0$ and $\mu^2 < 0$, the potential $V(\Phi)$ has a minimum for [6]:

$$\Phi^\dagger \Phi = -\frac{\mu^2}{2\lambda} \equiv \frac{v^2}{2}. \tag{2.22}$$

In Quantum Field Theory, the minimum of the potential corresponds to *the vacuum* which is the lowest energy state, and the quantized excitations of each field above the vacuum correspond to particle states. Fermion fields and boson fields (which carry non-zero spins) and charged scalar fields must have zero value in the vacuum. On the other hand, neutral scalar fields, which do not have electric charge, can have a non-zero value in vacuum, which is called *vacuum expectation value* or *VEV*. From the Eq. 2.22, the field Φ has a non-zero vacuum expectation value: $\langle 0|\Phi|0\rangle = \frac{v}{\sqrt{2}} \neq 0$ which implies choosing one of a set of degenerate states of minimum energy breaks the gauge symmetry. The vacuum expectation value of the scalar field, $\langle\Phi\rangle$ is fixed by the low energy effective Fermi theory:

$$v = (\frac{1}{\sqrt{2}G_F})^{\frac{1}{2}} = 246GeV \tag{2.23}$$

which sets the electroweak symmetry breaking scale.

In order to derive physical properties of the particles resulting from spontaneous symmetry breaking, the Higgs doublet can be written conveniently as

$$\Phi = \frac{1}{\sqrt{2}} exp(\frac{i}{2v}\overrightarrow{\xi} \cdot \overrightarrow{\sigma}) \begin{pmatrix} 0 \\ v + H \end{pmatrix}, \tag{2.24}$$

where $\overrightarrow{\xi} = \xi_1$, ξ_2, and ξ_3 and H are four real scalar fields. The H describes the physical Higgs boson, obtained by the excitations of the neutral Higgs field above the vacuum. On the other hand, the massless scalar fields $\overrightarrow{\xi}$ are not physical fields, they can be rotated away by a gauge transformation. These three massless scalar fields are as a result known as *Goldstone theorem*.

The gauge transformation which eliminates the massless scalar fields, $\overrightarrow{\xi}$, is known as *unitary gauge*. So one can end up with the Higgs doublet in the unitary gauge as

$$\Phi = \frac{1}{\sqrt{2}} \begin{pmatrix} 0 \\ v + H \end{pmatrix}. \tag{2.25}$$

Thus, the SSB lagrangian which is given in Eq. 2.20, now reads

$$\begin{aligned} L_{SSB} = \frac{1}{2}(\partial H)^2 - \lambda v^2 H^2 - \lambda v H^3 - \frac{\lambda}{4}H^4 + \frac{g^2 v^2}{4} W_\mu^\dagger W^\mu + \frac{g^2 v^2}{8cos^2\theta_w} Z_\mu Z^\mu \\ + \frac{g^2 v}{2} W_\mu^\dagger W^\mu H + \frac{g^2 v}{4cos^2\theta_w} Z_\mu Z^\mu H \\ + \frac{g^2}{4} W_\mu^\dagger W^\mu H^2 + \frac{g^2}{8cos^2\theta_w} Z_\mu Z^\mu H^2. \end{aligned} \tag{2.26}$$

The first term on the right-hand side is the kinetic term for the Higgs boson. The second term is the mass term, from which mass of the Higgs boson can be given by

$$m_H = \sqrt{2\lambda v^2} = \sqrt{-2\mu^2}. \tag{2.27}$$

Negative parameter, μ^2 is not predicted by the SM giving the value of the Higgs mass.

The third and fourth terms on the right-hand side of the SSB lagrangian generate trilinear and quadrilinear self couplings of the Higgs field. The fifth and sixth terms on the right-hand side are remarkably important, since they are mass terms of W and Z gauge bosons. From the SSB lagrangian, the masses of W and Z bosons appear to be

$$m_W = \frac{gv}{2} \tag{2.28}$$

and

$$m_Z = \frac{gv}{2cos\theta_w}. \tag{2.29}$$

These two equations enable the SM to make a useful prediction:

$$\frac{m_W^2}{m_Z^2} = cos^2\theta_w. \tag{2.30}$$

The last four terms on the right-hand side of Eq. 2.26 generate trilinear and quadrilinear couplings of the Higgs field with the gauge bosons.

In addition to the masses of W and Z gauge bosons, the mass of fermions are generated as a result of the Higgs mechanism through the presence of Yukawa couplings of the Fermion fields with the Higgs doublet. Then , the last term, which is L_{YW} in Eq. 2.11 can be written in two parts: the Higgs-lepton Yukawa lagrangian and the Higgs-quark Yukawa lagrangian as

$$L_{YW} = L_{YW,L} + L_{YW,Q}. \tag{2.31}$$

The Higgs-lepton Yukawa lagrangian can be written in the unitary gauge as

$$L_{YW,L} = -\sum_{i=e,\mu,\tau} \frac{y_i v}{\sqrt{2}} \bar{l}_i l_i - \sum_{i=e,\mu,\tau} \frac{y_i}{\sqrt{2}} \bar{l}_i l_i H, \tag{2.32}$$

where l_i are the charged lepton fields ($l_i = l_{iL} + l_{iR}$) with definite masses and the first term of the Higgs-lepton Yukawa lagrangian is the mass term for the charged leptons, whose masses are given by

$$m_i = \frac{y_i v}{\sqrt{2}}. \tag{2.33}$$

Since the Yukawa couplings, y_e,y_μ, and y_τ are unknown parameters of the SM, the masses of the charged leptons are not predicted and must be obtained from experimental measurements. On the other hand, a fermion mass term must include both left-handed and right-handed fields, so it is clear that neutrinos which are not charged leptons and their fields do not have right-handed component are indeed massless in the SM. This shows that neutrinos do not couple to the Higgs field in the SM.

The second term on the right-hand side of the Eq. 2.32 shows that the trilinear couplings between the charged leptons and the Higgs boson are proportional to the charged lepton masses.

In a similar manner to the Higgs-lepton Yukawa lagrangian, the Higgs-quark Yukawa lagrangian can be written in the unitary gauge as

$$L_{YW,Q} = -(\frac{v+H}{\sqrt{2}})(\overline{Q'^{D}_{L}} Y'^{D} Q'^{D}_{R} + \overline{Q'^{U}_{L}} Y'^{U} Q'^{U}_{R}) + h.c., \tag{2.34}$$

where Y'^U and Y'^D are Yukawa matrices, Q_L and Q_R are left-handed and right-handed quark fields. Here, the superscripts U and D refer to u,c,t and d,s,b quarks respectively. The choice of primes in the Higgs-quark Yukawa lagrangian is to draw attention to the need of further diagonalization of Yukawa matrices and quark fields.

Hence, the terms proportional to v in the lagrangian are the mass terms for the quarks.

2.1.5 Quantum Chromodynamics

Quantum Chromodynamics (QCD) [10] was developed in 1973 to describe the behavior of quarks being hold together by strong force carried by gluons. Again, quantum field theory is the framework in which QCD is developed. In this case, the color group $SU(3)_C$ is the starting global symmetry. This new quantum number (color) is introduced to refer three possible states of the quarks and it constitutes an exact symmetry (the particular color of the quarks is not affecting the dynamics of a process). In order to promote global symmetry to a local one, the covariant derivatives of the fields take the form:

$$D_\mu q \equiv (\partial_\mu - i g_s (\frac{\lambda_\alpha}{2}) G^\alpha_\mu) q, \tag{2.35}$$

where g_s is the strong coupling constant, although this name is usually used for references to α_s since there is a direct relationship between them: $g_s^2 \equiv 4\pi\alpha_s$. In addition, $\frac{\lambda_\alpha}{2}$ are the $SU(3)$ generators (Gell-Mann matrices, 3×3 matrices with α=1,2,...,8), G^α_μ are the gluon fields, and q is a vector of three components corresponding to different colors.

The QCD lagrangian is written in terms of the quarks, their covariant derivatives, and the kinetic term for the gluon fields [6]:

$$L_{QCD} = \sum_{q=flavors} \overline{q}(i\mathfrak{D} - m_q)q - \frac{1}{4}G^{\alpha}_{\mu\nu}G^{\mu\nu}_{\alpha}, \tag{2.36}$$

where $G^{\alpha}_{\mu\nu}$ is the gluon field strength tensor, which unlike the QED case, is given by,

$$G^{\alpha}_{\mu\nu} = \partial_{\mu}G^{\alpha}_{\nu} - \partial_{\nu}G^{\alpha}_{\mu} - g_s f_{\alpha\beta\gamma}G^{\beta}_{\mu}G^{\gamma}_{\nu}, \tag{2.37}$$

where $f_{\alpha\beta\gamma}$ are the structure constants of the $SU(3)_C$ group.

Similar to QED, the gauge interactions among the quarks and gluons are contained in the $\overline{q}i\mathfrak{D}q$ term

$$\overline{q}g_s\frac{\lambda_{\alpha}}{2}G^{\alpha}_{\mu}\gamma^{\mu}q. \tag{2.38}$$

However, there is an important difference of the QCD case from the QED case. The gluon kinetic term $G^{\alpha}_{\mu\nu}G^{\mu\nu}_{\alpha}$ contains a tree and a four gluon terms, which are precisely the self-interaction gluon vertices characteristic of a non-Abelian theory. When a pair of the quarks begins to separate from each other, the exchanged gluons interact with each other and the strong coupling constant, α_s, increases. This increasing force either binds the quarks together at low-energy scale (large distances) or it breaks when the energy density of the color field between the quarks is great enough to create a quark-anti-quark pair, resulting in two separate hadrons (the top quark constitutes an exception in the sense that due to its huge mass, it decays before it *hadronise*). This situation is called *color confinement*. On the opposite side, at high energies (short distances), the strong interaction proceeds via color fields of reduced strength and the quarks and gluons behave as essentially free. This situation is called *asymptotic freedom*. The amplitude of a strong interaction process at a given momentum transfer scale, q^2, can be parameterized in terms of the running coupling constants $\alpha_s(q)$. A conventional definition of α_s, at leading order is given by:

$$\alpha_s(q) = \frac{4\pi}{(11n_c - 2n_f)ln\frac{q^2}{\Lambda^2_{QCD}}}, \tag{2.39}$$

where $n_c(n_f)$ is the number of colors (flavors) of the quarks with mass less than the energy scale q and Λ_{QCD} is the QCD scale, which is the only adjustable parameter of QCD and depends on the momentum scale of the interaction. It marks the energy scale at which α_s becomes large and the perturbative approach is no longer valid. For most processes, the measured value of Λ_{QCD} is consistent with 200 MeV. The running strong coupling presented in Eq. 2.39 shows that for large q^2 (short distances), the coupling becomes small (asymptotic freedom) but at low q^2, the coupling approaches to unity. Hence, high-q^2 processes can be described by perturbative calculations but low-q^2 interactions need to rely on phenomenological model.

2.1.6 Limitations of the SM and the Hierarchy Problem

The SM describes different processes involving electroweak and strong interactions accurately and agrees well with experimental measurements. However, there is still one important missing piece of the SM particle content which is the Higgs boson explaining the origin of particle masses that needs to be hunted in an experiment. In addition, physicists are still pushing to find some deviations from the SM. The main reason is that the SM has serious theoretically motivated problems, starting from the fact that gravity is not included in the theory, that prevent it from being the ultimate theory and corrections to the Higgs mass is *quadratically divergent* which is known as *the hierarchy problem*.

The SM contains at least 19 free parameters including nine lepton and quark masses, three gauge couplings, three mixing angles and one CP violating phase for the quark system, two Higgs sector parameters (μ and λ), and one QCD vacuum angle parameter which cannot be predicted but must be measured in an experiment. One might wish to have less number of free parameters in a theory. In addition, more parameters would be needed to incorporate non-accelerator observations such as the cosmological baryon asymmetry, neutrino masses and mixings or the problematic cosmological constant.

The standard model also leaves several questions unanswered such as why are there three generations, spatial dimensions or colors, how do we understand neutrino oscillations and massive neutrinos, why are the electric charge of the proton and the electron exactly opposite or whether the Higgs mechanism is really the process through which the electroweak symmetry breaking occurs and lay beneath the origin of masses. Further, the model cannot explain which mechanisms producing the matter-antimatter asymmetry observed in the universe or what kind of a relation occurs between the strong and electroweak forces.

Perhaps the most attractive feature of the SM is the accurate descriptions of the interactions between particles with masses 17 orders of magnitude smaller than the Planck mass ($m_{planck} \sim 10^{19}$ GeV) and lack of association of gravity within this framework. This feature may be an indication that the SM is an effective theory; this is a low energy limit of a more fundamental one and one can embed it into a larger theory at high energies which is known as Grand Unified Theory (GUT). The interactions can be unified in terms of running coupling strengths of the SM, but difficulty arises with the strengths that do not meet at a single point (Figure 2.1). This automatically brings the question of up to which energy scale will the SM be valid.

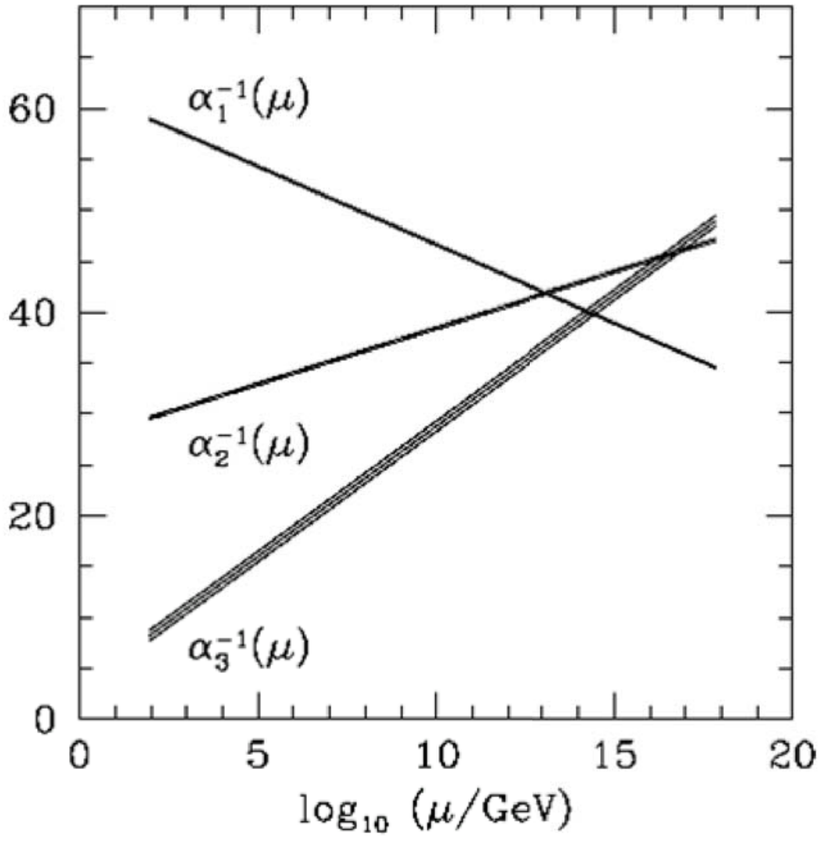

Figure 2.1: Distributions of running coupling strengths of the SM with respect to logarithmic of energy scale, μ.

As explained in the Higgs Mechanism subsection, the Higgs mechanism predicts the existence of a scalar particle in the SM physical spectrum, H_{SM}. However, *spin-0* fields are radically different from fermions and gauge bosons. The latter are protected from large corrections to their masses by making use of *the chiral* and *gauge* symmetries, respectively. In the SM, scalar particles are subject to quadratically divergent radiative corrections and there is no mechanism to prevent scalar particles from acquiring large masses through radiative corrections [11]. Therefore, $m^2_{H_{SM}}$ receives enormous quantum corrections from the virtual effects of every particle which couples to the Higgs field as shown in Figure 2.2.

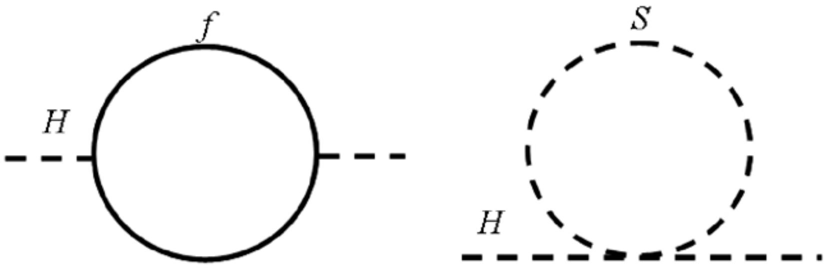

Figure 2.2: One-loop quantum corrections to $m^2_{H_{SM}}$ due to virtual fermion f on the left and virtual scalar S on the right

Due to these corrections, the Higgs mass would be

$$m^2_{H_{SM}} = (m^2_H)_0 + \Delta M^2_H, \tag{2.40}$$

where $(m^2_H)_0$ is the bare Higgs mass and ΔM^2_H is the correction given by

$$\Delta M^2_H = \frac{y^2_f}{16\pi^2}[-2\Lambda^2 + 6m^2_f ln(\frac{\Lambda}{m_f}) + ...], \tag{2.41}$$

where y_f is the Yukawa coupling of the fermion f and Λ is an energy cutoff which is interpreted as the energy scale at which new physics enters and changes the high energy behavior of the theory (which could be as large as the Planck scale). If the SM needs to describe nature until the Planck scale, then the quantum correction ΔM^2_H is about 32 orders of magnitude larger than the bare Higgs mass square. A cancellation of this correction at all orders would call for an incredible *fine tuning* which seems very unlikely.

In a model with spontaneous electroweak symmetry breaking, the problem affects not only the Higgs mass but also its expectation value and the masses of other particles that get their masses through this mechanism such as W, Z, quarks, and charged leptons. Hence, it is unnatural to have all the SM particles masses at the electroweak scale unless the model is somehow cut off and embedded in a richer structure at energies no bigger than the TeV scale.

2.2 Supersymmetry

The hierarchy problem of the SM discussed before can be fixed in an elegant way by introducing a symmetry which relates fermions and bosons. This symmetry, named Supersymmetry (SUSY), is the most motivated beyond the SM scenario having a submodel which appears to be similar to the SM in theoretical treatment called the Minimal Supersymmetric Standard Model (MSSM) addressing the open questions of the SM. SUSY can be accommodated with minimal Supergravity (mSuGra) model by both constraining the parameter space and taking gravity into consideration which are not possible in the SM.

2.2.1 SUSY Algebra

SUSY is introduced in the early 1970s by Yuri Golfand and Evgeny Likhtman (in 1971), Dimitri Volkov and Viladamir Akulov (in 1973) [12], and Julius Wess and Bruno Zumino (in 1974) [13] independently as a radically new type of symmetry of space-time and fundamental fields. In SUSY, an operator Q generates the transformation of converting fermions (matter) to bosons (interactions) and vice versa [14]:

$$Q|Fermion(Boson)\rangle = |Boson(Fermion)\rangle. \tag{2.42}$$

Q and its hermitian conjugate, $\bar{Q}$ are symmetry generators. Both Q and $\bar{Q}$ are fermionic spinors in nature (spin-$\frac{1}{2}$) and satisfy an algebra of commutation and anti-commutation relations:

$$\{Q, \bar{Q}\} = P^{\mu}, \tag{2.43}$$

$$\{Q, Q\} = \{\bar{Q}, \bar{Q}\} = 0, \tag{2.44}$$

$$[P^{\mu}, Q] = [P^{\mu}, \bar{Q}] = 0, \tag{2.45}$$

where P^{μ} is the four momentum generator of space-time translations. P^{μ} on the right-hand side of Eq. 2.43 transforms under Lorentz rotations, J and boosts, K as a spin-1 object while Q and $\bar{Q}$ on the left-hand side transform as spin-$\frac{1}{2}$ objects. In fact, SUSY is a unique extension of Poincaré Algebra that is a generalization of the space-time symmetries of quantum field theory which is an extension of the Lorentz group.

In SUSY, extension of usual space-time coordinates x^{μ} can be written in terms of anti-commutating coordinates, θ and $\bar{\theta}$ as

$$x^\mu \to (x^\mu, \theta, \bar{\theta}), \tag{2.46}$$

where $(x^\mu, \theta, \bar{\theta})$ is called *superspace* in the language of SUSY. In Quantum Field Theory, particles are represented by fields, functions of the four space-time coordinates, such as the differential Poincaré operators:

$$P_x = i\frac{\partial}{\partial x}, J_x = -i(y\frac{\partial}{\partial z} - z\frac{\partial}{\partial y}), K_x = i(t\frac{\partial}{\partial x} + x\frac{\partial}{\partial t}). \tag{2.47}$$

On the other hand, in SUSY algebra, particles are combined into *superfields* as a function of x^μ, θ, and $\bar{\theta}$ such that differential SUSY operators can be written as

$$Q_\alpha = \frac{\partial}{\partial \theta^\alpha} - i\sigma^\mu_{\alpha\dot{\beta}}\bar{\theta}^{\dot{\beta}}\partial_\mu \tag{2.48}$$

and

$$\bar{Q}_{\dot{\beta}} = -\frac{\partial}{\partial \bar{\theta}_{\dot{\beta}}} + i\theta^\alpha \sigma^\mu_{\alpha\dot{\beta}}\partial_\mu, \tag{2.49}$$

where α and $\dot{\beta}$ are known as two-component left-handed and right-handed spinor indices, respectively. These operators then act on superfields which are the natural representations of the supersymmetry algebra. Superfields are expanded in powers of θ and $\bar{\theta}$ in order to determine the particle content of SUSY.

The simplest superfields are *chiral superfields*, independent of $\bar{\theta}$ (and *anti-chiral superfields*, independent of θ). Expansion of chiral superfields in terms θ is of the form:

$$\Psi(x, \theta) = \phi(x) + \sqrt{2}\theta^\alpha \psi_\alpha(x) + \theta\theta F(x), \tag{2.50}$$

where, $\phi(x)$ corresponds to a complex scalar (*squarks*, *sleptons*, and the SM Higgs), ψ_α corresponds to a chiral fermion (quarks, leptons, and *higgsino*), and $F(x)$ refers to an auxiliary field.

In addition to chiral superfields, *vector superfields* which are functions of both vector θ and $\bar{\theta}$ can be given as

$$V(x, \theta, \bar{\theta}) = \theta\sigma^\mu v_\mu(x) - i\bar{\theta}\bar{\theta}\theta^\alpha \lambda_\alpha(x) + i\theta\theta\bar{\theta}_{\dot{\alpha}}\bar{\lambda}^{\dot{\alpha}}(x) + \frac{1}{2}\theta\theta\bar{\theta}\bar{\theta}D(x), \tag{2.51}$$

where $v_\mu(x)$ contains a vector boson, $\lambda(x)$ in the second and third terms on the right-hand side refers to a Majorana fermion, and $D(x)$ is an auxiliary field. The details of the particle content of SUSY left to the MSSM subsection. Additionally, more specific and comprehensive discussions on SUSY algebra formalism can be found elsewhere ([14], [15], [16], and [17]).

2.2.2 SUSY Solution to the Hierarchy Problem

The SM Hierarchy problem presented before is easily solved when considering the supersymmetric theory [18]. The reason is that every fermion f has a scalar SUSY partner S that couples to the Higgs as well and contributes with a mass correction term of the form:

$$\Delta M_H^2 = \frac{y_S^2}{16\pi^2}[2\Lambda^2 - 2m_S^2 ln(\frac{\Lambda}{m_S}) + ...]. \tag{2.52}$$

Since now y_f=y_S and all the terms in Eq. 2.41 and Eq. 2.52 have counter-term that naturally cancel the huge corrections (noting that logarithmic terms are not no longer necessary to be cancelled). The terms that do not cancel are of the form:

$$\Delta M_H^2 = \frac{y^2}{16\pi^2}|m_S^2 - m_f^2|. \tag{2.53}$$

This result leads us to the following naturalness argument: since these corrections must not be greater than $m_{H_{SM}}$ in order to avoid too much fine tuning, then

$$|m_S^2 - m_f^2| \leq 1TeV^2. \tag{2.54}$$

Hence, one associates $\Lambda \sim 1$ TeV as the scale where the SM is no longer valid and must be substituted by its supersymmetric extension. As a benefit, this new theory would be valid all the way up to the Planck scale.

Besides making the Higgs mass natural, SUSY has other interesting consequences. One of them is that when SUSY is locally realized it contains among its gauge fields the *gravitino*. Thus SUSY seems a good candidate for all interactions including gravity, or at least to play an important role in any such theory. In addition, Grand Unified Theories (GUTs) also provide good motivation for the existence of supersymmetry. One can use the running of the three couplings of the SM, measured at the electroweak scale, and find that, at a certain GUT scale of 10^{16} GeV; the couplings almost become the same value ($\alpha_{unification} \approx 1/24$) as show in Figure 2.3 with SUSY modifications. This is a strong theoretical motivation for the need of SUSY.

Furthermore, some SUSY models (including the MSSM) predict the presence of a lightest supersymmetric particle, *neutralino* which is a candidate for dark matter in the universe, provided that it is neutral, weakly interacting, and stable.

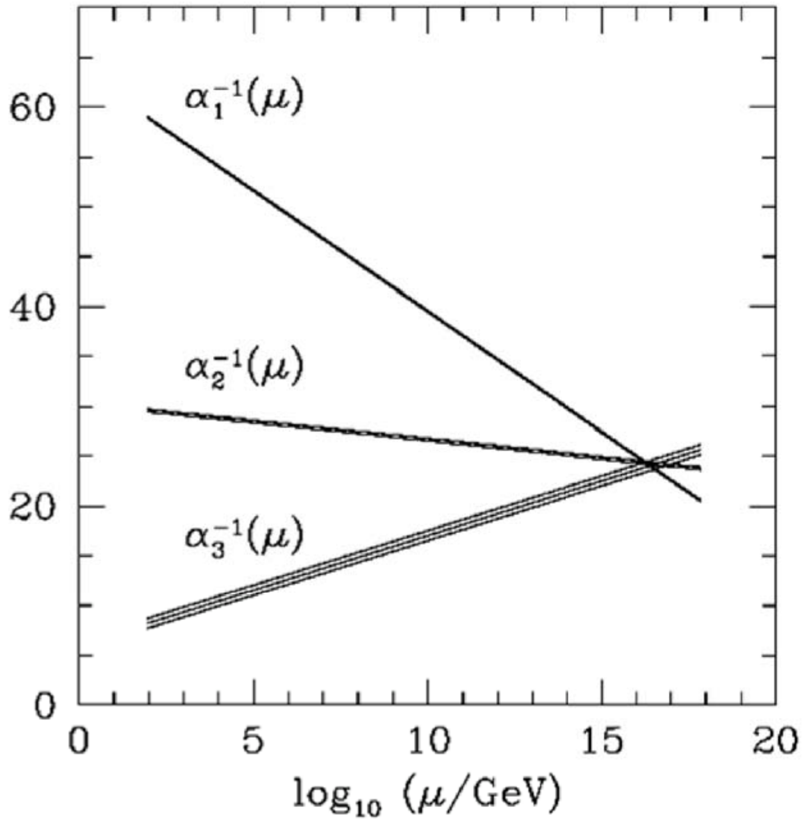

Figure 2.3: Unification of running coupling strengths in SUSY

2.2.3 The Minimal Supersymmetric Standard Model

Similar to the SM construction, that was conceived to be the minimal group viable to explain the electroweak sector, the MSSM is the minimal viable supersymmetric extension of the SM ([19], [20], and [21]). The MSSM obeys the same $SU(3)_C \otimes SU(2)_L \otimes U(1)_Y$ gauge symmetries of the SM but doubles the spectrum of new particles since for every particle in the SM, a *superpartner* is postulated which differs by half a unit of spin. The superpartners are conveniently described by a notation with close correspondence to the SM notation for bosons and fermions. Hence, the superpartners are written with the same letter of their partner but with a *tilde* over it and superfields are written with a *hat* superscript. In addition, the bosonic partners of the fermions are denoted starting with an extra *s* (scalar) (e.g. selectron is the superpartner of the electron) and the fermionic partners of the bosons finish with the suffix *ino* (e.g. gluino is the superpartner of the gluon).

For simplicity, one generation of quarks, leptons, and their superpartners can be considered in the context of the MSSM. One can define $\hat{Q}$ as the superfield and their scalar partners of quarks which are in a $SU(2)_L$ doublet have the form:

$$\hat{Q} = \begin{pmatrix} \tilde{u}_L \\ \tilde{d}_L \end{pmatrix}. \tag{2.55}$$

In a similar form, the superfield $\hat{U}^c$ ($\hat{D}^c$) contains the right-handed up (down) anti-quark, $\bar{u}_R$ ($\bar{d}_R$), and its scalar partner, $\tilde{u}_R^*$ ($\tilde{d}_R^*$). The superscript c of the superfields is to remind *charge conjugation*. Following the same pattern, scalar partners of leptons which are contained in the $SU(2)_L$ doublet represented by superfield $\hat{L}$:

$$\hat{L} = \begin{pmatrix} \tilde{\nu}_L \\ \tilde{e}_L \end{pmatrix}. \tag{2.56}$$

In addition, the superfield $\hat{E}^c$ contains the right-handed anti-electron $\bar{e}_R$, and its scalar partner, $\tilde{e}_R^*$. In the MSSM, for every gauge boson there is a Majorana fermion (gaugino). $\hat{G}_a$ is defined as a superfield that contains all the gluons, g_a , and their fermion partners the gluinos $\tilde{g}_a$; $\hat{W}_i$ contains the $SU(2)_L$ gauge bosons, W_i , and their fermionic partners, $\tilde{w}_i$ (winos), and $\hat{B}$ contains the $U(1)$ gauge field, B, and its superpartner, $\tilde{b}$ (bino).

In the MSSM, the Higgs sector is enlarged to dismiss gauge anomalies. Cancellation of anomalies is achieved by requiring an additional Higgs doublet and accompanying superpartners. Thus, the SM can be considered as a two Higgs doublet model in the context of the MSSM. For that, an up-like Higgs superfield, $\hat{H}_u$ and down-like superfield $\hat{H}_d$ are proposed. Finally, although not strictly a particle of the SM, the graviton G is the gauge boson of gravity and its superpartner, the gravitino $\tilde{G}$ is introduced in the MSSM with a superfield $\hat{G}$, which plays an important role in the phenomenology of some supersymmetric models. For clarification, the superfield spectrum of the MSSM is shown in Table 2.3 in one go.

Having discussed the superfields and the particle content of the MSSM, the parameters of supersymmetry-conserving sector can be given in a list [23]:

- Gauge couplings: g_s, g, and g' corresponding to the SM gauge group,
- Higgs mass parameter, μ,
- Higgs-fermion Yukawa coupling constants: y_u, y_d, and y_l corresponding to the coupling of quarks or leptons and their superpartners to the Higgs bosons and higgsinos.

Table 2.3: Superfields and particle content of the MSSM.

Chiral Supermultiplets	Quarks ($\times 3 families$)	Spin	Squarks ($\times 3 families$)	Spin
$\hat{Q}$	(u_L, d_L)	$\frac{1}{2}$	$(\tilde{u_L}, \tilde{d_L})$	0
$\hat{U}^c$	$u_R^\dagger$	$\frac{1}{2}$	$\tilde{u}_R^*$	0
$\hat{D}^c$	$d_R^\dagger$	$\frac{1}{2}$	$\tilde{d}_R^*$	0
	Leptons ($\times 3 families$)	Spin	Sleptons ($\times 3 families$)	Spin
$\hat{L}$	(ν, e_L)	$\frac{1}{2}$	$(\tilde{\nu}, \tilde{e}_L)$	0
$\hat{E}^c$	$e_R^\dagger$	$\frac{1}{2}$	$\tilde{e}_R^*$	0
	Higgs bosons	Spin	Higgsinos	Spin
$\hat{H}_u$	(H_u^+, H_u^0)	0	$(\tilde{H}_u^+, \tilde{H}_u^0)$	$\frac{1}{2}$
$\hat{H}_d$	(H_d^0, H_d^-)	0	$(\tilde{H}_d^0, \tilde{H}_d^-)$	$\frac{1}{2}$

Vector Supermultiplets	Gauge bosons	Spin	Gauginos	Spin
$\hat{G}_a$	g_a	1	$\tilde{g}_a$	$\frac{1}{2}$
$\hat{W}_i$	W_1, W_2, W_3	1	$\tilde{w}_1, \tilde{w}_2, \tilde{w}_3$	$\frac{1}{2}$
$\hat{B}$	B	1	$\tilde{b}$	$\frac{1}{2}$

Gravity Supermultiplet	Graviton	Spin	Gravitino	Spin
$\hat{G}$	G	2	$\tilde{G}$	$\frac{3}{2}$

The remaining parameters of the MSSM arose from supersymmetry-breaking sector including

- Gaugino Majorana masses M_1, M_2, and M_3,
- Five scalar mass-squared parameters for the squarks and sleptons: $M^2_{\hat{Q}}$, $M^2_{\hat{U}}$, $M^2_{\hat{D}}$, $M^2_{\hat{L}}$, and $M^2_{\hat{E}}$ corresponding to the five electroweak gauge multiplets,
- Trilinear interaction terms of the form Higgs-squark-squark and Higgs-slepton-slepton, with coefficients A_u, A_d, and A_l,
- The scalar Higgs squared-mass parameters, two of which (m_1^2 and m_2^2) contribute to the diagonal Higgs squared-masses and a third which corresponds to the off-diagonal terms, $m_{12}^2 \equiv \mu B$. These three parameters can be re-expressed in terms of the two Higgs vacuum expectation values ($v_d = \langle H_d^0 \rangle$ and $v_u = \langle H_u^0 \rangle$), usually taken through the ratio

$$tan\beta \equiv \frac{v_u}{v_d}. \tag{2.57}$$

The MSSM has three massless gauge bosons, after SUSY breaking, the three gauge bosons acquire masses which points that there should exist five spin-0 Higgs field in the particle spectrum of the SM: three natural scalars (h, H, A) and two charged pairs (H^+, H^-).

The supersymmetric partners of the gauge and Higgs bosons (gauginos and higgsinos) can mix. As a result, the physical mass eigenstates are model-dependent linear combinations of these states, called *charginos* and *neutralinos*, which are obtained by diagonalising the corresponding mass matrices. There are four charginos ($\tilde{\chi}_i^{\pm}$) and four neutralinos ($\tilde{\chi}_i^{0}$) which are by convention ordered in masses ($\tilde{\chi}_1^{\pm}$ is the lowest chargino and $\tilde{\chi}_1^{0}$ is the lowest neutralino). Depending whether the chargino or neutralino eigenstate approximates a particular gaugino or higgsinos state, they can become more photino-like, bino-like and result is strikingly different phenomenology.

The supersymmetric partners of the quarks and leptons are spin-0 bosons and the resulting squarks and sleptons can mix their left- and right-handed components yielding the mass eigenstates (denoted by the indices 1,2 instead of *L*,*R*). This mixing is proportional to the mass of the SM partner quark or lepton and to *tanβ*. Thus, the mixing can lead to an important splitting in the mass spectrum of the heavy quarks, especially at large *tanβ*. In contrast, the first two families can be considered degenerate in mass. All physical particles of the MSSM are given in Table 2.4.

Table 2.4: The physical particles of the MSSM.

SM Particle	spin	SUSY Particle	spin
quarks: q	$\frac{1}{2}$	squarks: $\tilde{q}_1, \tilde{q}_2$	0
leptons: l	$\frac{1}{2}$	sleptons: $\tilde{l}_1, \tilde{l}_2$	0
gluons: g_a	1	gluinos: $\tilde{g}_a$	$\frac{1}{2}$
gauge bosons: $W^{\pm}, Z^0, \gamma$	1	neutralinos: $\tilde{\chi}_1^0, \tilde{\chi}_2^0, \tilde{\chi}_3^0, \tilde{\chi}_4^0$	$\frac{1}{2}$
Higgs bosons: $h^0, H^0, A^0, H^{\pm}$	0	charginos: $\tilde{\chi}_1^{\pm}, \tilde{\chi}_2^{\pm}$	$\frac{1}{2}$
graviton: G	2	gravitino: $\tilde{G}$	$\frac{3}{2}$

2.2.4 MSSM Lagrangian and R-parity

The interactions of the MSSM are best understood if MSSM lagrangian can be constructed using the already defined particle content and following an analogy with the SM lagrangian ([22], [23], [24]). By using the SM notation, the kinetic term of the lagrangian can be written as :

$$L_{KE} = \sum_i \{(D_\mu S_i)^\dagger (D^\mu S_i) + i\bar{\psi}_i \gamma^\mu D_\mu \psi_i\} + \sum_A \{-\frac{1}{4} F^A_{\mu\nu} F^{\mu\nu A} + \frac{i}{2} \bar{\lambda}_A \gamma^\mu D_\mu \lambda_A\}. \qquad (2.58)$$

Here, S_i (ψ_i) is the scalar (fermion) component of the i^{th} chiral superfield, $F^A_{\mu\nu}$ is the Young-Mills gauge field, and λ_A is the gaugino superpartner of the corresponding gauge boson. It is worth noticing that the $\sum_i$ is a sum over all fermion fields of the SM, the scalar partners and the two Higgs doublets with their fermion partners. On the other hand, $\sum_A$ is over the $SU(3)_C$, $SU(2)_L$, and $U(1)_Y$ gauge fields with their fermion partners, the gauginos.

In the MSSM, the interactions between gauge bosons and fermions are described by:

$$L_{int} = -\sqrt{2}\sum_{i,A} g_A(S_i^* T^A \bar{\psi}_{iL}\lambda_A + h.c.) - \frac{1}{2}\sum_A(\sum_i g_A S_i^* T^A S_i)^2, \tag{2.59}$$

where $\psi_L \equiv \frac{1}{2}(1-\gamma_5)\psi$, T^A is the matrix of the group generators, and g_A are the gauge coupling constants. It can be seen that there is no adjustable parameter; hence, all interaction strengths are completely fixed in terms of SM coupling constants.

Once the superfields and the gauge symmetries are chosen, the only freedom in constructing L_{MSSM} is contained in a function called superpotential, ω . From the superpotential, both the scalar potential and the Yukawa interactions of the fermions with the scalars can be found:

$$L_\omega = -\sum_i |\frac{\partial\omega}{\partial z_i}|^2 - \frac{1}{2}\sum_{ij}[\bar{\psi}_{iL}\frac{\partial^2\omega}{\partial z_i \partial z_j}\psi_j + h.c.], \tag{2.60}$$

where z is a chiral superfield. This form of the lagrangian is dictated by the supersymmetry and by the requirement that it is renormalizable.

The superpotential ω is an analytic form of the chiral superfields of Table 2.3, that has the form:

$$\omega = \epsilon_{ij}\mu\hat{H}_u^i\hat{H}_d^j + \epsilon_{ij}(y_l\hat{H}_d^i\bar{\hat{L}}^j\bar{\hat{E}} + y_d\hat{H}_d^i\hat{Q}\bar{\hat{D}} + y_u\hat{H}_u^j\hat{Q}^i\bar{\hat{U}}) + \omega_{RP}, \tag{2.61}$$

where i and j are $SU(2)_L$ doublet indices and $\epsilon_{ij} = -\epsilon_{ji}$ (with $\epsilon_{12} = 1$) contracts the $SU(2)_L$ doublet fields. No derivative interactions are allowed in order that be an analytical function. The term $\mu\hat{H}_u^i\hat{H}_d^j$ gives mass terms for the Higgs boson and so μ is often called the Higgs mass parameter. The terms in the parenthesis proportional to y_l, y_u, and y_d give the usual Yukawa interactions of the fermions with the Higgs bosons. Hence, unlike the SM case, these coefficients are determined in terms of the fermion masses and the vacuum expectation values of the neutral members of the scalar components, and are not arbitrary couplings.

In the most general superpotential, one can add more terms which are grouped under W_{RP} in Eq. 2.61. These terms are of the form:

$$\omega_{RP} = y_{\alpha\beta\gamma}\hat{L}^\alpha\hat{L}_\beta\bar{\hat{E}}^\gamma + y'_{\alpha\beta\gamma}\hat{L}^\alpha\hat{Q}^\beta\bar{\hat{D}}^\gamma + y''_{\alpha\beta\gamma}\bar{\hat{U}}^\alpha\bar{\hat{D}}^\beta\bar{\hat{D}}^\gamma + \mu\hat{L}\hat{H}, \tag{2.62}$$

where the indices α, β, and γ label the three generations of quarks and leptons. These terms constitute a problem in the sense that the first two and the fourth terms contribute to lepton number violation interactions and the third one to baryon number violation interactions. The combination of lepton and baryon violation terms can contribute to the proton decay at tree level through the exchange of the scalar partner of the down quark. Since this process is experimentally restricted, it put into the question of the validity of the model.

One solution is to assume that the parameters are small enough to avoid experimental limits. Even this is certainly allowed experimentally, this would imply the introduction of an artificial tuning. The other solution is to introduce a new symmetry called R-parity. R-parity (R_p) is multiplicative quantum number defined as:

$$R = (-1)^{3(B-L)+2s}, \tag{2.63}$$

where B is baryon and L is lepton quantum numbers and s is the spin of the particle. Thus, all SM particles have $R_p = +1$ while their SUSY partners have $R_p = -1$.

The assumption of such symmetry prevents lepton and baryon number violating terms but has also dramatic phenomenological consequences: there can be no mixing between the sparticles and the $R_p = 1$ particles, SUSY particles can only be pair-produced in the collisions of SM particles and a SUSY particle would undergo a chain of decays until the lightest SUSY particle (LSP) is produced. Then, this LSP cannot decay further and constitutes a cold dark matter candidate.

2.2.5 SUSY Breaking

At this point, the MSSM lagrangian does not provide mass terms for all the particles (fermions, scalars, gauge fields). If supersymmetry was an exact symmetry, quarks and squarks would have equal masses and gluinos would be massless [25]. Since this is not the case in nature, at low energies supersymmetry must be a broken symmetry and new SUSY-breaking terms need to be introduced in the lagrangian. To prevent dangerous quadratic divergences, only a small subset of supersymmetry-breaking terms is present in the theory and their couplings are denoted as soft parameters.

Hence, the soft lagrangian which breaks SUSY has the form of (first generation only):

$$
\begin{aligned}
-L_{soft} = \frac{1}{2}(M_3\hat{g}\hat{g} + M_2\hat{W}\hat{W} + M_1\hat{B}\hat{B}) + \epsilon_{\alpha\beta}(-\mu B H_d^\alpha H_u^\beta - H_u^\alpha \hat{Q}_i^\beta \hat{A}_{u_{ij}} \bar{\hat{U}}_j \\
+ H_d^\alpha \hat{Q}_i^\beta \hat{A}_{d_{ij}} \bar{\hat{D}}_j + H_d^\alpha \hat{L}_i^\beta \hat{A}_{l_{ij}} \bar{\hat{E}}_j + h.c.) + m_{H_d}^2 |H_d|^2 + m_{H_u}^2 |H_u|^2 \\
+ \hat{Q}_i^\alpha m_{Q_{ij}}^2 \hat{Q}_j^{\alpha *} + \hat{L}_i^\alpha m_{L_{ij}}^2 \hat{L}_j^{\alpha *} + \bar{\hat{U}}_i^* m_{U_{ij}}^2 \bar{\hat{U}}_j + \bar{\hat{D}}_i^* m_{D_{ij}}^2 \bar{\hat{D}}_j + \bar{\hat{E}}_i^* m_{E_{ij}}^2 \bar{\hat{E}}_j.
\end{aligned}
\tag{2.64}
$$

This lagrangian has arbitrary masses for the scalars and gauginos and also arbitrary bi-linear and tri-linear mixing terms. The scalar and gaugino mass terms have the desired effect of breaking the mass degeneracy between the particles and their SUSY partners. The tri-linear A term affect primarily the particles of third generation. The μB term mixes the scalar components of the two Higgs doublet. In the most general case, all of the mass and interaction terms of Eq. 2.64 are matrices involving all three generators. However, the origin of all these terms is left unspecified. How supersymmetry breaking is transmitted to the superpartners is encoded in the parameters of L_{soft}. All of the quantities in L_{soft} receive radiative corrections and thus are scale-dependent, satisfying so-called Renormalization Group Equations (RGEs).

For phenomenological purposes, the MSSM lagrangian is simply a low energy effective lagrangian with a number of input parameters. The fact that except for the assumption of the presence of supersymmetric particles, R_p, and gauge and Poincaré invariance, nothing else has been assumed makes from the MSSM a very simple framework but one needs to introduce plenty of free input parameters. MSSM includes at least 105 new parameters that added to the 19 parameters of the SM, the model has 124 parameters to be determined. While often only subsets of these parameters are relevant for experimental processes and there exists some phenomenological constraints in these parameters, the number is too large for practical purposes to carry out phenomenological analyses in full generality.

However, unlike in the SM case, now there is the possibility to establish a top-down approach by which the MSSM parameters are predicted within the context of an underlying theory, often as functions of fewer basic parameters. The basic question to be addressed is how to understand the explicit soft supersymmetry encoded in the L_{soft} parameters as the result of spontaneous supersymmetry breaking in a more fundamental theory. Since this is not known, different models have been constructed as an attempt to find an answer for this question. Since TeV scale supersymmetry breaking models have reported negative results, other models which assume that the theory can be splitted into at least two sectors have been considered. These two sectors have no direct renormalisable couplings between them and they are divided into *observable* or *visible* sector, which contains the SM fields and their superpartners, and the *hidden* sector, in which supersymmetry is spontaneously broken by a dynamical mechanism.

Within this framework, SUSY breaking is communicated from the hidden sector where it originates to the observable sector via suppressed interactions involving a third set of fields: the *mediator* or *messenger* fields. The hidden sector implies that the fundamental scale of supersymmetry breaking μ_s is hierarchically larger than the TeV scale. Depending on the model this μ_s can be postulated to be at the GUT scale, Majorana neutrino mass scale or extra-dimensional braneworlds. Therefore, different models account for specific mechanisms on how supersymmetry breaking is mediated between the hidden and observable sectors and involve specific energy scales at which the soft terms are generated. These values are then used to compute the corresponding values at observable energy scales, all predicted at the TeV scale by the models, using the scale dependence of the L_{soft} parameters as dictated by their RGEs.

2.2.6 Constraining the MSSM: mSuGra Model

The observation that the measured coupling constants tend to meet at a point when evolved to high energy scales inspired many SUSY GUT models. In these models, the value of the couplings at the GUT scale $M_{GUT} \sim 10^{16}$ GeV plays a central role:

$$\sqrt{\frac{5}{3}}g'(M_{GUT}) = g(M_{GUT}) = g_s(M_{GUT}) \equiv g_{GUT}, \tag{2.65}$$

Since gravitational interactions are shared by all the particles, it is quite natural to imagine gravity to be the only interaction shared by the both hidden and the observable sector. Furthermore, at some point gravity must be present in particle field theory if a comprehensive description of nature is desired. Here, supergravity would be the responsible of promoting global supersymmetry to local supersymmetry. This is what inspired to mSuGra model [26].

In this model, along with the coupling constants, the following set of assumptions emerges:

1. Common gaugino mass $m_{1/2}$: the gaugino mass terms are assumed to unify:

$$M_1(M_{GUT}) = M_2(M_{GUT}) = M_3(M_{GUT}) \equiv m_{1/2}, \tag{2.66}$$

2. Common scalar mass m_0: The soft SUSY-breaking scalar mass terms contributing to

the squark, slepton, and Higgs boson masses are equal to m_0 at M_{GUT}:

$$M^2_{\hat{Q}}(M_{GUT}) = M^2_{\hat{u}}(M_{GUT}) = ...$$

$$M^2_{H_d}(M_{GUT}) = M^2_{H_u}(M_{GUT}) \equiv m^2_0, \tag{2.67}$$

3. Common tri-linear scalar coupling A_0. The soft tri-linear SUSY-breaking terms are equal to A_0 at M_{GUT},

$$A_u(M_{GUT}) = A_d(M_{GUT}) = A_l(M_{GUT}) = ... \equiv A_0. \tag{2.68}$$

Through RGE's the gaugino masses in Eq. 2.66 scale in the same way as the corresponding coupling constants:

$$M_i(M_W) = m_{1/2}\frac{g^2_i(M_W)}{g^2_{GUT}}, \tag{2.69}$$

yielding

$$M_3 \equiv m_{\tilde{g}} \approx 2.7m_{1/2}$$

$$M_2(M_W) \approx 0.8m_{1/2}$$

$$M_1(M_W) \approx 0.4m_{1/2}, \tag{2.70}$$

where every term is evaluated at the electroweak mass scale, M_W and $m_{\tilde{g}}$ is the gluino mass.

The gluino mass is therefore always the heaviest of the gaugino masses. Assuming the relations Eq. 2.67 and Eq. 2.68 in conjunction with SUSY and the gauge structure, leads to the following expressions for the masses of the sfermions (except for the third generation) at the electroweak scale:

$$m^2_{\tilde{f}_{L,R}} = m^2_f + m^2_0 + b_{\tilde{f}_{L,R}}m_{1/2} \pm m^2_Z cos2\beta(T_3^{\tilde{f}_{L,R}} Q_{\tilde{f}_{L,R}} sin^2\theta_W), \tag{2.71}$$

where $\tilde{f}_{L,R}$ is the corresponding left (right) sfermion $T_3^{\tilde{f}_{L,R}}$ are the third component of the weak isospin, Q is the electric charge of the corresponding fermion f, and coefficients b are derived from the RGE's and can take different values. In particular, $b \approx 6$ for squarks, ≈ 0.5 for sleptons, and ≈ 0.15 for right sleptons. Thus, the squarks are heavier than the sleptons, which is not surprising provided that the squarks have strong interaction in addition to electroweak. More concretely, the mass parameters of the first two generations are roughly degenerate while for the third generation masses are typically reduced by a factor of 1-3. However, the concrete spectrum can vary depending on the $tan\beta$ value.

Since the supersymmetry is broken via gravitational interaction, a new massless Goldstone particle (the Goldstino) needs to be presented. This way the particle will be eaten by the gravitino (the spin-$\frac{3}{2}$ partner of the spin-2 graviton), such that it becomes massive, determining the SUSY breaking scale, μ_s:

$$m_{\tilde{G}} \sim \frac{\mu_s^2}{M_{planck}}. \tag{2.72}$$

Therefore, in mSuGra model the hidden sector is postulated at the Planck mass and, in order to obtain the new SUSY masses at the desired TeV scale to prevent Higgs mass divergence and to obtain coupling unification at the GUT scale, the SUSY breaking scale (following the Eq. 2.72) should be around $10^{11} - 10^{12}$ GeV. The fact that the gravitino is of the order of the TeV is a prediction from the mSuGra model.

With the assumptions from Eq. 2.66 to Eq. 2.68, the SUSY sector in mSuGra is completely described by 5 input parameters at the GUT scale: m_0, $m_{1/2}$, A_0, μ and B, where μ is the Higgs mass parameter and B is the Higgs mixing parameter. The requirement that the Z boson obtain its measured value when the parameters are evaluated at low energy can be used to restrict $|\mu B|$, leaving the sign of μ as a free parameter. In addition, one can also change the B parameter for $tan\beta$, leaving the usual parameters of the model [27]:

$$m_0, m_{1/2}, A_0, tan\beta, sign(\mu). \tag{2.73}$$

This model is the simplest scenario that serves as a good benchmark model since it is extremely predictive as the entire low energy spectrum is predicted in terms of few input parameters. Of course, one needs to bear in mind that changing the input parameters at M_{GUT} (for example assuming non-universal scalar masses) changes the phenomenology at the weak scale. Therefore one should always perform experimental analyses in view of taking the model as a reference and focus as much as possible model independent approaches.

And finally, experimental signatures of SUSY are determined through mSuGra parameters (Eq. 2.72) at LHC with CMS detector. Different combinations of mSuGra parameters offer test points (benchmark points including both low mass LM1-10 and high mass HM1-4 points) of SUSY searches with CMS detector as shown in Figure 2.4.

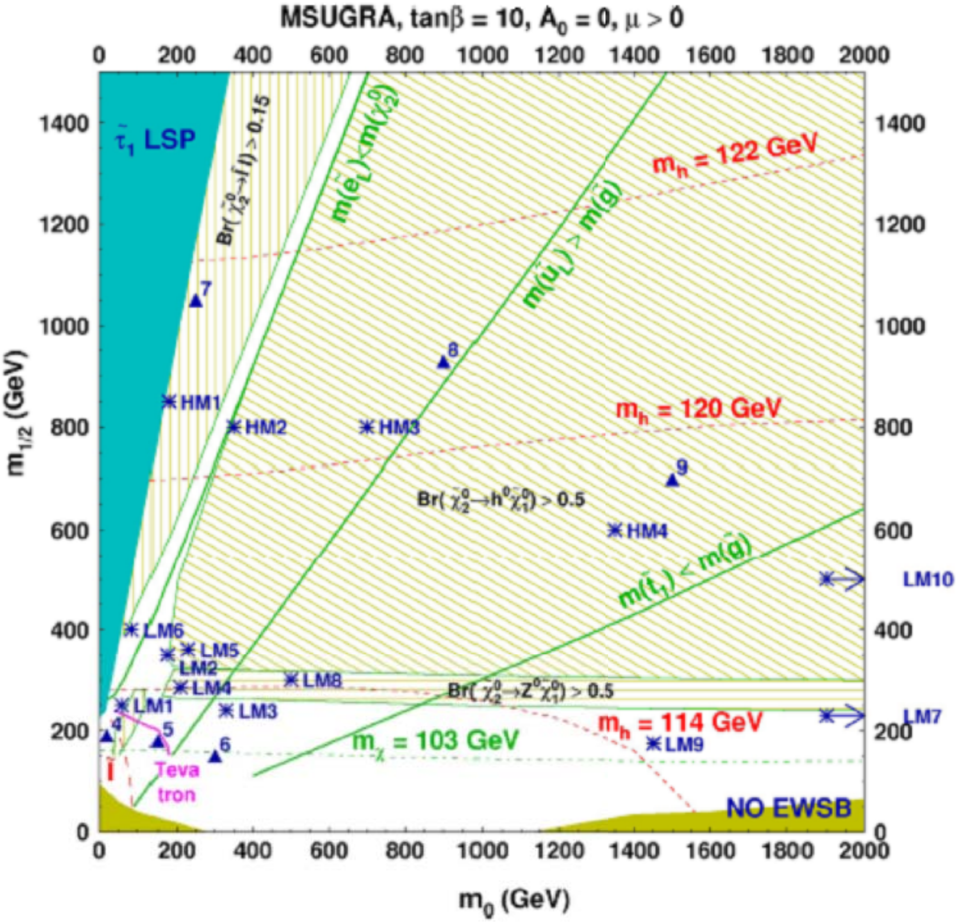

Figure 2.4: CMS SUSY discovery potential of the test points in the m_0 versus $m_{1/2}$ plane. The lines in this plane correspond to the assumptions that $tan\beta = 10$, $A_0 = 0$ and $\mu > 0$.

2.2.7 Squarks and Gluinos

From all variety of particles that the new MSSM framework introduces, two types of them are of special relevance for fully hadronic SUSY searches at LHC with CMS detector and hence for this thesis: squarks and gluinos.

Squarks are the spin-0 boson superpartners of the left- and right- handed quarks. These particles are the part of the Supersymmetric QCD framework, which is based on the colored particles of the MSSM. The massive states are a mixture of the chiral states, with different contributions defined by the set of RGEs that run in the mSuGra framework. This mixture is not particularly significant in the first two generations, which can be degenerate in mass. However, this is not the case for the stop (due to large top mass) and the sbottom at large $tan\beta$.

In RGEs, squarks mass parameters have a stronger dependence on the common gaugino mass $m_{1/2}$ because of color. For the squarks first and second generation, the left- and right-handed soft SUSY-breaking parameters at electroweak scale are given approximately by [27]:

$$m_{\tilde{u}_L,\tilde{d}_L} \approx m_0^2 + 5.0m_{1/2}^2 \tag{2.74}$$

and

$$m_{\tilde{u}_R,\tilde{d}_R} \approx m_0^2 + 4.5m_{1/2}^2. \tag{2.75}$$

The gluino is the color octet fermion (spin-$\frac{1}{2}$) and it cannot mix any other particle in the MSSM. In mSuGra, the gluino mass parameter M_3 is related to the bino and wino masses as shown in the previous subsection:

$$M_3 : M_2 : M_1 \approx 3.4 : 1 : 0.5. \tag{2.76}$$

Therefore, the gluino should be much heavier than the lightest neutralino or chargino. The radiative corrections to the gluino mass can be rather large due to the strong interaction with all squark-quark pairs and its color octet nature.

The general prediction for mSuGra is that

$$m_{\tilde{g}} \leq 1.2m_{\tilde{q}}, \tag{2.77}$$

which holds for the five lightest squarks and small or moderate $tan\beta$. The hadronic production of squarks and gluinos at the LHC in an R_p conserving scenario proceeds through the following partonic reactions [11]:

$$\begin{aligned}
q\bar{q} &\to \tilde{q}\bar{\tilde{q}}, \\
gg &\to \tilde{q}\bar{\tilde{q}}, \\
qq &\to \tilde{q}\tilde{q}, \\
q\bar{q} &\to \tilde{g}\tilde{g}, \\
gg &\to \tilde{g}\tilde{g}, \\
qg &\to \tilde{q}\tilde{g}. \qquad (2.78)
\end{aligned}$$

An exemplary diagram for the $qg \to \tilde{q}\tilde{g}$ decay path (the analysis results regarding this decay channel will be presented in Chapter 6 in detail) is shown in Figure 2.5.

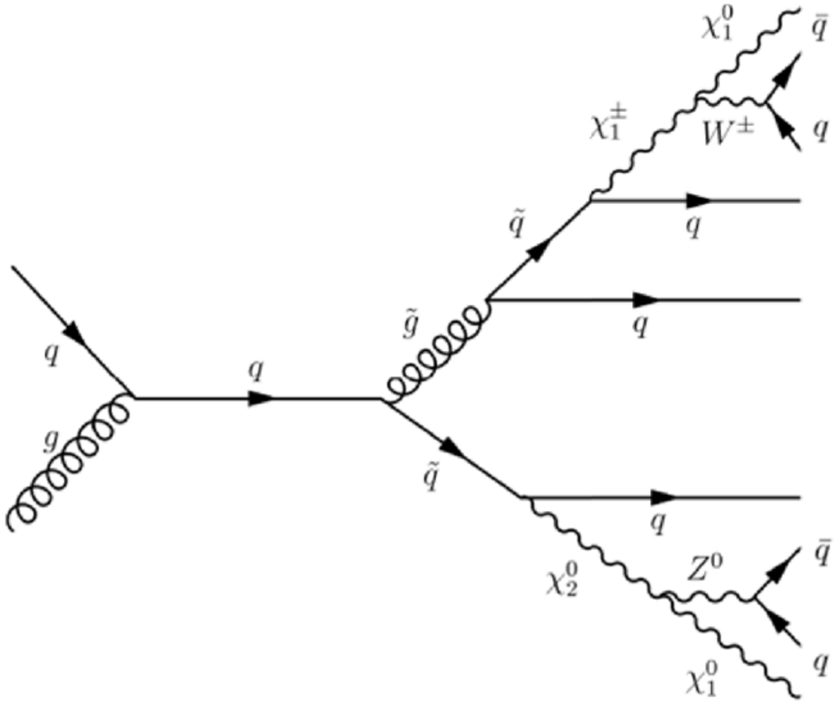

Figure 2.5: Squark-gluino production and further decay processes

In an mSuGra model with R_p conservation, signatures were produced by sparticles in the detector are typically related to E_T^{miss} (missing transverse energy) due to the presence of the LSP (the lightest neutralino, $\tilde{\chi}_1^0$) usually produced after a chain of successive decays of different complexity. The preferred decay modes for squarks are:

$$\tilde{q} \to q\tilde{g},$$

$$\begin{aligned}
\tilde{q} &\to q\tilde{\chi}_1^0, \\
\tilde{q} &\to q + \tilde{\chi}_2^0, \\
\tilde{q} &\to q + \tilde{\chi}_1^+.
\end{aligned} \tag{2.79}$$

The preference for one decay or the other depends on the available phase space. In the case of the gluino, since it has only strong interactions, its decay proceeds through the following reactions:

$$\begin{aligned}
\tilde{g} &\to \tilde{q}q, \tilde{q}\bar{q}, \bar{\tilde{q}}q, \\
\tilde{g} &\to qq'\tilde{\chi}_i^0, \\
\tilde{g} &\to qq'\tilde{\chi}_i^\pm.
\end{aligned} \tag{2.80}$$

The decay of charginos and neutralinos are quite complex since there are several possibilities and the final-state branching fractions are small and quite sensitive to the model. But for an inclusive hadronic search, one can expect at least two jets and missing transverse energy for every squark (gluino) produced. In addition, extra jets from initial and final state radiation can be present as well as some leptons coming from chargino and neutralino decays which is out of the scope of this thesis and these channels contribute to leptonic SUSY searches.

CHAPTER 3

THE CMS EXPERIMENT

The CMS (Compact Muon Solenoid) detector is one of the general purpose detectors constructed at LHC (Large Hadron Collider). This chapter briefly gives an overview for the LHC and CMS subdetector systems including tracker, electromagnetic calorimeter, hadronic calorimeter, muon system, and trigger system. The CMS Computing Model is summarized at the end of the Chapter.

3.1 The Large Hadron Collider

3.1.1 Overview

The Large Hadron Collider (LHC) [28] is a 27 km circumference proton-proton collider constructed at the French-Swiss border west of Geneva, Switzerland. The LHC project is carried out by CERN (European Organisation of Nuclear Research) [29]. It has been designed to achieve a center-of-mass energy ($\sqrt{s}$) of 14 TeV and an instantaneous luminosity of $L_{inst} = 10^{34} cm^{-2} s^{-1}$. As well as colliding proton beams, the LHC will also provide heavy ions (lead-lead) collisions at a center-of-mass energy of 1,312 TeV and a luminosity of $L = 10^{27} cm^{-2} s^{-1}$.

There are four main experiments which will take place at the LHC: two with general purpose detectors, ATLAS (A Toroidal Lhc ApparatuS) and CMS (Compact Muon Solenoid), and two with dedicated detectors, ALICE (A Large Ion Collider Experiment) and LHCb (the Large Hadron Collider Beauty) which will study heavy ion and B-physics respectively. Figure 3.1 shows the four experimental sites along the LHC ring. The CMS detector is situated approximately 100 m underground at IP5 (Interaction Point in 5th LHC octant), and will be taking data from both the p-p and Pb-Pb collision runs.

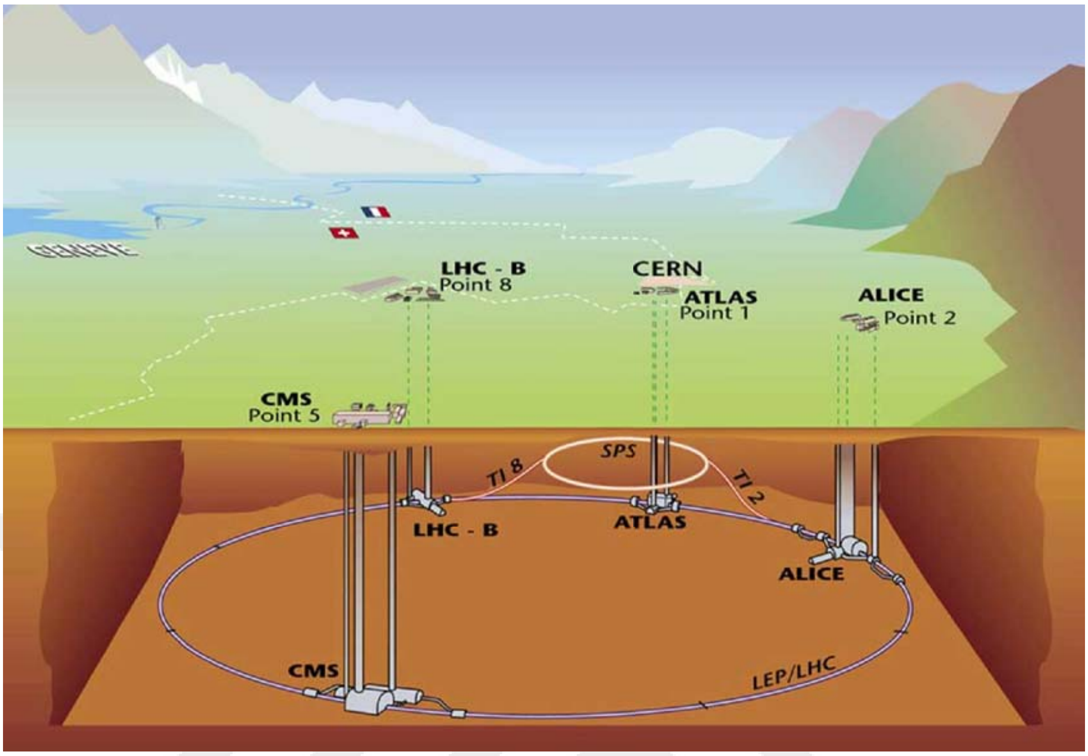

Figure 3.1: LHC experimental sites above and underground seen from north side of the ring. SPS accelerator on the far end is used to pre-accelerate the LHC beam.

The first attempt of beam circulation efforts at LHC ended up with an incident 9 days after the start-up on September 10, 2008. The incident was caused by a faulty electrical connection between two magnets of the accelerator. This resulted in mechanical damage and release of helium from the magnet cold mass into the tunnel. LHC is rescheduled to provide collision data for the experiments including CMS in Fall 2009.

3.1.2 Physics Goals

One of the primary objectives of the LHC is to detect the Higgs boson which is predicted by the SM of elementary particle physics and is believed to be responsible for the spontaneous symmetry breaking of the EWK sector (subsection 1.1.4). Results from the LEP (The Large Electron Positron collider, the former accelerator of CERN) experiments set a lower bound on the Higgs boson mass (M_H), excluding masses below $M_H = 114.4$GeV [30]. At the *Fermilab Tevatron*, there are ongoing experiments searching for the Higgs boson. As of August 2008, combined data from *CDF* and *D0* experiments at the Tevatron were finally sufficient to exclude the Higgs boson at 170 GeV at the 95 percent confidence level as shown in Figure 3.2 [31]. Within this bound, the Higgs boson may decay via a number of channels, and the branching ratio for the different decay modes depends on the Higgs mass. Figure 3.3 shows the expected rate (cross section) of important physics processes at the LHC in different energy-mass scales. It can be seen that the decays of the SM Higgs boson to massive vector bosons (e.g. $H_{SM} \rightarrow 2Z \rightarrow 4\mu$) dominate the high mass range. Further, the Higgs production cross sections are through gluons ($gg \rightarrow H_{SM}$) and quarks ($q\bar{q} \rightarrow q\bar{q}H_{SM}$). These are the two dominant channels at the LHC, able to produce the Higgs boson in the mass range extending from the lower Fermilab and LEP limits up to 1 TeV.

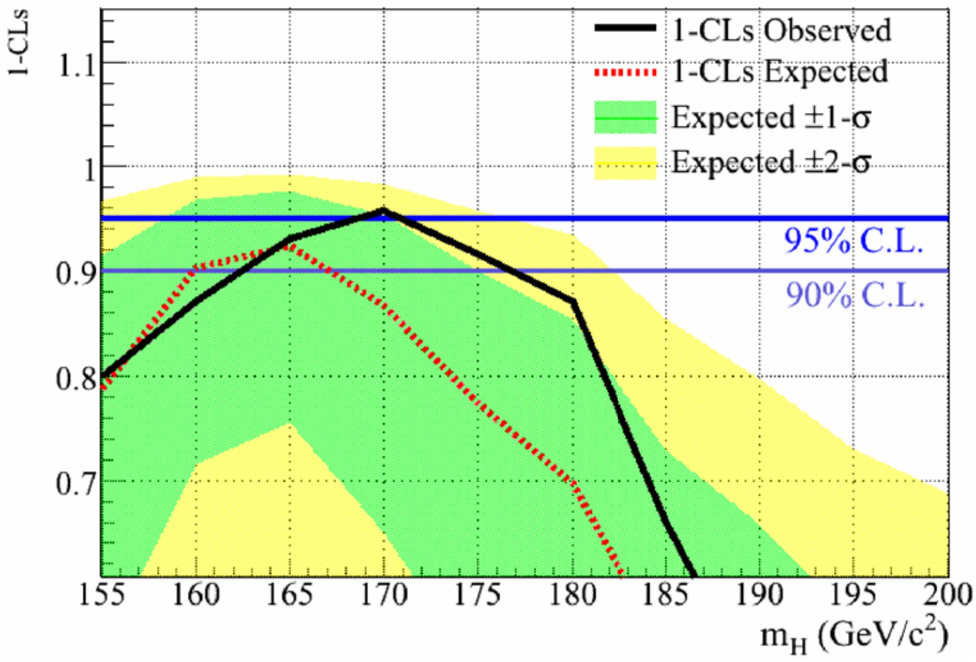

Figure 3.2: Prediction of the mass of Higgs boson obtained from Fermilab Tevatron CDF and DO collaborations

Beyond the Standard Model, SUSY is considered to be a good candidate for resolving the problem of the quadratically diverging mass of the Higgs boson, as described in Chapter 1. The decays of supersymmetric particles, such as squarks and gluinos, if R-parity is conserved, always contain cascades and the lightest SUSY particle, neutralino (LSP). The latter is expected to interact very weakly, thus leading to significant missing transverse energy, E_T^{miss},

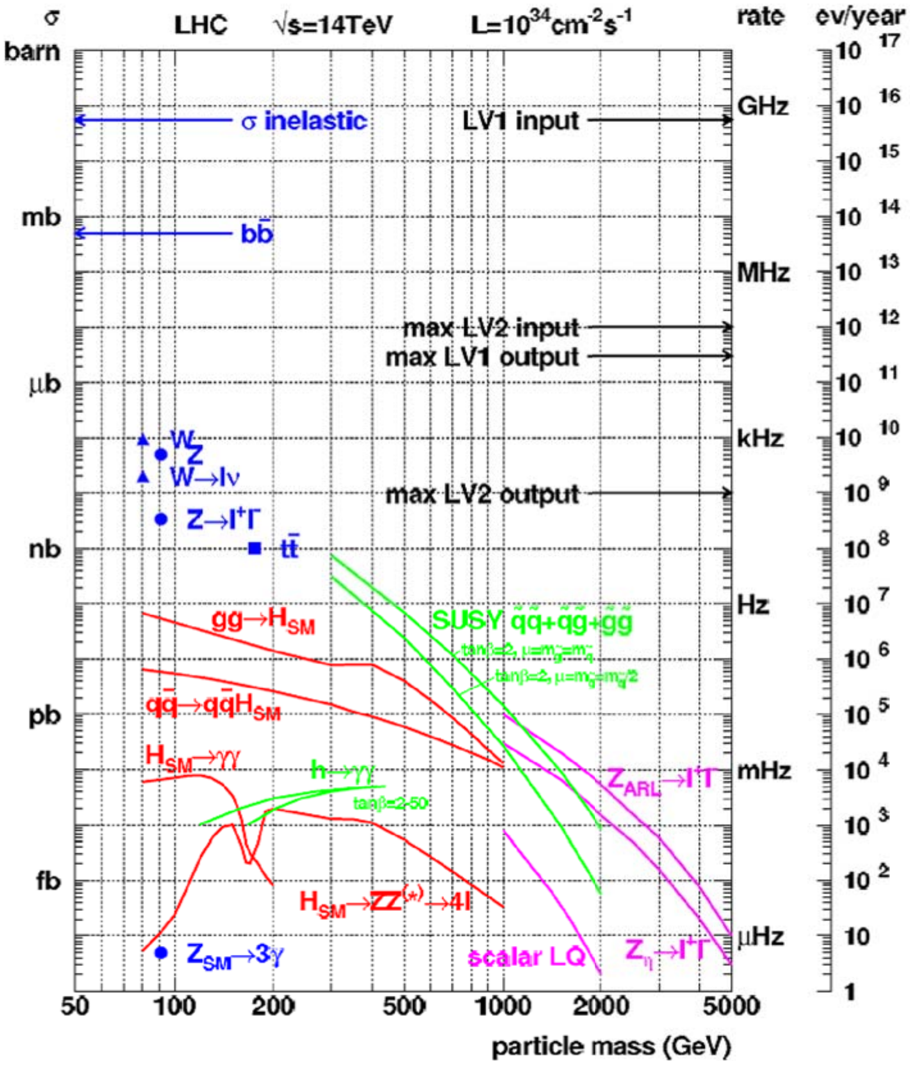

Figure 3.3: Proton-proton cross sections for some important physics processes expected at the LHC at the center of mass energy of 14 TeV

in the final state. For that reason neutralino is a good candidate for the dark matter of the universe. The rest of the cascade results in an abundance of leptons and jets. LHC experiments (ATLAS and CMS) target to search for SUSY signal which is the main objective of this thesis.

Another important physics goal of the LHC experiments is to provide further understanding of the physics of known particles. The LHC will produce large quantities of SM particles, enabling studies of the properties of the most recently discovered top quark (Tevatron, 1995 [32] and [33]) and CP violation, which are the two active topics of research carried out at other colliders currently in operation in the world. With the high energy Pb-Pb collisions, the observation of a new state of matter called *quark-gluon plasma* may be possible, which is a separation of hadrons into individual quarks predicted by the theory of QCD at high temperatures.

3.1.3 Design and Operation

The LHC comprises of a number of accelerator units as shown is Figure 3.4. Protons will be obtained by removing electrons from hydrogen atoms. Then, they will be injected from one of the two linear accelerators, LINAC2 (LINAC3 for lead ions) into the PS (Proton Synchrotron) which will then be used to provide a low energy beam (25 GeV) with the final bunch structure. The beams will be pre-accelerated using the SPS (Super PS), and then will be injected into the LHC near IP2/IP8 for the beam that circulates clock wise/counter-clock wise, where particles will be accelerated from 450 GeV to the nominal energy of 7 TeV (for proton beam) [34].

Inside the LHC accelerator, the particles circulate in opposite directions in two separate beam pipes. The diameter of the beam is reduced by focusing magnets before the beam enters every experimental interaction point to achieve high luminosity collisions. The cross section of the LHC dipole is shown in Figure 3.5. The two beam pipes are surrounded by shells of superconducting coils creating the magnetic field which keeps the beams to follow a circular path. The entire dipole rests inside a vessel filled with liquid Helium to enable operation at temperature below 2 K. In total, 40,000 of such cryogenic units are placed around the 27 km circumference LHC ring.

Particles inside the beam are grouped into approximately cylindrical bunches with a diameter

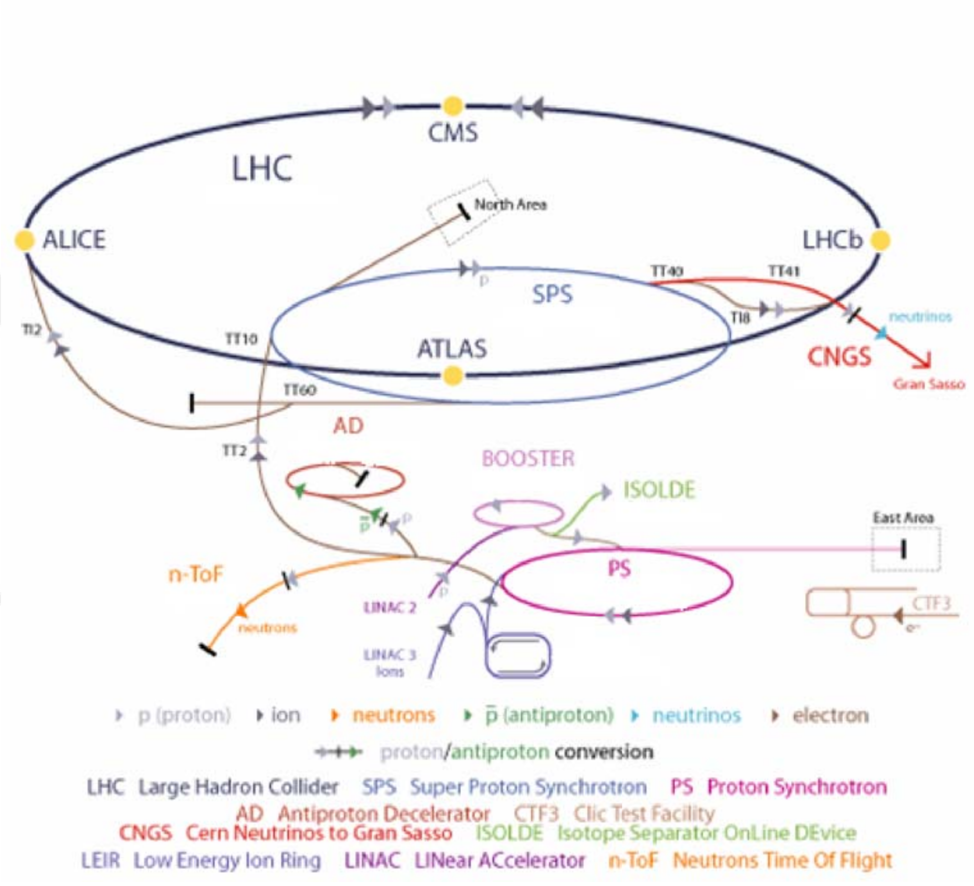

Figure 3.4: Accelerator complex at CERN

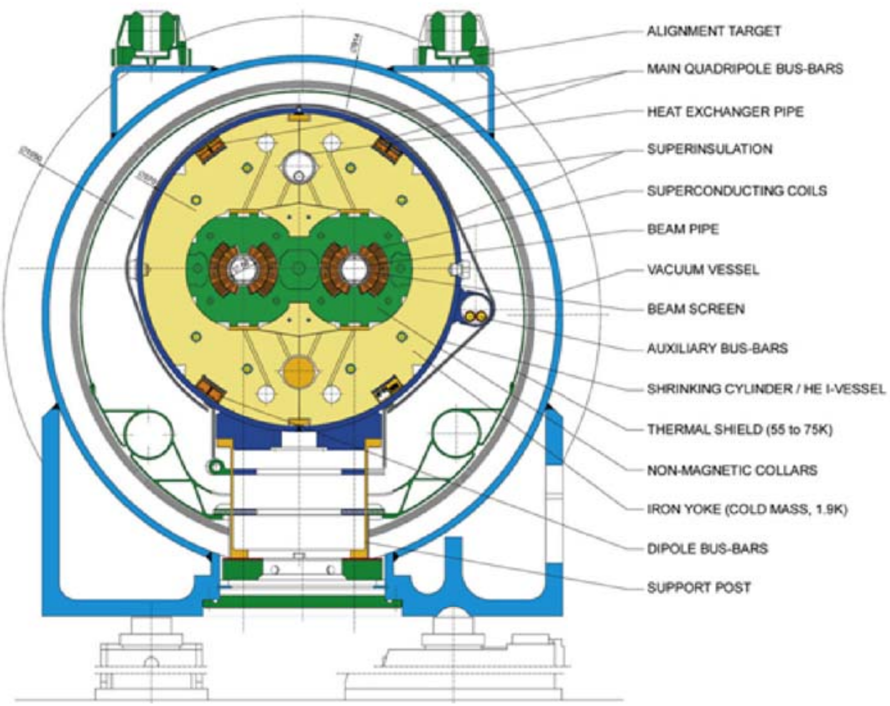

Figure 3.5: Schematic view of the cross section of the LHC dipole

and a length of approximately 16 μm and 8 cm at the interaction point respectively. The LHC filling scheme for the proton beam assuming a bunch separation of 25 ns. Trains of 72 occupied and 12 empty bunches, each made in one PS cycle, are used to fill the SPS with an injection kicker gap of 220 ns. A longer gap of 950 ns is allocated after 3-4 consecutive trains for injection of beam into the LHC. Approximately 4 cycles of SPS fill the entire LHC, requiring nearly 3 minutes. Longer gaps between bunch trains and one missing train at the end of the LHC cycle allow for the synchronisation, resetting of electronics, and obtaining calibration data in the absence of collision events. There will be 3564 spaces available during each LHC cycle, 2808 will be filled with actual particle bunches.

The LHC proton and lead parameters are summarised in Table 3.1. The event rate is proportional to the luminosity multiplied by the cross section of the scattering events. At a center of mass energy of 14 TeV, the total p-p collision cross section is 120 mb. However, around 50 mb of this will be elastic or single diffractive scattering, which does not produce any particles which enter the detector region. Hence, taking into account the bunch spacing of 25 ns and the fraction of filled bunches in the run of approximately 0.8, the average number of inelastic p-p interactions expected during each beam crossing is about 20 at full luminosity. In addition, the short bunch spacing of 25 ns results in further *pile-up*, which comes from the soft remnants overlapping from the two previous bunch crossings and some early effects from the subsequent one. The structure of the Pb beam does not impose such pile-ups; however, due to the number of nuclei involved at each collision event the detector will suffer from much higher particle occupancies.

Table 3.1: LHC beam parameters for nominal proton and heavy ion runs.

Beam Parameters	Proton	Lead	Units
Design Luminosity	10^{34}	10^{27}	$cm^{-2}s^{-1}$
Energy at collision	7	2.56	TeV
Number of particles per bunch	1.15×10^{15}	7×10^{7}	-
Bunch spacing	25	99.8	ns
Number of collision events per beam crossing	~ 20	~ 7	-

In 2009 fall, the LHC will undergo a series of accelerator and detector commissioning stages and pilot runs at the beginning of its operation. Regular physics runs will start with a period of low luminosity beams which will contain fewer protons, possibly with larger bunch spacing, enabling detector calibration and alignment and physics studies in a clean environment with less pile-up. The luminosity during this phase is expected to be $2 \times 10^{33} cm^{-2} s^{-1}$, which will only produce 4 inelastic interactions per beam crossing on average, with an integrated luminosity over one year of approximately 10 fb^{-1} (high luminosity runs will provide $\sim 100 fb^{-1}$ per year). This period will be important in thoroughly analyzing and understanding the current knowledge of particle physics, and may also be sufficient for the discovery of new physics.

3.2 The CMS Detector

3.2.1 Overview

The design of the CMS detector has focused on mainly three aspects: high *granularity*, *hermiticity*, and *radiation hardness*. Signatures of important physics processes will appear in the form of high transverse momentum (p_T) objects. High granularity is necessary to measure precisely the position of these objects, and also to individually separate the energy deposition of objects in pile-up events. Hermiticity is particularly important when non-interacting particles including those from possible new physics are involved, since their signature will be the missing energy of the entire system. The high luminosity LHC environment will impose an additional challenge to the sensors and the readout electronics, as they are required to survive the high radiation environment as well as to deliver fast enough response to cope with the collision rate of 40 MHz ([35] and [36]).

The major subdetectors of the CMS detector is shown in Figure 3.6. It has a multi-layered cylindrical barrel structure enclosing the beam pipe and endcaps to complete the hermetic coverage. Starting from nearest point to the beam interaction, the constituent sub-detectors are the Tracker, the Electromagnetic Calorimeter (ECAL), the Hadronic Calorimeter (HCAL) and the superconducting solenoidal magnet delivering axially a magnetic field strength of 4 Tesla, followed by layers of Muon Chambers interspersed with iron Return Yokes.

The main features of the CMS subdetectors are good charged particle tracking, good muon identification, good electromagnetic energy resolution, and good missing transverse energy, E_T^{miss} and jet resolution.

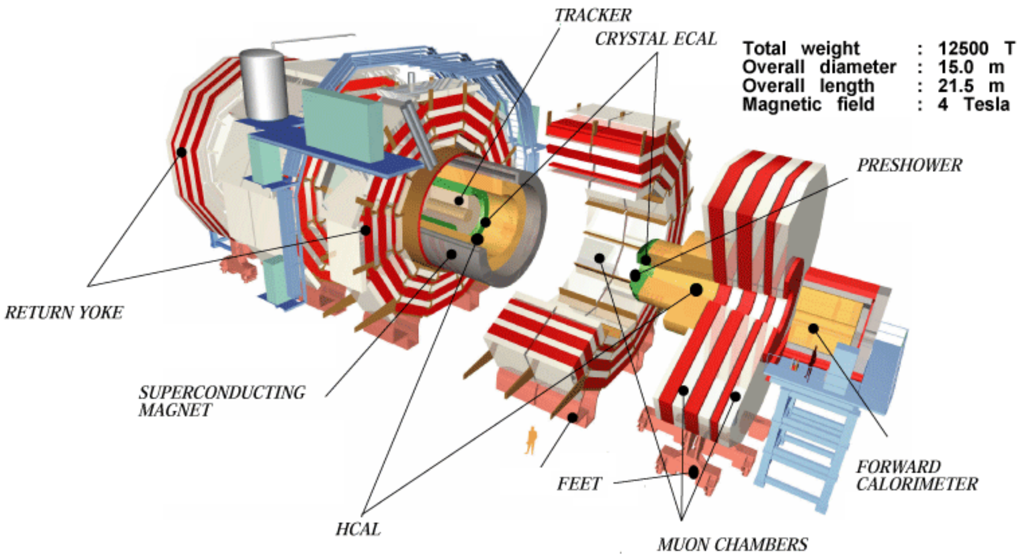

Figure 3.6: An illustration of the major components of the CMS detector

Characterization of particles is achieved by examining their interaction with different subdetectors as illustrated in Figure 3.7. All electrically charged particles leave a trail of ionization in the central silicon tracker, and photons/electrons and hadrons deposit all of their energy in the ECAL and HCAL respectively. Muons, which have low interaction rate in the calorimeters, are identified by the muon tracking system at high radius; the magnetic field acts in opposite direction outside the solenoid hence the muon track points back to its vertex.

3.2.2 The CMS Coordinate System

In the CMS coordinate system, the origin is centred on the nominal interaction point with the x-axis pointing radially inward towards the center of the LHC ring, the y-axis pointing vertically upward and the z-axis pointing along the beam direction. The azimuthal angle,ϕ, is measured from the x-axis in the x-y plane. The polar angle, θ, is measured between the line connecting the coordinate to the interaction point and the z-axis. *Pseudorapidity*, η, is defined as $\eta = -ln(tan(\frac{\theta}{2}))$. Distance in the $\eta - \phi$ plane is measured as $\Delta R = \sqrt{(\Delta\eta)^2 + (\Delta\phi)^2}$. Momenta and energy measured transverse to the beam, p_T and E_T respectively, are computed from their x and y components (i.e. $E_T^2 = E_x^2 + E_y^2$, for massless particles). The energy imbalance measured in the transverse plane is denoted by E_T^{miss} (missing transverse energy). The transverse component of momentum is calculated as $p_T = psin\theta$.

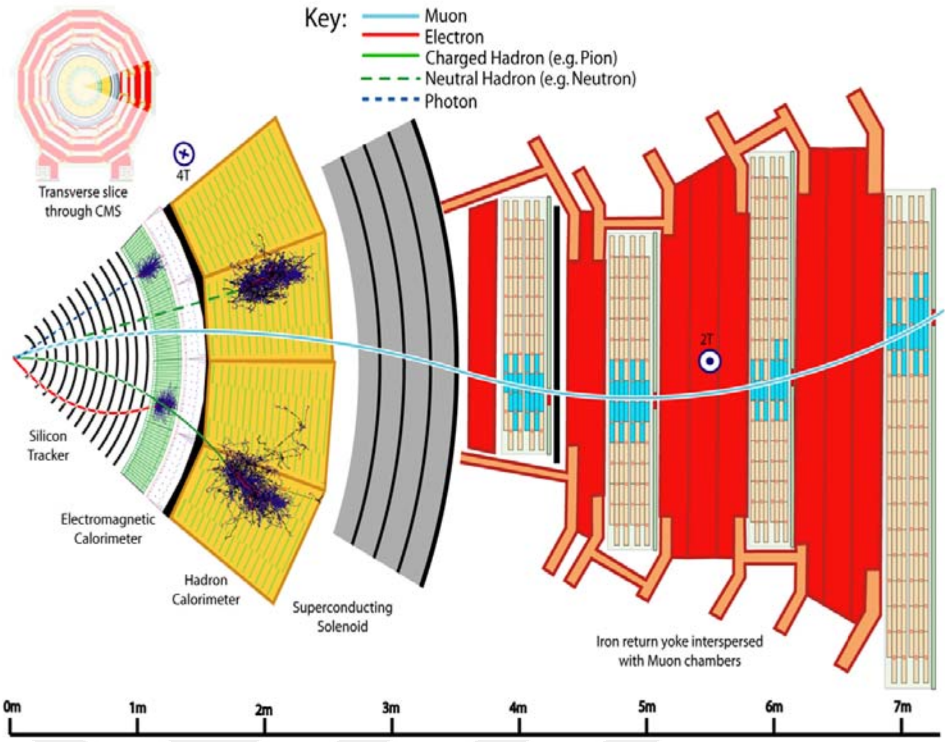

Figure 3.7: An illustration of transverse slice of CMS detector with passages of particles through the subcomponents

3.2.3 The Tracker

The closest sub-detector to the beam interaction point is the silicon tracking system. It measures the trajectories and momenta of charged particles such as high energy muons, electrons, and hadrons up to $|\eta| < 2.4$ [37]. The tracker records the paths (tracks) of the charged particles which are used for momentum calculations through a magnetic field. In the tracker, two different silicon technologies are used: pixel and microstrip detectors. Close to the beam pipe the high particle flux requires small pitch pixel detectors whereas further out the occupancy drops sufficiently to allow silicon microstrip detectors to be used. As particles travel through the tracker, the pixels and microstrips generate electric signals which are then amplified and detected. The tracker, shown in Figure 3.8, has an outer radius of 110 cm, is 540 cm long and has 75 million readout channels.

The pixel detector records the paths of particles emerging from collision (especially short-lived particles), shown in Figure 3.9, consists of 3 barrel layers with 2 pairs of endcap disks

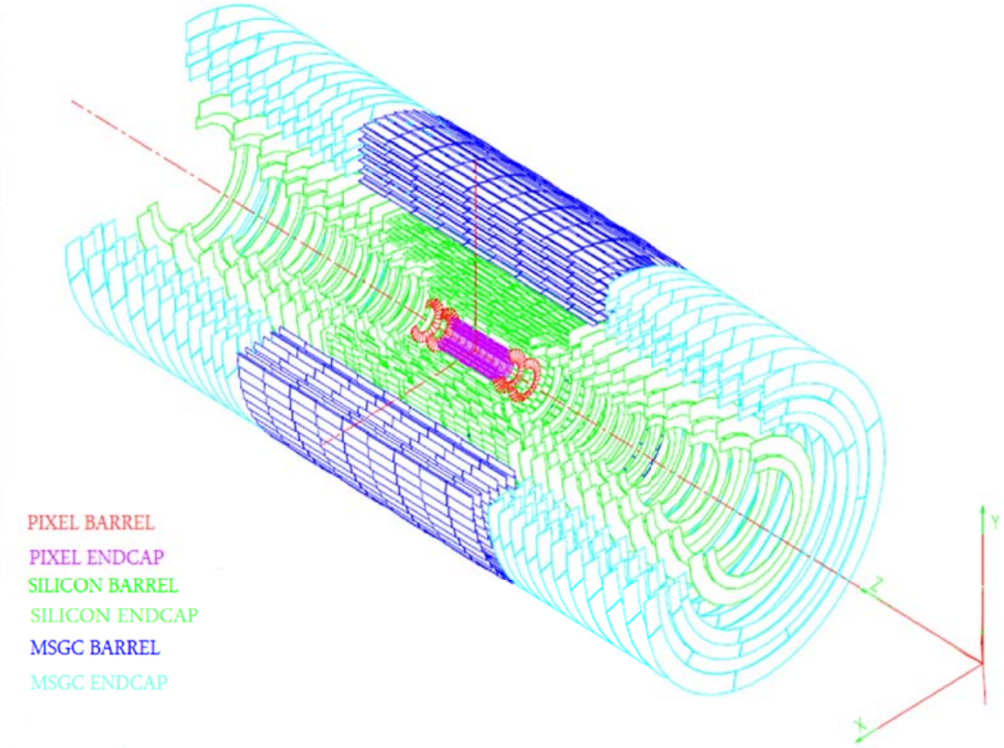

Figure 3.8: Layout of the entire tracker

and provides two hit coverage up to $|\eta| = 2.2$. The barrel layers are located at radii of 4.4 cm, 7.3 cm and 10.2 cm and are 53 cm long. The two endcap disks are located at $|z| = 34.5$ cm and 46.5 cm with radii of 6 cm to 15 cm.

In order to maximize the vertex resolution, the pixel pitch has a surface area of $\approx 100 \times 150$ mm^2. The pixel spatial resolution is increased by using analogue signal interpolation of the charge sharing induced by the large Lorentz drift in the magnetic field. Thus the barrel pixel layers are collinear to the beam and the endcaps are arranged in a turbine-like geometry with blades rotated by 20^o. The spatial resolution is 10 μm in $r - \phi$ and 20 μm in z giving a vertex resolution of $\sim 40\mu m$.

The silicon microstrip tracker surrounds the pixel detector and covers the range $|\eta| < 2.4$. The strip tracker is split into 2 systems, inner and outer, each of which has barrel and endcap sections. Most detector layers utilize single sided microstrips but some use *stereo* modules consisting of two tilted back-to-back modules which provide a 3D hit measurement.

The modules used in the various parts of the silicon tracker should be explained. The Tracker Inner Barrel (TIB) is composed of 4 microstrip layers covering $|z| < 65$ cm, where the first 2 layers use stereo modules with a stereo angle of 100 mrad. The silicon sensors have a thickness of 320 μm and a length of 10 cm. Point resolutions of 23-34 μm in $r - \phi$ and 230 μm in z are obtained depending on the layer. Each inner endcap, Tracker Inner Disk (TID), has three microstrip layers, the first two of which have stereo modules. The microstip detectors are 320 μm thick with a minimum length of 10 cm. A point resolution of 23-34 μm in $r - \phi$ and 230 μm in z is obtained.

The outer barrel system, Tracker Outer Barrel (TOB), comprises 6 layers covering the range $|z| < 110$ cm with the first two layers using stereo modules. The point resolution varies from 35-52 μm in $r - \phi$ and is constant at 530 μm in z. The Tracker EndCaps (TEC) comprise 9 layers over the range $120 < |z| < 280$ cm. The first two and the fifth disks have stereo modules. The microstrips have a thickness of 320-500 μm and a length of 25 cm. A point resolution of 35-52 μm in $r - \phi$ and 530 μm in z is obtained.

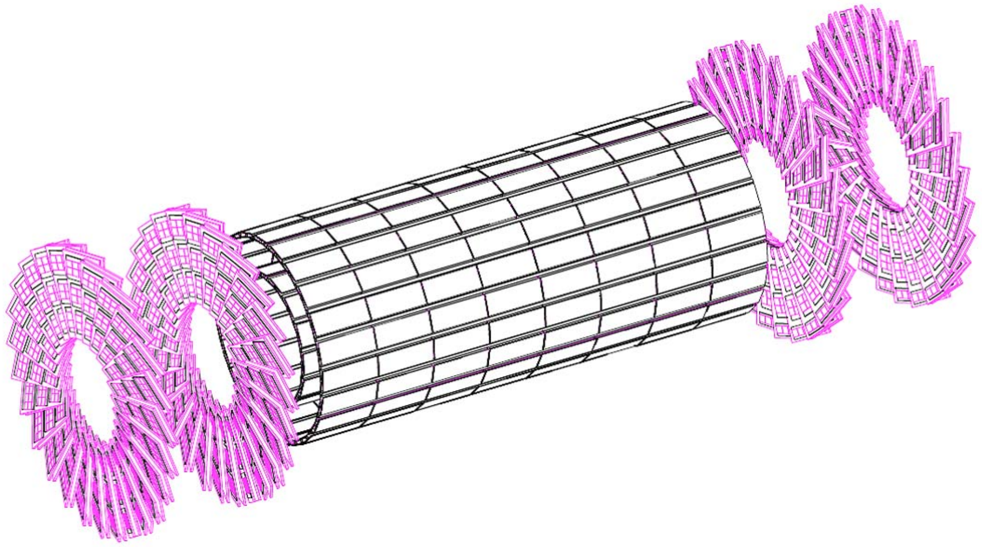

Figure 3.9: Layout of the pixel detectors in the CMS tracker

3.2.4 The Electromagnetic Calorimeter

Surrounding the silicon tracker is the electromagnetic calorimeter (ECAL) which measures energies of particles. As of particular interest, energies of electrons and photons (they appear in decay channels of Higgs boson and new physics searches) are measured. The ECAL is divided into a barrel and 2 endcap sections, shown in Figure 3.10. CMS has chosen 7600 scintillating lead tungstate ($PbWO_4$) crystals to provide precise electron and photon energy measurement. Lead tungstate crystals are radiation hard, have short radiation lengths (X_0 = 0.89 cm) and are fast (80 percent of light is emitted within 25 ns). This choice allowed a fast, fine grained and compact ECAL which could be placed inside the coil. $PbWO_4$ crystals yield a relatively low number of photons (30/MeV) and so need to be read out by *photodetectors* with an intrinsic gain as *photo multipliers* cannot operate in the high magnetic field [38].

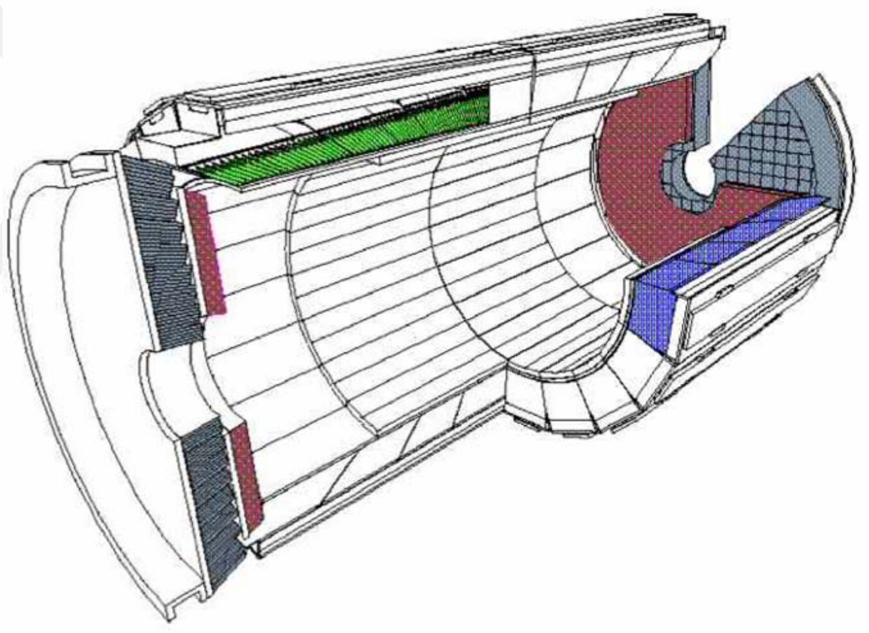

Figure 3.10: A 3D view of the CMS electromagnetic calorimeter

The ECAL barrel (EB) begins at a radius of 129 cm and covers the range $|\eta| < 1.479$. 61,200 crystals are grouped together to form one of 36 identical *supermodules*. Each supermodule covers half of the barrel length. The crystals are mounted 3^o off axis from the nominal vertex position to avoid energy leakage between crystals. Each crystal measures $22 \times 22 \times 230$ mm^3 and covers an area of $\Delta\eta \times \Delta\phi = 0.0174 \times 0.0174$. These crystals are read out by silicon avalanche photodiodes (APDs).

The ECAL endcaps (EE) are located 314 cm from the vertex and cover the range $1.479 < |\eta| < 3.0$. Each endcap is constructed from two *Dees* consisting of semi-circular aluminium plates mounting crystals in groups of 5×5 crystals, known as *supercrystals*. The endcaps crystals are tilted off axis in an x-y grid. A total of 21,528 crystals of dimensions $28.6 \times 28.6 \times 220$ mm^3 are used in the endcaps. Vacuum *phototriodes* are used for the endcap readout as they are more radiation hard than APDs.

A preshower detector comprised of two planes of lead absorber followed by silicon strip detectors is placed in front of the endcaps, covering $1.48 < |\eta| < 2.6$. These are used to help identification of neutral pions in the endcap region where the average pion energy is high enough to make resolving individual photons difficult resulted by the calorimeter granularity.

3.2.5 The Hadronic Calorimeter

Surrounding the electromagnetic calorimeter is the hadronic calorimeter (HCAL) which measures energies, positions, and arrival times of hadrons such as proton, neutron, kaon, and pion. It provides indirect measurements of non-interacting uncharged particles such as neutrinos. The HCAL was placed inside the magnet coil in order to minimize non-Gaussian energy resolution tails and to provide good containment. This required a compact absorber and left little room for the active medium. Brass was chosen for the absorber because it is non-magnetic and has a short interaction length (λ). Tile/fibre technology was chosen for the active medium together with wavelength-shifting fibre readouts [39]. The barrel section, denoted HB, spans the region $|\eta| < 1.4$ and is read out in towers of $\Delta\eta \times \Delta\phi = 0.087 \times 0.087$ in a single longitudinal sampling. The HB has 15 brass plates comprising 6.5 λ thus additional layers, known as the hadron outer (HO), are placed behind the coil, hadron outer (HO), to act as a tail catcher. This covers the region $|\eta| < 1.26$ and uses the same tower geometry as the barrel. The HO extends the barrel HCAL depth to over 10 λ.

Hadron endcap (HE) disks are located either side of the solenoid coil and span the region $1.3 < |\eta| < 3.0$ with towers varying in size from $\Delta\eta \times \Delta\phi = 0.087 \times 0.8 \times 0.35 \times 0.8$.

To extend the η coverage, a forward calorimeter, hadron forward (HF), is located at the edges of CMS covering the region $3.0 < |\eta| < 5.0$. This detector is constructed from steel and quartz fibre. These materials lead to shorter and narrower jets which is useful in the high flux forward region. The sections of the HCAL are shown in Figure 3.11.

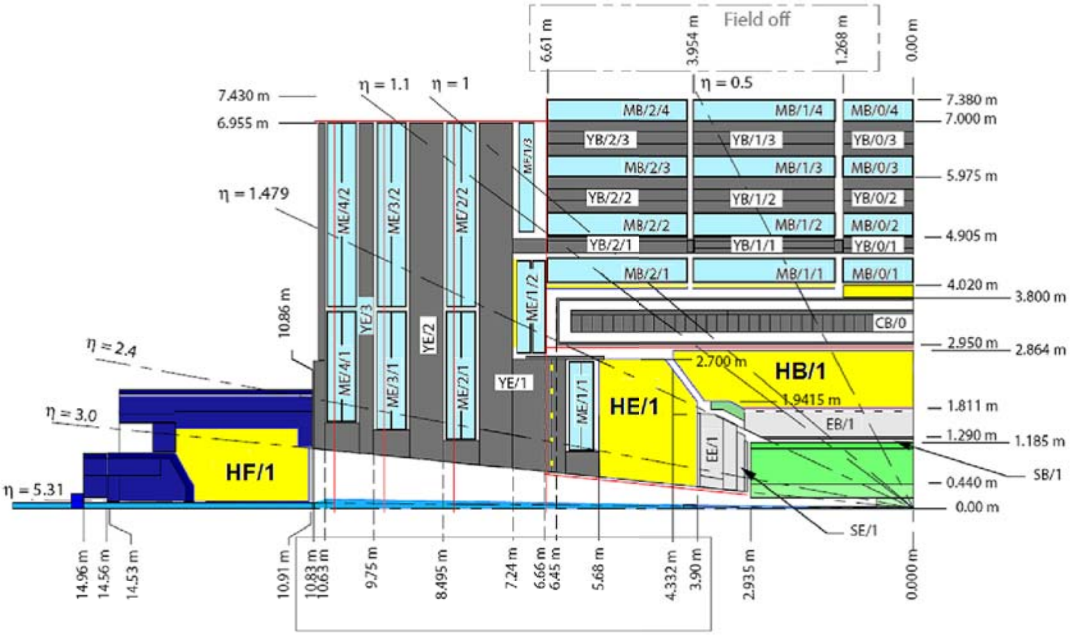

Figure 3.11: Longitudinal view of a quarter of the CMS detector. The HCAL (colored in yellow) is composed of three main parts, HB, HE and HF, and additional scintillators (HO) outside the magnet. The muon chambers (colored in light blue) are mixed with the iron return yoke

3.2.6 The Muon System

The Muon system provides measurements of muons which are like electrons and positrons but 200 times heavier in the range of $|\eta| < 2.4$ as shown in Figure 3.11 and 3.12. Since muons can penetrate several meters of iron without interacting, unlike most particles they are not stopped by any of CMS calorimeters. Therefore, muon detectors to detect muons are placed at the very edge of the experiment where they are the only particles likely to register a signal. Detectors are placed at four layers or stations in the barrel and endcap sections of the iron flux return. Three different types of gaseous detector are used due to the varying radiation and magnetic environments. The barrel section, covering $|\eta| < 1.2$, uses drift tubes (DT). The high muon and neutron background environment of the endcaps, $0.8 < |\eta| < 2.4$, means cathode strip chambers (CSC) are used instead of DTs. Resistive Plate Chambers (RPC) are used in both the barrel and part of the endcaps, $|\eta| < 2.1$ [40].

The barrel region contains 250 chambers of up to 12 planes of drift tubes. The individual drift tubes have a cross section of 42×13 mm^2 and are filled with Ar and CO_2. Each drift tube consists of a central anode wire surrounded by aluminum cathodes. The induced charge has a maximum drift length of 2 cm or 400 ns. Each station provides a muon vector with a resolution of 100 μm in ϕ and 1 mrad in direction.

The two endcaps use 468 CSCs each of which is trapezoidal and contains 6 gas gaps. Each gap has a plane of radial cathode strips with perpendicular anode wires. The muon position is measured from the charge sharing of the radial cathode strips. Each station provides a muon vector with a resolution of ~ 200 μm in ϕ and 10 mrad in direction.

The RPCs consist of a gas gap enclosed by two graphite-coated bakelite plates. The graphite forms a cathode with an aluminum strip used to read out the generated signal. The RPCs have a time resolution of ~ 1 ns which makes them useful for identifying the bunch crossing time.

3.2.7 The Trigger System

At $\sqrt{s} = 14$ TeV the proton-proton inelastic cross section is roughly 100 mb. At design luminosity ($L = 10^{34} cm^{-2} s^{-1}$) this results in one billion inelastic interactions per second. Given the LHC bunch crossing interval of 25ns (40 MHz), this yields an average of 20 inelastic collisions per bunch crossing (event) [41]. Given that CMS has ~ 10^8 detector channels and one event comprises ~ 1 MB of data this would give rise to a data rate of 100 TB per second. Storage systems place a limit of 150-200 MB per second, hence an online selection, *trigger*, is used to reduce the event rate to ~ 100 Hz. Moreover, there is no way that data from all these events could be read out, and even if they could, most would be less likely to reveal new phenomena; they might be low-energy glancing collisions for instance, rather than energetic, head-on interactions. Therefore, one needs a trigger that can select the potentially interesting events, such as those which will produce the Higgs particle or SUSY sparticles.

The CMS trigger is divided into two parts; a fast hardware L1 (Level-1) trigger and a software High Level Trigger (HLT). The L1 trigger uses custom-built electronics hardware and reduces

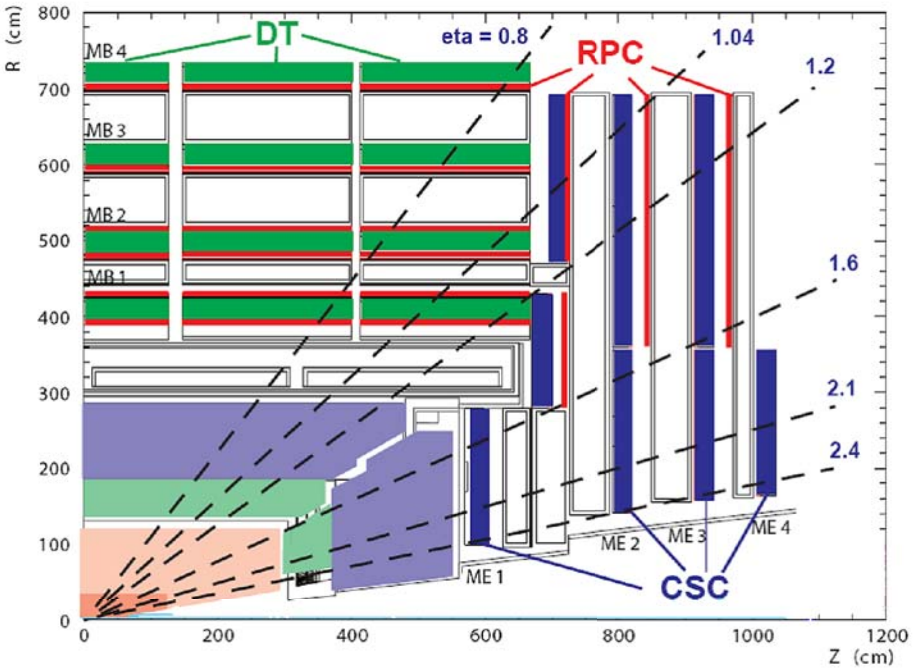

Figure 3.12: Layout of one quarter of the CMS muon system. The RPC system is limited to $|\eta| < 1.6$ in the endcap, and for the CSC system only the inner ring of the ME4 chambers have been deployed

the event rate from 40 MHz to 100 kHz. The HLT runs on a commodity computing farm and reduces the rate further to $\sim$ 100 Hz for offline storage.

A period of 3.2 μs is enough for the L1 decision, but the signal transit time between the detector and the trigger hardware reduces this to less than 1 μs. The L1 trigger only uses calorimeter and muon information with the rest of the event stored in a memory until the decision is reached.

The L1 trigger has separate calorimeter (regional and global) and muon triggers, that are all fed into a global trigger. The regional calorimeter trigger readouts both the ECAL and HCAL calorimetry in coarse grained samples of one HCAL tower or 5×5 ECAL barrel crystals, which corresponds to an area of $\Delta\eta \times \Delta\phi = 0.087 \times 0.087$. The regional calorimeter trigger identifies jet, photon and electron candidates (primitives).

The L1 jet trigger sums energy in a 4×4 array of towers which are then combined into a 3×3 array. Thus a jet is formed from a 12×12 array of towers corresponding to approximately a square unit in the $\eta - \phi$ plane. An examplary jet L1 algorithm, which is τ-jet algorithm can be used to imagine τ-jet-like shapes in towers of ECAL. Central jets are accepted to be τ-jets as illustrated in Figure 3.13.

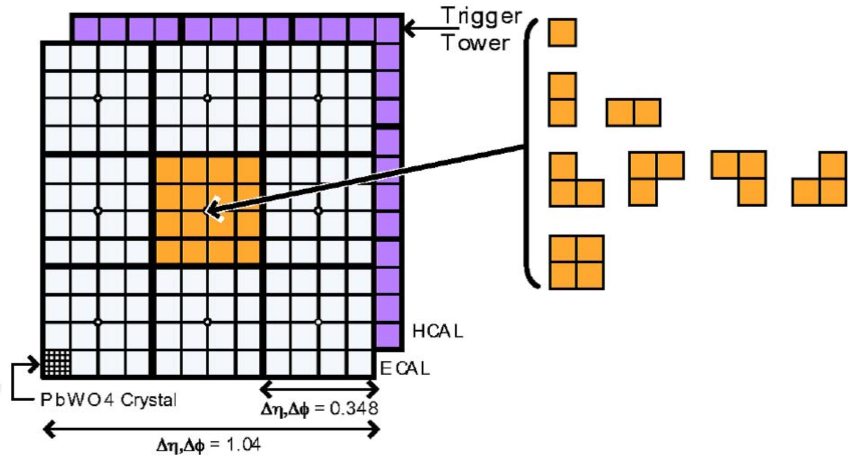

Figure 3.13: The L1 τ-jet trigger algorithm showing the acceptable τ-like shapes in the central region of ECAL

The Global Calorimeter Trigger (GCT) combines the information from the regional calorimeter triggers and creates an transverse energy ordered list of each primitive type. The global L1 trigger combines the information from the GCT and muon trigger and uses threshold cuts on the primitives to make the accept/reject decision.

Once accepted by the L1 trigger the event is readout and combined by an event builder via a switched network capable of a data transmission rate of 1 TB per second. Once combined the event is sent to a processor in the computing farm, which runs the HLT algorithms and makes the accept/reject decision. Scalability of the system is ensured with the addition of additional event builders and processor units which use the high speed network to communicate. As such during the low luminosity phase only a fraction of the total system will be implemented. As the data rate increases more event builders and processing nodes will be added.

By using a pure software high level trigger maximum flexibility of the reconstruction and triggering criteria can be achieved. The HLT rejects events as soon as possible by using the minimum of event information and by performing partial event reconstruction. Full granularity calorimeter information is used, followed by the tracker pixel detector and finally the full event is reconstructed using all detectors. If an event passes the HLT it is passed to the offline computing system together with a list of all primitives that passed the thresholds, the trigger bits.

3.3 CMS Computing Model

The aim of the CMS Computing Model is to cope with computing requirements for storage, processing and analysis of CMS detector data. After first year of the start-up (foreseen to be 2010 or 2011), there will be a need of 34,7 PB disk space and 59.5 PB tape space in order to store and process run data. The CMS Computing Model meets computing requirements by making use of the hierarchy of computing *Tiers* (Figure 3.14) as described in the CMS Computing Project [42].

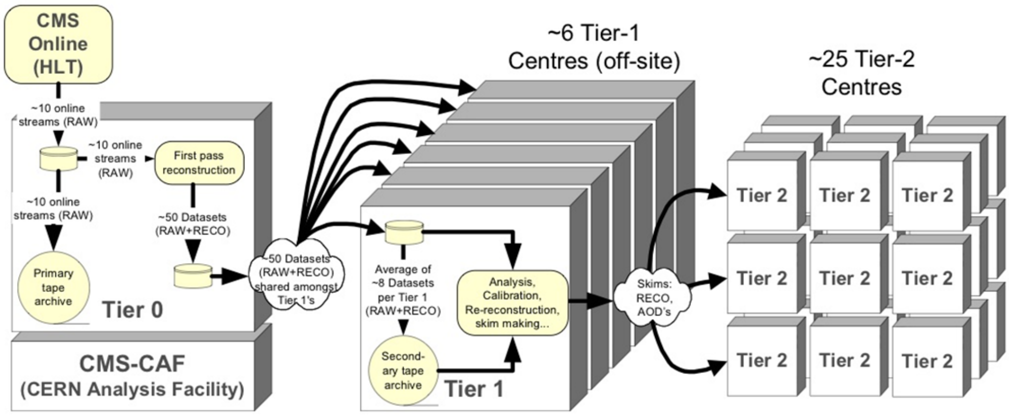

Figure 3.14: Tiered architecture and data flow of the CMS Computing Model

3.3.1 Tiered Architecture

A single Tier-0 center at CERN accepts data from the CMS Online Data Acquisition System, archives the data and performs prompt first pass reconstruction. Online streams of data arrive in a 20 day which is called input buffer. They are split into *Primary Datasets* that are then linked together to form reasonable file sizes. Primary Dataset RAW data is archived to tape at Tier-0 and sent to reconstruction nodes in the Tier-0. Resultant RECO Data is linked with matching RAW data to form a distributable format *FEVT* (Full Event). RECO data is archived to tape at Tier-0. FEVT are distributed to Tier-1 centers (Tier-1s subscribe to data). AOD copy is sent to each Tier-1 center.

A CMS CERN Analysis Facility provides access to the full RAW dataset and focusses on the latency-critical detector, trigger, calibration and analysis activities. Activities are directly coupled to the operations and performance of the CMS detector. In particular, CMS-CAF is responsible of diagnosing detector problems, providing trigger performance services such as reconfiguration, optimization and the testing of new algorithms, and calibrations required by the high level trigger or the initial reconstruction pass. These activities will have the highest priority at the CAF and will take priority over all other activities. The other tasks are supporting the analysis of CMS wide and CERN based users, recording and book keeping services, provide the central information repository for data management, storing conditions and calibration data, providing the main software repositories and the documentation repositories, and other services associated with all Tier-1 centers.

A set of large Tier-1 centers in CMS collaborating countries provide services for data archiving, reconstruction, calibration, skimming and other data-intensive analysis tasks. Tier-1s receive custodial data (FEVT and AOD) from Tier-0. Currently stored dataset are kept on disk and other bulk data mostly stored on tape with disk cache for staging. The main task of Tier-1s to serve data to analysis groups running selections, skims, and test reprocessing. Most analysis products are sent to Tier-2s for iterative analysis works.

A more numerous set of Tier-2 centers (including Turkish Grid services provided by TUBITAK ULAKBIM), smaller but with substantial CPU resources, provide capacity for analysis and Monte Carlo simulation. Tier-2 centers rely upon Tier-1s for accessing to large datasets and securing storage of the new data products they produce. Each Tier-2 is associated with a particular Tier-1 center. Three types of use of Tier-2 resources are worth of discussing: local community use that is some fraction of the Tier-2 center resources will be fully under the control of their own local users, CMS controlled use which is Tier-2 resources will also be used for organized activities allocated top-down by CMS, and opportunistic use by any CMS member.

Tier-3 centers provide resources for local groups. Tier-3 sites are often relatively small computing installations that serve the needs of the local institutions user community. The facilities at these sites do not form part of the negotiated baseline resource for CMS, but they are important component of the analysis capability of CMS as they provide a location and resources for a given institute to perform its work with substantial freedom of action.

3.3.2 Worldwide LHC Computing Grid

The mission of the Worldwide LHC Computing Grid (WLCG) project is to build and maintain a data storage and analysis infrastructure for the entire high energy physics community that will use the LHC [43]. The data from the LHC experiments including CMS will be distributed over the world, according to a tiered architecture discussed before. A primary backup will be recorded on tape at CERN, the Tier-0 center of LCG. After initial processing, this data will be distributed to a series of Tier-1 centers, large computer centers with sufficient storage capacity. The Tier-1 centers will make data available to Tier-2 centers, each consisting of one or several collaborating computing facilities, which can store sufficient data and provide adequate computing power for specific analysis tasks.

The Grid computing connects computers that are scattered over a wide geographic area, allowing their computing power to be shared. Just as the World Wide Web enables access to information, computer grids enable access to computing resources. These resources include data storage capacity, processing power, sensors, visualization tools and more. Thus, grids can combine the resources of thousands of different computers to create a massively powerful computing resource, accessible from the comfort of a personal computer.

The grid was designed to provide an advanced computing infrastructure suitable for collaborative problem solving within science and engineering. Resources, both computational and storage, were shared among collaborating institutions within a dynamic *Virtual Organisation* (VO). The VO comprises individuals based at different institutions around the world all working towards a common goal. The ultimate aim of grid computing was to provide ever present access to resources such that the user did not need to know where their work was carried out. They simply interacted with the grid and resources were provided. The grid was named by analogy with the power grid: users should consume computing power much as they consume electricity, without knowing the details of how or where it was generated.

The Worldwide LCG Project [44] depends upon several other projects for the supply of much of the specialized software used to manage data distribution and access as well as job submission and user authentication and authorization, known as the Grid *middleware*. These projects include *Globus*, *Condor*, *the Virtual Data Toolkit* and *the gLite* toolkit. The majority of the computing resources made available by the members of the collaboration are operated as part of the EGEE (Enabling Grids for E-sciencE) Grid , a consortium of national Grid infrastructures and computing centres from 34 countries including Turkey. Other resources are operated as part of other grids, such as the Open Science Grid (OSG) in the United States and the Nordic Data Grid Facility (NDGF). Achieving interoperability between different grids without compromising on the functionality constitutes a major challenge.

The interaction that the Grid provides between users and components of a complex software, middleware architecture can be seen in Figure Figure 3.15. The User Interface (UI) was the gateway to the grid for users. The installed software allowed the user to manage data and submit computational jobs.

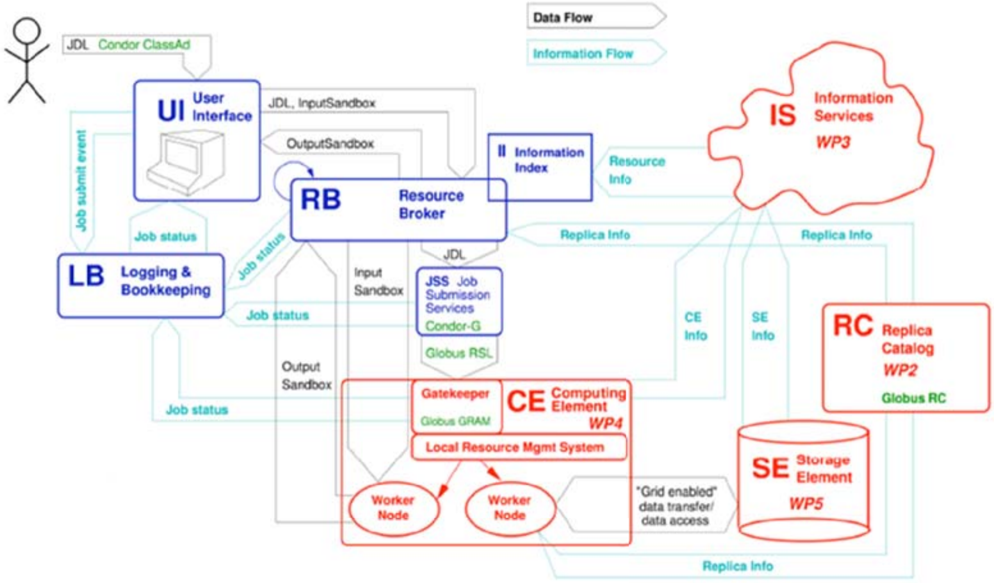

Figure 3.15: An overview of the major LCG components

Data was stored on a site *Storage Element* (SE) and recorded in a global file catalogue, known as the Replica Location Service (RLS) or *Replica Catalogue*. By using the client tools a user could copy data to/from and between SEs. Queries on the RLS were used for data discovery and location.

The Workload Management System (WMS) was provided by *the Resource Broker* (RB). The role of RBs was to accept users jobs and take responsibility for assigning them to a site for processing. *The Computing Element* (CE) controlled the processing at a site, receiving jobs from the RB and scheduling them for execution on the site *Worker Nodes* (WNs). *The Logging and Bookkeeping* (LB) system recorded changes in job state and was queried by users to determine the state of their jobs.

The Information Services (IS) listed all the RBs, CEs and SEs and was used by each system, and end users, to discover and obtain information about the other components.

CHAPTER 4

INTRODUCTION TO CMS SUSY ANALYSES

This chapter is dedicated to CMS software framework as a large collection of software tools which is necessary for any physics analysis effort with the CMS detector. SUSY PAT (Physics Analysis Toolkit) is an analysis tool adapted to needs of hadronic SUSY searches compromising both event cleaning and trigger selection tasks.

4.1 CMS Software Framework

The CMS collaboration has put effort in building a common framework and developing software packages which enable analysis tasks of any kind to be carried out in a consistent way. These analyses include evaluation of detector performance to analysis of data, from beam tests to physics simulation. Currently, the software is constantly being updated and the framework itself is still evolving; ultimately, there will be a solid framework with a set of common tools for all the CMS data analysis when the LHC switches on. The details of the CMS computing model and software architecture can be found in [36]. The current CMS software (CMSSW) framework can be described generally in two parts: Core Software and Physics Software, as shown in Figure 4.1.

4.1.1 Core Software

The overall collection of software, CMSSW, is built around a framework, an Event Data Model (EDM), and services needed by the simulation, calibration and alignment, and reconstruction modules that process event data so that physicists can perform analysis [45]. The framework and EDM facilitates the development and deployment of reconstruction and analysis software.

The CMSSW framework implements a software model wherein there is one executable, called *cmsRun*, and many plug-in modules which run algorithms. The same executable is used for both detector and Monte Carlo data. This framework is distinct from a more traditional approach in which several executables are used, one per task or set of tasks.

The CMS EDM is based on the concept of an event as a $C++$ object container for all raw and reconstructed data regarding a physics event. During processing, data are passed from one module to the next via the event, and are accessed only through the event. All objects in the event may be individually or collectively stored in ROOT files, and are thus directly accessible in ROOT [46]. ROOT is an object-oriented data analysis and statistics software package used for event data manipulation such as plotting, fitting, variable cutting, and so forth. Further, the framework also takes into account CMS detector description. As will be discussed later, both reconstruction and simulation tasks require the geometry of the detector including size, shape, material type, and position.

Data and Workflow Management tools of the CMSSW framework have many tasks which are being implemented. The most important ones are dataset bookkeeping and world wide transfer tasks (as discussed in WLCG subsection before), data location services, and many others [47]. HLT and Data Quality Monitoring (DQM) include event filtering, online selection, beam testing and others inside the CMSSW framework to be implemented later in physics analyses [48].

4.1.2 Physics Software

Event generators simulate creation of particles from a single proton-proton scattering event and their further decays until they reach a stable state within the scope of the experiment. The event data output from the generators are in the form of four-momentum vectors assuming the primary vertex position is at the center of beam axis. The proton-proton scattering event is then placed in a simulated detector environment with a suitable smearing of the vertex point. The interactions of the particles with the detector elements as well as the dead material are simulated and interpreted in terms of signal output from the read-out electronics. A variety of event generators are currently used in CMS. They range from general-purpose ones (*Pythia*, *Herwig*, *Sherpa*) to more specific ones (Matrix Element calculators like *ALPGEN*, *MadGraph*, *MCatNLO*, and so on) [49]. Two different types of simulation are currently being used in CMSSW framework. The first one is Full Simulation [50] which is based on Geant4 simulation toolkit [51] and the second one is named Fast Simulation [52].

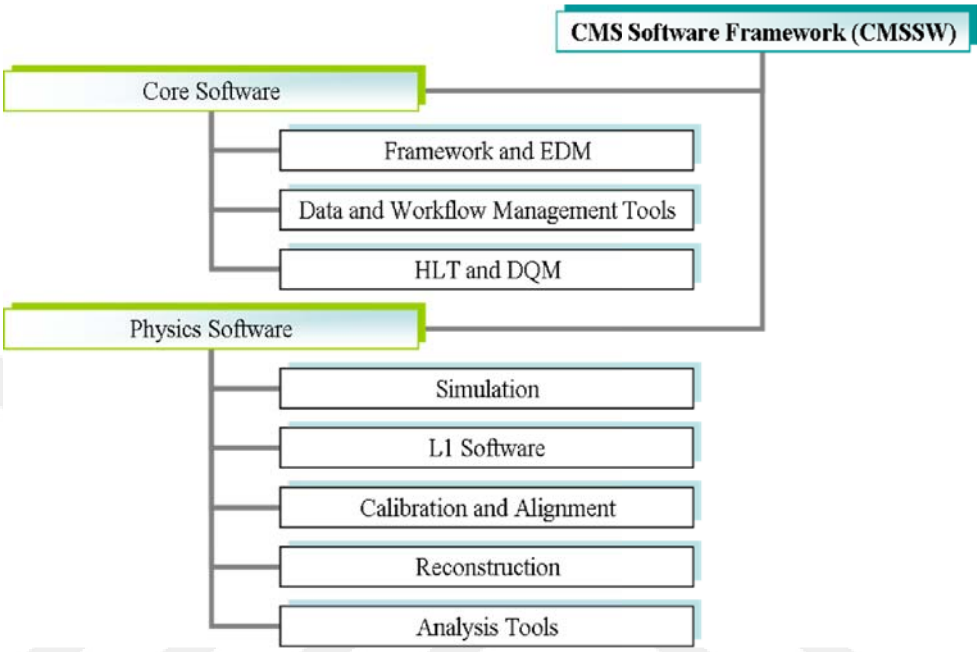

Figure 4.1: CMS software framework common tools

CMSSW covers L1 software option which makes appropriate L1 trigger decisions on event selection [53] and also detector calibration and alignment modifications are directly fed into the framework [54]. The offline event reconstruction in CMSSW is performed in multiple sub-systems which are responsible for reconstructing basic detector objects (e.g. tracks, hits, jets) and physics objects (e.g. electrons, muons, jets). The reconstruction of objects is carried out on demand, and a user has an access to the fully reconstructed objects through a common interface, ROOT [55].

Finally, CMSSW puts all those software tools together in a compact and easy-to-use framework with Analysis Tools for physics studies [56] and with a visualization tool, IGUANA for visualizing the event data in three dimensions [57]. The analysis tool of CMSSW framework, PAT, should be explained next.

4.2 PAT Algorithm

The Physics Analysis Toolkit (PAT) provides required algorithm tools for doing analyses in the framework of CMSSW. It meets both requirements of user-friendliness and flexibility, by providing an easy and configurable interface to the physics objects with cleaning options performed for the event as a whole [58]. In order to understand use case of PAT, one needs to first develop an understanding throughout the workflow of the toolkit layer-by-layer.

4.2.1 PAT Layers

The workflow of the PAT consists of three layers each having specific tasks to be implemented by a user as shown in Figure 4.2. The first layer, *Layer 0* takes the input standard reconstructed objects in CMSSW data format containing relevant output of reconstruction, RECO or in a more compact data format, AOD (Analysis Object Data). CMSSW data formats including RECO and AOD should be explained:

1. RAW: This is the output format of the HLT (High Level Trigger) farm. It contains data from all detector channels as well as the Level 1 and HLT bits. Target data size is the largest.
2. RECO: This is the output from event reconstruction of the RAW data, where, objects (tracks, vertices etc.) have been reconstructed and calibrations applied. The target event size is smaller than RAW data.
3. AOD: This is the output from further reconstruction (reprocessing) of RECO data. Physics objects (electron, muon, photon, jet, tau etc.) have been reconstructed and calibrations applied. This is expected to be the primary data used in analysis. The target event size is smaller than RECO and RAW data sizes.
4. TAG: This format indexes other event data and is the output from skimming of event data. This process is used to identify events with similar characteristics (b quark tagging, tau tagging). This format has not been implemented yet.

Layer 0 performs cleaning and association tasks to the content stored in either RECO or AOD data formats. Cleaning process includes removing duplicate physics objects and fulfilling necessary isolation criteria. Cleaning or object clean-up is called *cross cleaning* in the language of PAT and has special importance to this thesis, should be explained in detail in Cross Cleaning subsection. Further, MC matching, trigger matching including both L1 and HLT trigger primitives, jet and E_T^{miss} corrections, and b- and tau-tagging tasks can also be performed on this layer.

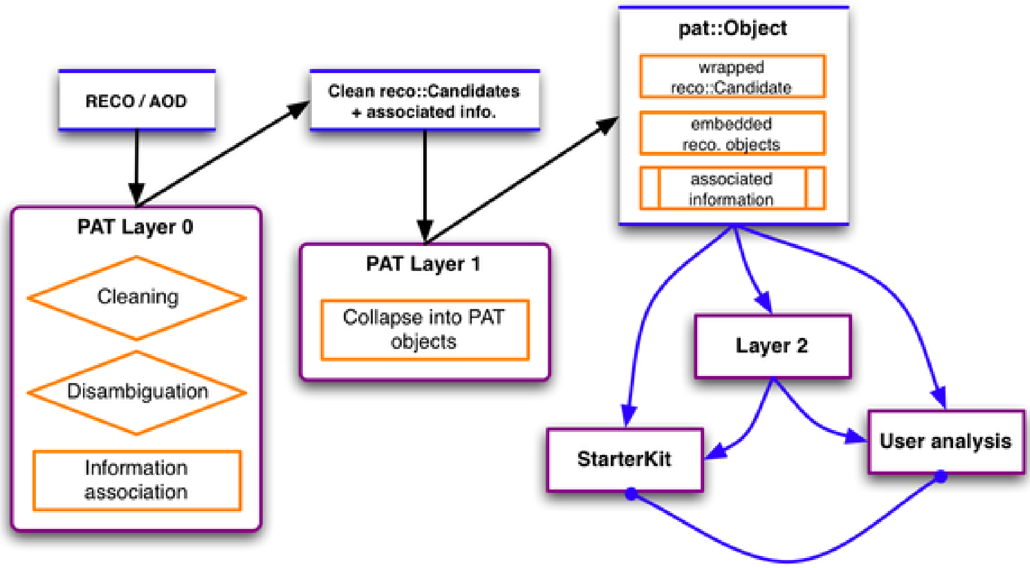

Figure 4.2: Workflow of PAT

The second layer, *Layer 1* takes the information gathered on Layer 0 and collapses into more compact objects, namely PAT objects as shown in Figure 4.3. These physics objects like muons, electrons, photons, jets and others are reconstructed and stored in a form of *reco::Candidate* model in the namespace of *pat::* as *pat::Muon*, *pat::Electron*, *pat::Photon*, *pat::Jet*, and for other objects which contain all relevant information including kinematics variables, isolation information, track information, vertices and so forth. The last layer is *Layer 2*, which is optional for analyses; one can define more specific event hypotheses in advance level with this layer [59].

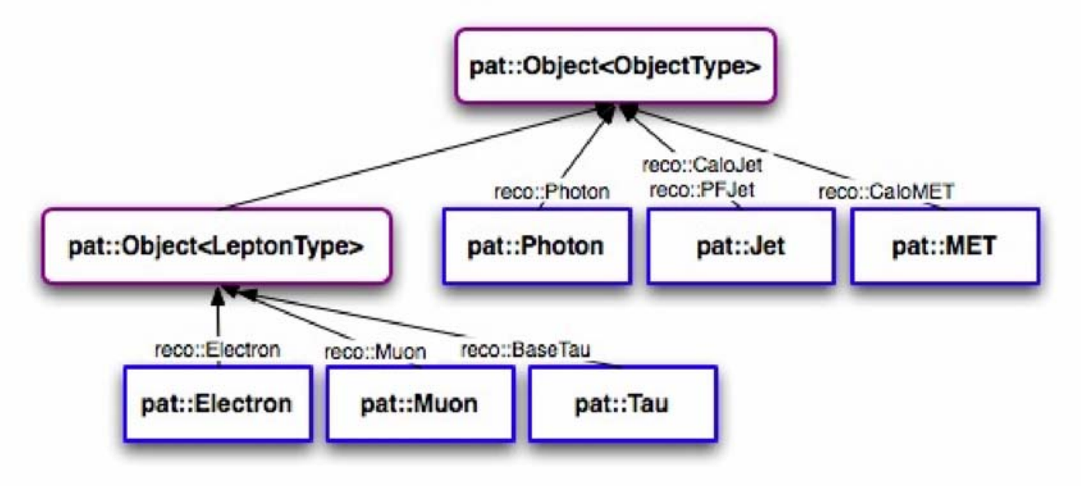

Figure 4.3: PAT framework objects

4.2.2 SUSY PAT Algorithm

SUSY PAT algorithm is configured PAT interfaces tailored to needs of SUSY analyses in CMS detector software framework [60]. The algorithm to be compiled works under any compatible CMSSW, but *CMSSW 1.6.12* version is a matter of choice being free of any possible technical error for the implementation. The algorithm contains interface classes, library of selectors, and two example codes for the hadronic SUSY searches. Installation of SUSY PAT algorithm package is remarkably simple provided that a working CMSSW environment is set up. Once installation is achieved, two subpackages are offered under SusyAnalysis working directory, namely, *AnalysisSkeleton* and *EventSelector*. These subpackages should be explained in turn.

AnalysisSkeleton includes necessary codes concerning object classes and configuration files with two ready-to-use example codes; one is for general fully hadronic channel SUSY searches, the other one is for SUSY searches with di-jet events. Further, this subpackage is used for object cross cleaning. On the other hand, EventSelector covers a wide range of event selectors which are capable of computing physics variables of interests for end users. Particularly, full decisions to events selection are provided with this subpackage for final physics analyses. Event selectors are subject to editing and removing or a new event selector can be added by users in a flexible manner. Available SUSY PAT event selector libraries and their corresponding selections are given in Appendix A.

4.2.3 Cross Cleaning

Information on physics objects (electron, muon, tau, jet, photon, and so on) are provided by different Physics Objects Groups (POGs) of CMS collaboration are not cross-checked for overlaps [61]. Overlaps of physics objects occur when they are reconstructed from the same deposit of energy found in CMS calorimeters. This can affect event counting and identification in a wrong way such that one type of physics object can appear in a collection of other type physics object. Thus, the aim of cross cleaning is to post-process against overlaps of different physics objects.

SUSY PAT algorithm provides ease-of-use cross cleaning processes as electron-jet cleaning, photon-jet cleaning, muon-jet cleaning, and electron-photon cleaning. For the analyses chapters of this thesis, both electron-jet and muon-jet cleanings are implemented. An exemplary cross cleaning procedure, which is electron-jet, should be given specifically to explore the details of implementation.

The electron-jet cleaning begins with finding an electron which appears inside a cone of a jet, that is to search for an electron and a jet which are reconstructed from the same energy deposit in the detector. Then, electron and jet overlap and both share a common energy called E_{shared}. This energy is electromagnetic energy which is deposited inside tower crystals of calorimeter and must be bigger than zero in order to perform cleaning. If electron is isolated and E_{shared} is bigger than 70 percent of jet energy, then jet is removed. If electron is isolated, but E_{shared} is smaller than 70 percent of jet energy, then E_{shared} is subtracted from energy of jet and both objects are kept. The last possibility, if electron is not isolated yet and the shared energy is above a threshold, then electron is removed and the shared energy is subtracted from energy of electron to be added to jet. See the illustration of electron-jet cleaning in Figure 4.4.

4.3 Monte Carlo Data Samples

Having discussed the analysis framework, SUSY PAT, the details of Monte Carlo samples including both signal and background data samples used in the analysis chapters of this thesis should be clarified. Further, trigger decisions which are accommodated to data sample production on Layer 1 of SUSY PAT are to be explained in this section.

Input Monte Carlo datasets of 2007 production of CMS collaboration, namely *CSA07* data samples, where it stands for Computing, Software and Analysis challenge of 2007 [62] are subject to use in this thesis. The datasets were produced with CMS software version of CMSSW 1.6.7, but used under CMSSW 1.6.12 in analysis chapters of this thesis. Both 10 pb^{-1} and 100 pb^{-1} calibration and alignment constants were used in reconstruction of CSA07 data samples. The CSA07 data consists of more than 150 million events, for that reason, only the background and signal samples which are used in this work will be explained.

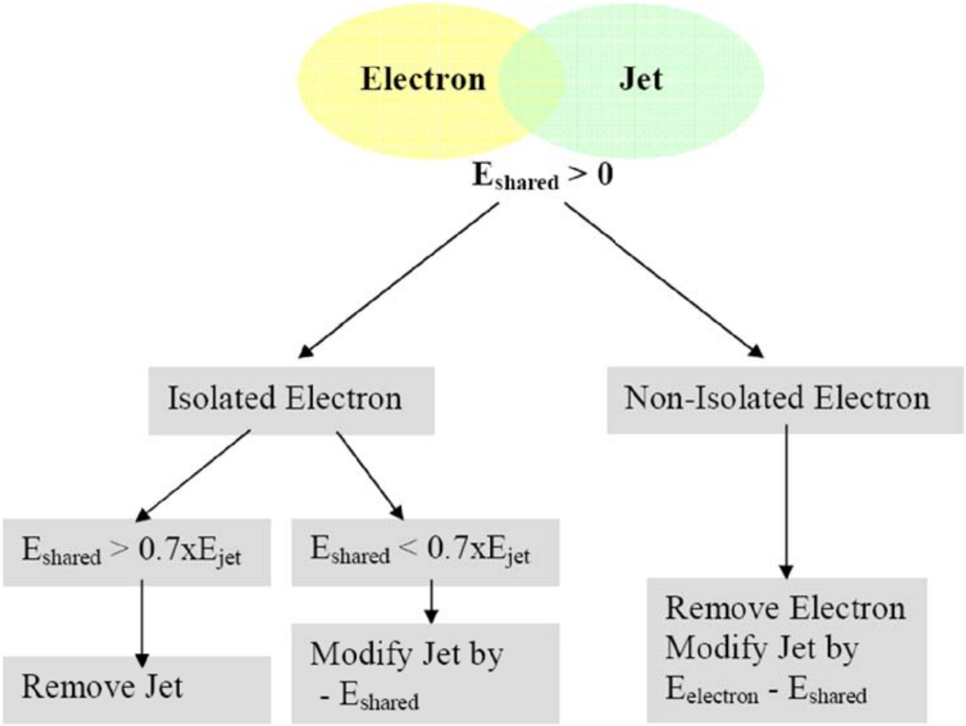

Figure 4.4: Illustration of electron-jet cleaning

Both CSA07 signal and background samples are processed on Layer 1 of SUSY related PAT, which are called Layer1 production samples or *PAT-ified* samples. Both electron-jet and muon-jet cross cleanings are applied and data samples are scaled to 1 fb^{-1} integrated luminosity, $\oint Ldt$, where L is luminosity. Appropriate physics triggers are added to the analysis path which is left to be explained in SUSY Triggers subsection.

Layer1 production of data samples which are used in this thesis for final analyses, though being in AOD data format and occupying less disk space, are stored in CMS CAF (Cern

Analysis Facility) storage elements [63]. The CMS CAF provides general services for the whole CMS collaboration including user logins, database support, production bookkeeping, and software repositories.

4.3.1 Signal Samples

Low mass mSuGra test points (benchmark points), LM1-9, are the signal data samples to be used to explore a search strategy for SUSY parameter space. Low mass SUSY signal samples are generated by Pythia [64] and cross sections are estimated by PPROSPINO1 [65] for both leading and next-to-leading orders. LM1-9 samples with their estimated cross sections in SUSY parameter space are given in Table 4.1.

Table 4.1: CSA07 Monte Carlo low mass SUSY samples.

Samples	m_0 (GeV)	$m_{1/2}$ (GeV)	$tan\beta$	A_0	$sign(\mu)$	σ(pb) LO	σ(pb) NLO
LM1	60	250	10	0	+	54.86	43.28
LM2	185	350	35	0	+	9.41	7.27
LM3	330	240	20	0	+	45.47	34.20
LM4	210	285	10	0	+	25.11	19.43
LM5	230	360	10	0	+	7.75	5.96
LM6	85	400	10	0	+	4.94	3.84
LM7	3000	230	10	0	+	6.79	3.82
LM8	500	300	10	-300	+	12.19	8.81
LM9	1450	175	50	0	+	39.79	23.28

4.3.2 Background Samples

Background samples are necessary to simulate possible contributions which come from Standard Model processes like QCD and EWK processes to SUSY signal searches. Particularly, CSA07 Layer1 productions of soups are used to simulate QCD and EWK processes which represent SM background to SUSY. Here, soups contain different processes, but, *Gumbo* contains mostly QCD processes and *Chowder* contains only EWK processes. Gumbo is generated with Pythia [64] and Chowder is generated by ALPGEN [66]. Table 4.2 summarizes the background data samples which are scaled to 1 fb^{-1} integrated luminosity with processes each soup contains [67].

Table 4.2: CSA07 Gumbo and Chowder soups.

Background Samples	Soup	Physics process	Number of Events
QCD	Gumbo	Hard QCD di-jets, photon+jets, Minimum bias events	6165643
EWK	Chowder	W+jets (up to 5 jets), Z+jets (up to 5 jets), $t\bar{t}$+jets (up to 4 jets) events	1549168

In Table 4.2, both Gumbo and Chowder soups are skimmed samples, skim refers to a filter applied peculiar to interest of a CMS collaboration group, here *JetMet* is the group which provided Gumbo and Chowder with event filters, skimmed data samples, according to needs for SUSY searches. Further, as it is a matter of preference to know number of events and also integrated luminosity values for Gumbo and Chowder instead of knowing their proper cross sections. Since, when different processes get mixed together into a big soup, they cannot all go in with their proper cross sections, we would only have QCD, so some processes are reduced with respect to others. To compensate for this reduction, a *weight* is given to each event. In analyses chapters of this thesis, this weight information is included when calculating numbers of events of a given process passing a certain selection, or when plotting a certain event variable integrated over various processes. In principle, *the event weight* is calculated by the cross section times luminosity divided by the number of events of a given process that are in the soup. When a generator level filter has been applied, skimmed, this artificially enhances the cross section, so the event weight is multiplied by the filter efficiency. In practice, for the CSA07 soups, the calculation of the event weights is non-trivial. The number of events of every process that actually make it into the soup has to be exactly known. Some processes are overlapping (e.g. Minimum Bias contains also soft QCD) and care needs to be taken to avoid double counting.

Having discussed skimmed and weighted QCD and EWK Layer1 production data samples to be used in this thesis, there is one more background to SUSY, which is invisible decay of Z boson. Here, Z boson decays into a neutrino and an anti-neutrino, which represents an irreducible background to SUSY. Invisible Z background is generated by Pythia [64] and scaled to 1 fb^{-1} integrated luminosity. To sum up, all signal and background Layer 1 production of data samples which are used in this thesis can be listed as follows:

- SUSY low mass signal samples: LM1-9 (Pythia),
- QCD extracted from Gumbo (Pythia),
- EWK $t\bar{t} + jets$,W($\rightarrow l\nu$)+jets,Z($\rightarrow ll$)+jets from Chowder (ALPGEN),
- Invisible Z ($\rightarrow \nu\bar{\nu}$) (Pythia).

4.3.3 SUSY Triggers

Having clarified Monte Carlo data samples, PAT Layer1 weighted and skimmed productions, to be used, the available CSA07 SUSY skims including specific trigger paths should be discussed. It is a matter of fact that every physics analysis should include specific physics triggers taking into account detector performance that select the event to be analyzed. CMS collaboration SUSY group has afforded available skims taking care of trigger needs of SUSY analyses [68]. The available SUSY skims are given in Appendix B.

As this thesis presents a search strategy in a fully hadronic channel with jet event topologies, then hadronic searches skims which are JetMet or JetMet-HLT should be picked up from Appendix B. And these JetMet skims offer HLT1jet and HLT2jet trigger streams to select 1 jet and 2 jet events to be studied in a fully hadronic channel.

Thus, two trigger paths are used for event selection. The first one is HLT1jet trigger path with L1 trigger level jet selection of L1-SingleJet150 (single jet L1 trigger) such that it requires one jet with transverse energy greater than 150 GeV. The second trigger path is HLT2jet trigger path with either Ll-SingleJet150 or L1-DoubletJet70 (double jet L1 trigger) such that two jets having transverse energies greater than 70 GeV each are required.

CHAPTER 5

DI-JET EVENT TOPOLOGY

5.1 Motivation

Two quarks are considered to be producing two squarks ($q\bar{q} \rightarrow \tilde{q}\bar{\tilde{q}}$) which decay into two quarks and two neutralinos, where two quarks offer two energetic jets and neutralinos imply missing energy and momentum in the detector. Squarks are thought to be pair-produced and have largest branching ratios to decay directly to neutralino which requires squark to be lighter than gluino ($m_{squark} < m_{gluino}$) such that there is no cascade decay through gluinos [69], [70]. See Figure 5.1 as an example decay chain to squark-squark production (squark pair production).

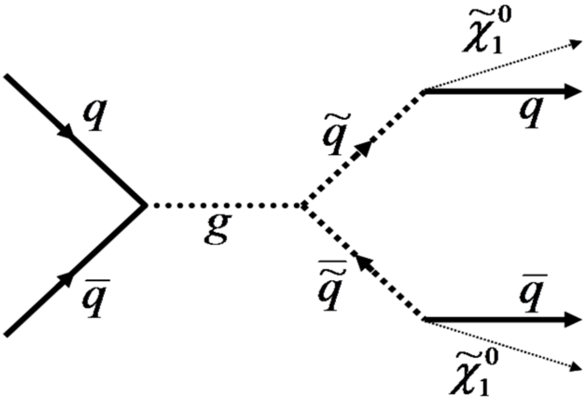

Figure 5.1: Squark-squark production as an example decay chain for SUSY di-jet event topology

5.2 Event Kinematics

The event kinematics is based on two highest energetic jets (with two highest momentum transfers associated with them). The two leading jets are reconstructed in $\eta - \phi$ space of the CMS detector that is called transverse plane (plane perpendicular to beam axis). Furthermore, two important kinematical variables are used to investigate into di-jet kinematics which are named alpha variables: α^{jj} and α_T^{jj}. The definitions of these alpha variables for di-jet case are given respectively as (see also Appendix C):

$$\alpha^{jj} = \frac{E_T^{j2}}{M_{inv}^{jj}} \tag{5.1}$$

and

$$\alpha_T^{jj} = \frac{E_T^{j2}}{M_{inv,T}^{jj}}, \tag{5.2}$$

where, E_T^{j2} is the transverse energy of the second hardest jet while M_{inv}^{jj} and $M_{inv,T}^{jj}$ are the invariant mass and the transverse invariant mass of two leading jets system which can be given as follows:

$$M_{inv}^{jj} = \sqrt{(E^{j1} + E^{j2})^2 - (\vec{p}^{j1} + \vec{p}^{j2})^2} \tag{5.3}$$

and

$$M_{inv,T}^{jj} = \sqrt{(E_T^{j1} + E_T^{j2})^2 - (\vec{p}_T^{j1} + \vec{p}_T^{j2})^2}. \tag{5.4}$$

In addition to the above mentioned alpha variables, HT^{jj} is to be used as scalar sum of transverse momentums of first and second jets and MHT^{jj} vector is to be used as negative vector sum of transverse momentums of first and second leading jets. The two kinematical variables can be formulated as follows

$$HT^{jj} = p_T^{j1} + p_T^{j2} \tag{5.5}$$

and

$$\overrightarrow{MHT}^{jj} = -(\vec{p}_T^{j1} + \vec{p}_T^{j2}). \tag{5.6}$$

The geometry of di-jet events in transverse plane is associated to the those mentioned kinematical variables with $\Delta\phi^{jj}$ giving the difference in azimuthal angles of first and second leading jets on the same transverse plane, $\Delta\phi(MHT^{jj}, j)$ giving the both differences in azimuthal angles between MHT^{jj} vector and first jet and second jet separately, and η (pseudorapidity) which is often used to locate events in longitudinal coordinate of the detector.

The last word with event kinematics is that this thesis does not invoke missing transverse energy, E_T^{miss} explicitly with alpha variable, this is because of there are other causes of missing transverse energy like jet mis-measurements this is not something one wants to encounter.

5.3 Event Selection

5.3.1 Pre-selection

The event selection begins with pre-selection. At least three reconstructed jets are pre-selected with $p_T > 20$ GeV within a cone of radius $\Delta R = 0.5$ inside η range of $|\eta| < 5$. At least one primary vertex is selected. The jets are required to be fully hadronic with $F_{em} < 0.9$. F_{em} is the electromagnetic fraction and defined as percentage of total energy of jets which is found in the electromagnetic calorimeter of the detector. Thus, hadronic jets are defined in this study as the jets leaving some energy smaller than 0.9 % of their total energy in the electromagnetic calorimeter before passing to the hadronic calorimeter. Furthermore, pre-selection includes lepton veto that is no electron, muon, and tau requested with $p_T > 10$ GeV. This pre-selection is achieved by *EventSelector* class in SUSY PAT analysis framework.

5.3.2 Datasets and Trigger

Low mass mSuGra point 1, LM1 is used as an exemplary signal sample for SUSY having the biggest cross section among other low mass points 2-9. SM Background samples are selected to be QCD events, EWK events, and additionally invisible Z decay channel events. Both SUSY signal and Standard Model (SM) background samples are simulated and scaled to 1 fb^{-1} integrated luminosity. The summary of data samples are as follows:

- SUSY LM1-9 (Pythia),
- QCD extracted from Gumbo (Pythia),
- EWK $t\bar{t} + jets$,W($\rightarrow l\nu$)+jets,Z($\rightarrow ll$)+jets from Chowder (ALPGEN),
- Invisible Z ($\rightarrow \nu\bar{\nu}$) (Pythia).

The trigger path is selected as 2 jets trigger, namely HLT2JET trigger with JetMet skim.

5.3.3 Full Selection

The full event selection which is considered for this MC analysis with di-jet events in a fully hadronic channel can be listed as below:

- Pre-selection and HLT2JET trigger path,
- Vetoing electron, muon, and tau with $p_T < 10$ GeV,
- Two leading jets with $p_T > 50$ GeV and $F_{em} < 0.9$,
- Vetoing the third jet with $p_T < 50$ GeV,
- $|\eta^{j1,j2}| < 5$,
- $HT > 500$ GeV (signal-to-background optimization).

5.4 Analysis Results

After the full selection, η^{j1} versus p_T^{j1} and η^{j2} versus p_T^{j2} distributions are considered to see transverse momentum distributions of first and second jets with respect to corresponding ηs. While SM background events including QCD, EWK, and invisible Z have wider transverse momentum distributions for the first jet, SUSY signal is observed to have narrow transverse momentum distribution along corresponding η axis as shown in Figure 5.2. For SUSY signal, transverse momentum of first jet is more centrally distributed and there occurs few events outside a region of $|\eta^{j1}| < 2.5$. For that, a cut on η of first jet is added to the cut flow due to high number of events rejection for background processes as well. On the other hand, the cut of $|\eta^{j2}| < 2.5$ is not appropriate for the second jet such that this cut will throw more SUSY events in contrast to the first case, though it still can reject higher number of events for background as shown in the Figure 5.3.

In the course of this study, an important aspect of MHT^{jj} vector was noticed which might be a thread for the di-jet system, that is, the vector was realized to be pointing in the same direction of $CaloMET$, missing energy (mostly understood in QCD di-jet events) in calorimeter that meant to have some jets that can be mis-measured within the same direction of missing energy. Since, in this study, E_T^{miss} is not taken into account explicitly and jet mis-measurements are strongly avoided, then it is required not to have jets within a cone of radius, ΔR smaller than 0.3 around the direction of missing E_T^{miss}, where E_T is taken to be harder enough like $E_T > 30$ GeV. So all the plots given from that point are obtained right after full selection with $|\eta^{j1}| < 2.5$ (as discussed before) and $\Delta\phi(MHT^{jj}, j) < 0.3$ cut, where j can be the first, the second or the third jet though the third jet is vetoed beforehand. The raw distribution of $\Delta\phi(MHT^{jj}, j)$ should be flat for both SUSY LM1 and SM background that can be seen in Figure 5.4, which is already discussed to be an insurance against jet mis-measurements. After that the resulting HT^{jj} plot appears to be as in Figure 5.5 and MHT^{jj} plot as in Figure 5.6.

The most important interpretations can be made with alpha kinematical variables that are defined before is that QCD has sharp drops around $\alpha^{jj} = 0.5$ and also around $\alpha_T^{jj} = 0.5$ and there left hardly any QCD events after $\alpha^{jj} > 0.5$ and $\alpha_T^{jj} > 0.5$, while SUSY signal, EWK, and invisible Z backgrounds still have considerable number of events, see Figures 5.7 and 5.8. Alpha cuts are very strong in terms of rejecting QCD events for signal-to-background enhancement. Thus, alphas are useful variables since certain ranges of alphas are predominantly occupied by SUSY events, but SM background (especially QCD events) is strongly diminished.

Another good approach for rejecting background events against SUSY signal is to use $\Delta\phi^{jj}$ variable. In Figure 5.9, it is clearly seen that there left nearly 2 or 3 QCD events in a region where $\Delta\phi^{jj}$ is smaller or equal to 2.0 radian while EWK, invisible Z, and SUSY signal have flat distributions of di-jet events along the azimuth. Basically, the main task is to reduce QCD events being the most dominant background to SUSY (QCD background has the largest cross section among EWK and invisible Z). Moreover, it has been already studied that most of the QCD di-jets are back-to-back [70] that means $\Delta\phi^{jj} = \pi$ (3.14 radian). For that reason, it is proposed to reject QCD background with a cut of $\Delta\phi^{jj}$ variable where it is smaller than $\frac{2\pi}{3}$ (2.1 radian).

As already been pointed out, α^{jj}, α_T^{jj}, and $\Delta\phi^{jj}$ variables can separately be used to reject QCD background to enhance SUSY signal. Besides, using these three important variables together or partially together to see whether signal can be discriminated from background processes is also inside the scope of this study. For that purpose, $\Delta\phi^{jj}$ variable versus α^{jj} plots have been studied to see whether this combination can achieve a high signal over background result or not. As it is seen in Figure 5.10 that $\Delta\phi^{jj} < \frac{2\pi}{3}$ and $\alpha^{jj} > 0.55$ cuts will be enough to dismiss all QCD events. In a similar manner, the combination of $\Delta\phi^{jj} < \frac{2\pi}{3}$ and $\alpha_T^{jj} > 0.55$ can also dismiss the all QCD events as it is seen in Figure 5.11. It is a matter of fact that α^{jj} and α_T^{jj} variables can still alone dismiss all QCD events without any restriction on $\Delta\phi^{jj}$ variable.

After all the work done for event cut flow and event variables plotting, next thing is to look at events surviving each subsequent cut for both SM background and SUSY signal on the way of signal-to-background calculation for $\alpha^{jj} > 0.55$ and $\alpha_T^{jj} > 0.55$ and $\Delta\phi^{jj} < \frac{2\pi}{3}$ cuts. As it is summarized in the Table 5.1, the final selection for this study appeared to include full selection, $|\eta^{j1}| < 2.5$, and $\Delta\phi(MHT^{jj}, j) < 0.3$. Further, $\alpha^{jj} > 0.55$, $\alpha_T^{jj} > 0.55$, and $\Delta\phi^{jj} < \frac{2\pi}{3}$ cuts applied respectively in order to see the signal yields and number of events surviving after these cuts for SM background. Following these individual cuts, $\alpha_T^{jj} > 0.55$ and $\Delta\phi^{jj} < \frac{2\pi}{3}$ cuts applied together.

Table 5.1: Number of events surviving after full selection and each subsequent cut for SUSY and SM background with corresponding signal-to-background (S/B) and significance values ($S/\sqrt{B}$) at $1fb^{-1}$ integrated luminosity.

Samples	Full sel.	$\alpha^{jj} > 0.55$	$\alpha_T^{jj} > 0.55$	$\Delta\phi^{jj} < \frac{2\pi}{3}$	$\alpha_T^{jj} > 0.55 + \Delta\phi^{jj} < \frac{2\pi}{3}$
SUSY-LM1	1725	220	425	664	418
QCD	3.0×10^6	0	0	2	0
EWK	2297	7	20	38	18
Invisible Z	232	19	56	90	55
Total Bkg.	3.0×10^6	26	76	130	73
S/B		8.5	5.6	5.1	5.7
$S/\sqrt{B}$		43.2	48.8	58.2	49

The interpretations that should be made for the signal-to-background optimizations for SUSY is that $\alpha^{jj} > 0.55$ cut gives the highest signal over background value that is this cut is all enough to suppress background. Additionally, it is also noticed that $\Delta\phi^{jj} < \frac{2\pi}{3}$ cut gives the highest signal significance value among values of other cuts applied. However, $\Delta\phi^{jj} < \frac{2\pi}{3}$ cut is not alone enough to reject all QCD events as there left still 2 events surviving. For that reason, $\alpha_T^{jj} > 0.55$ cut applied with $\Delta\phi^{jj} < \frac{2\pi}{3}$ cut and there left no QCD events surviving and S/B rose to 5.7. Thus, the final remark is to study α^{jj} variable, α_T^{jj} variable, and α_T^{jj} and $\Delta\phi^{jj}$ variables together, the first one giving the highest S/B value, the second one yields more SUSY LM1 events, and the third alternative for having considerable high S/B and significance values with a requirement rejecting all QCD events.

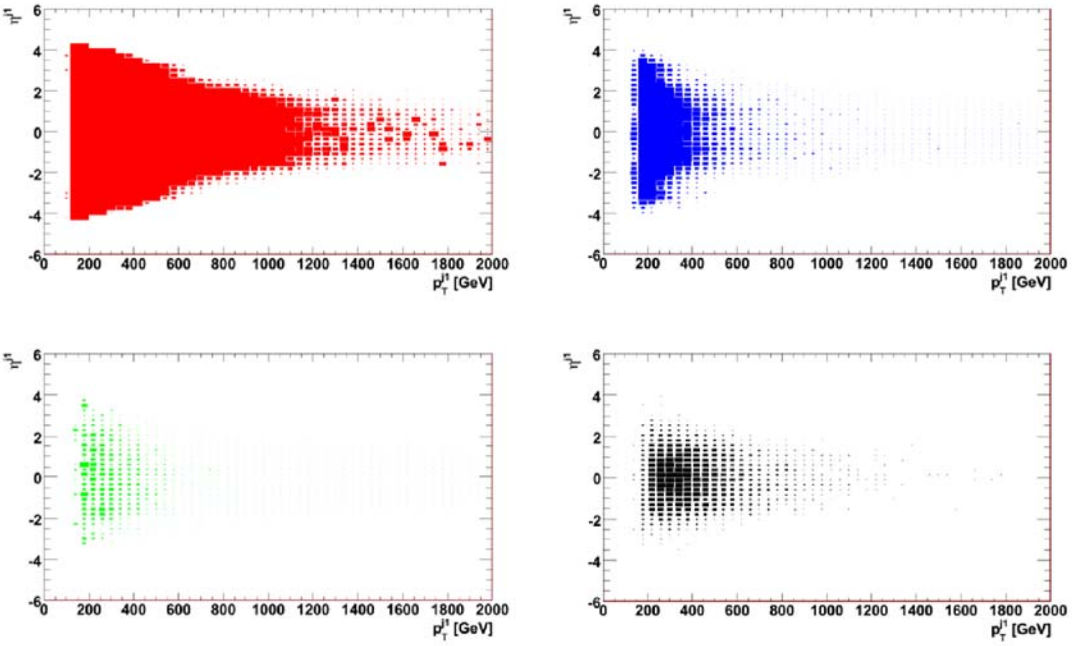

Figure 5.2: η^{j1} versus p_T^{j1} distributions for QCD (red boxes), EWK (blue boxes), invisible Z (green boxes), and LM1 (black boxes)

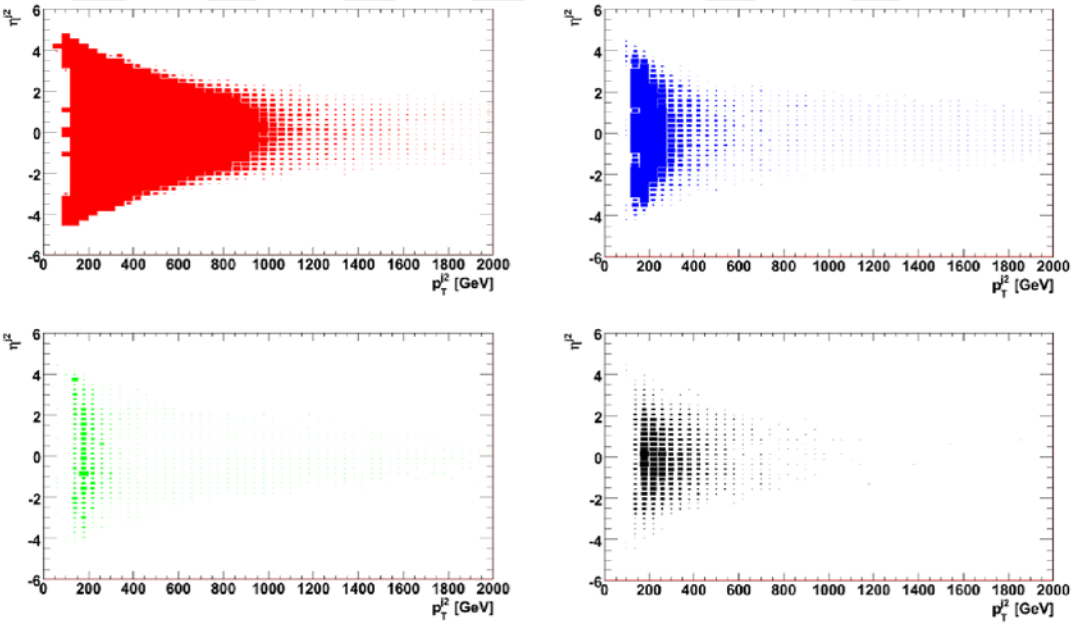

Figure 5.3: η^{j2} versus p_T^{j2} distributions for QCD (red boxes), EWK (blue boxes), invisible Z (green boxes), and LM1 (black boxes)

So far the discriminating power of alpha variables is not used for other SUSY mSuGra points: LM2-9. In Figure 5.12 and Figure 5.13, α^{jj} and α_T^{jj} distributions for LM1-9 are shown, respectively. LM1 gives the highest statistics among LM2-9 points in terms of alpha variables. Now, using the same full events selection that was shown in Table 5.1, the same alpha cuts can be applied to calculate signal-to background and significance values. Signal yields, signal-to-background ratios, and significance values for LM2-9 points are found to be not as high as those found for LM1, as can be seen in Table 5.2. Further, LM4, LM3, and LM2 points have the highest signal yields, respectively, and corresponding calculations. For LM7 signal point, there left no event after $\alpha^{jj} > 0.55$ and $\alpha_T^{jj} > 0.55$ cuts separately applied (event value smaller than 1.0 is taken 0, for example 0.2 event counted to be 0 which makes sense for a physical event).

Table 5.2: Signal yields, S/B ratios, and $S/\sqrt{B}$ values for LM2-9 signal points after $\alpha^{jj} > 0.55$ and $\alpha_T^{jj} > 0.55$ cuts separately for the same full selection which was shown in Table 5.1 (at 1 fb^{-1} integrated luminosity).

SUSY Samples	$\alpha^{jj} > 0.55$			$\alpha_T^{jj} > 0.55$		
	Yields	S/B	$S/\sqrt{B}$	Yields	S/B	$S/\sqrt{B}$
LM2	62.7	2.4	12.3	128.2	1.7	14.7
LM3	70.6	2.7	13.6	135.0	1.8	15.5
LM4	94.0	3.6	18.4	192.6	2.5	22.1
LM5	34.5	1.3	6.8	73.7	1.0	8.5
LM6	31.8	1.2	6.3	66.6	0.9	7.6
LM7	0	0	0	0	0	0
LM8	6.1	0.2	1.2	13.0	0.2	1.5
LM9	2.2	0	0.4	4.9	0	0.6

The other important interpretation is that signal yields for LM2-9 points are doubled after $\alpha_T^{jj} > 0.55$ cut as being a comparison to signal yields after $\alpha^{jj} > 0.55$ cut applied. The same result is also observed in Table 5.1, for LM1 point is that α_T^{jj} variable is more useful than α^{jj} variable when it comes to a point where one needs more signal yield. Hence, we can propose to exclude LM7 point (yielding 0 number of event after alpha and transverse alpha cuts, and accordingly having no sufficient signal-to-background and significance values) with alpha variable studies and accommodate LM4, LM3, and LM2 SUSY signal points to LM1 as being alternative signal points.

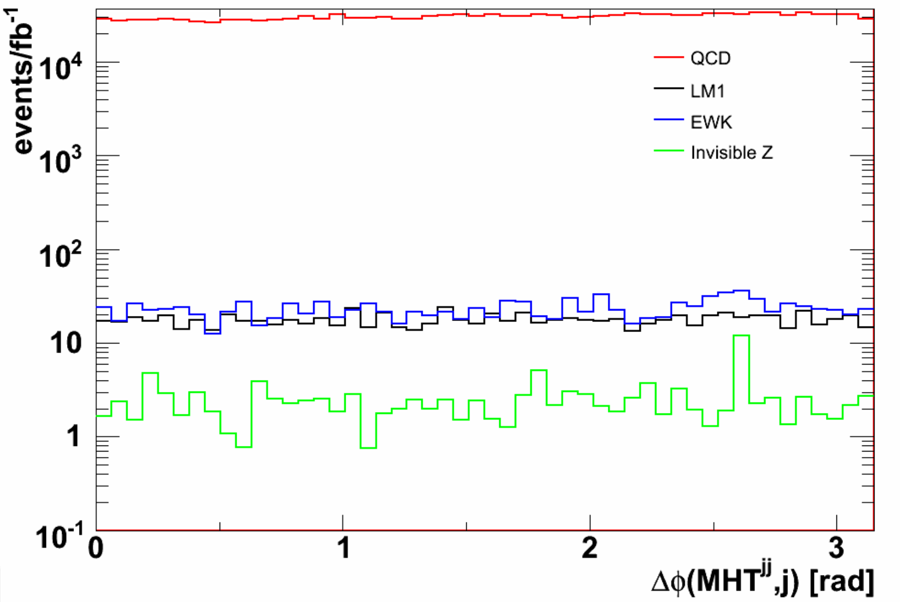

Figure 5.4: $\Delta\phi(MHT^{jj}, j)$ distributions for SM background and SUSY signal LM1

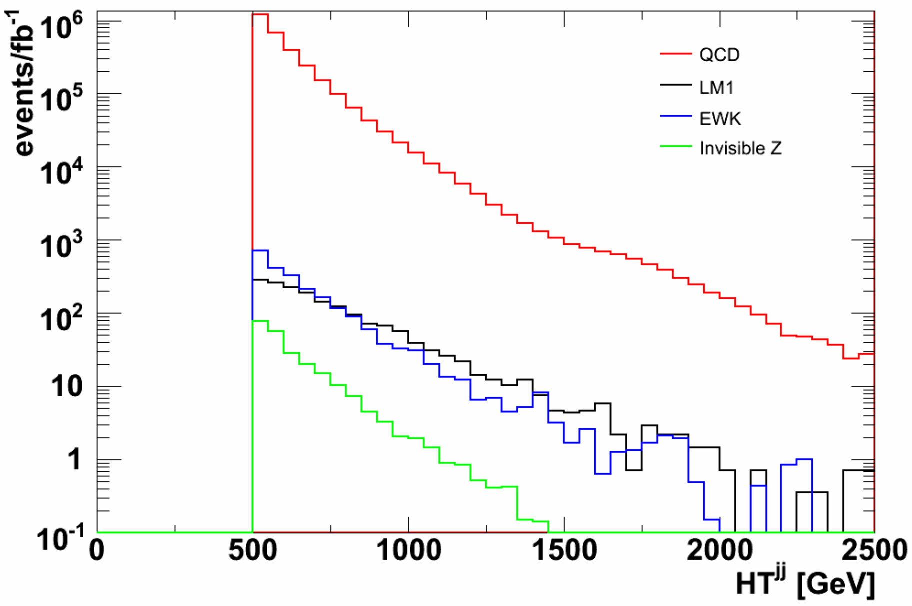

Figure 5.5: HT^{jj} distributions for SM background and SUSY signal LM1

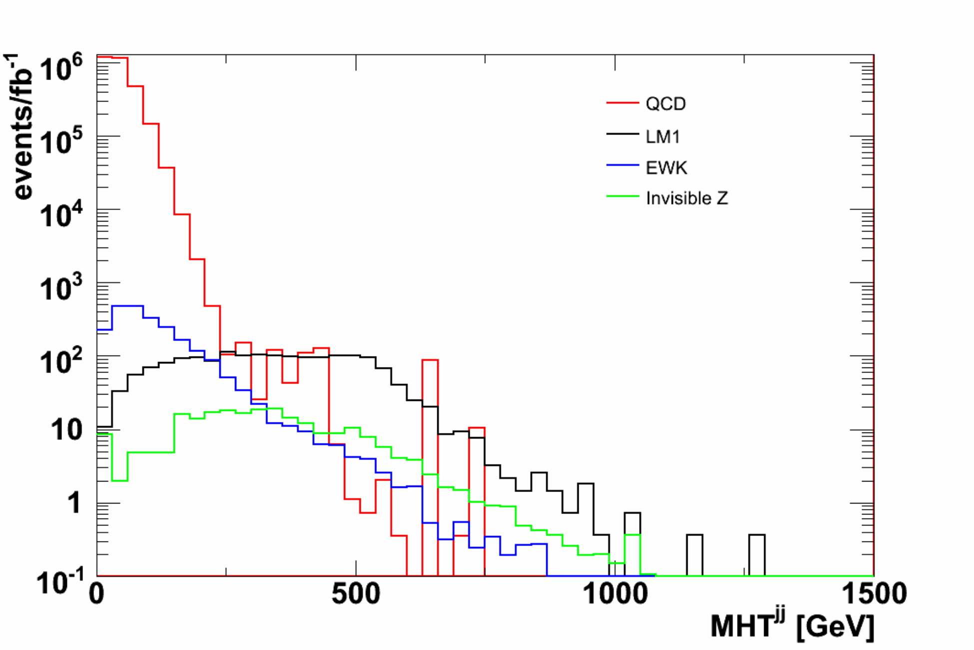

Figure 5.6: MHT^{jj} distributions for SM background and SUSY signal LM1

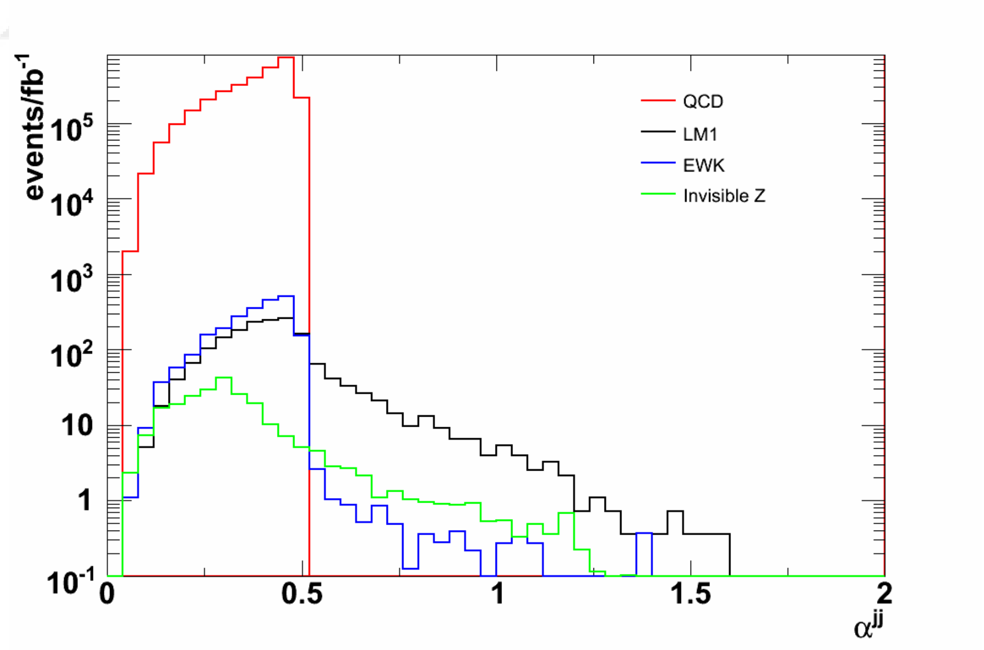

Figure 5.7: α^{jj} distributions for SM background and SUSY signal LM1

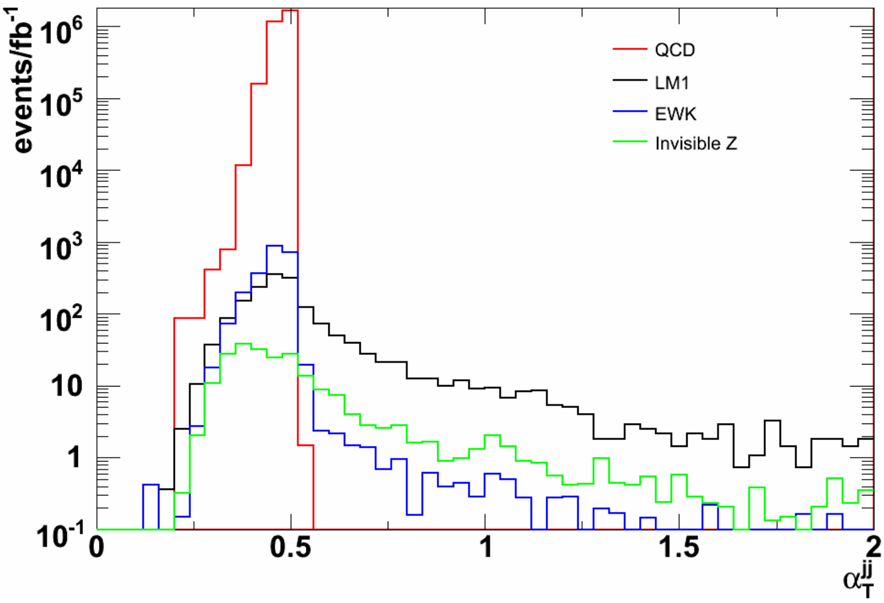

Figure 5.8: α_T^{jj} distributions for SM background and SUSY signal LM1

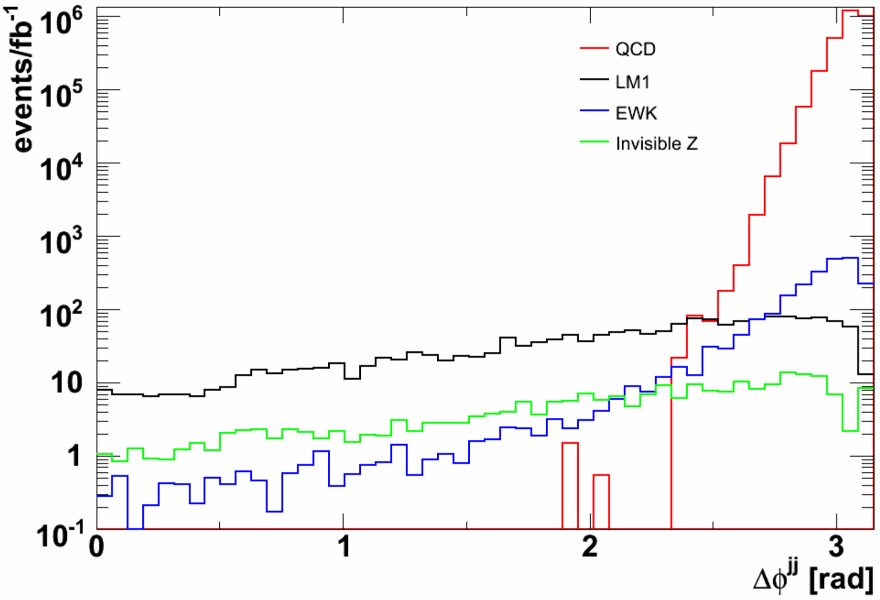

Figure 5.9: $\Delta\phi^{jj}$ variable of di-jet system for both SM background and SUSY signal LM1

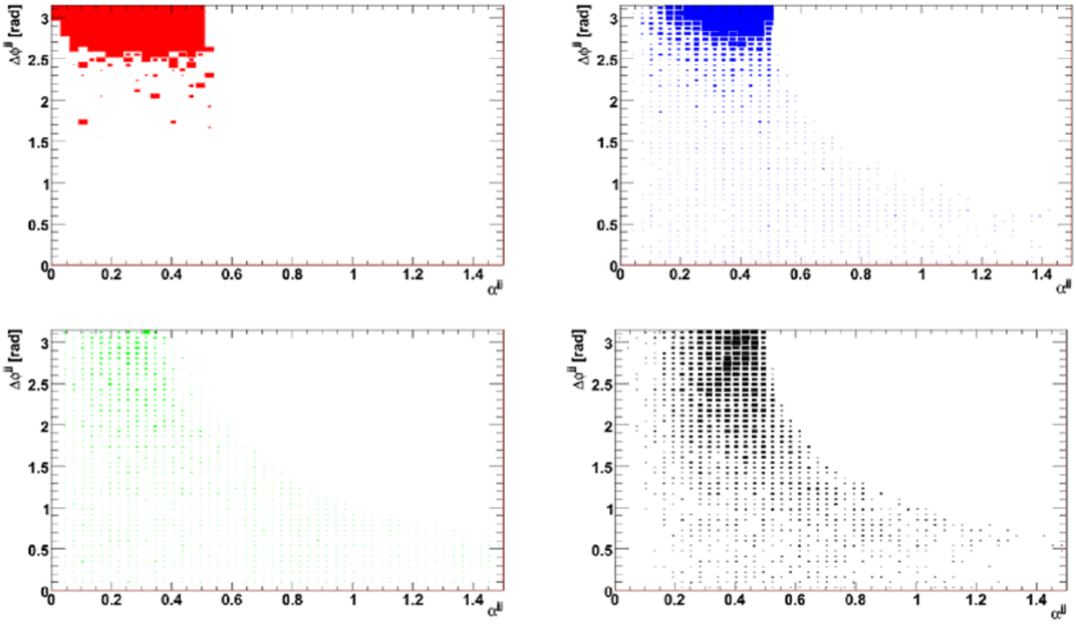

Figure 5.10: $\Delta\phi^{jj}$ versus α^{jj} distributions for QCD (red boxes), EWK (blue boxes), invisible Z (green boxes), and LM1 (black boxes)

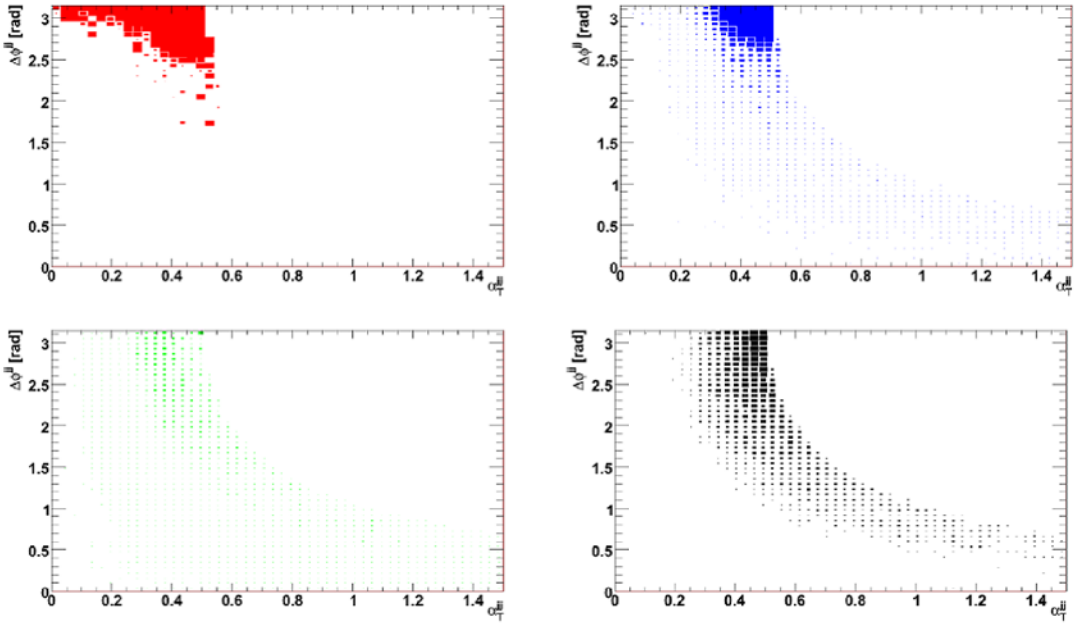

Figure 5.11: $\Delta\phi^{jj}$ versus α_T^{jj} distributions for QCD (red boxes), EWK (blue boxes), invisible Z (green boxes), and LM1 (black boxes)

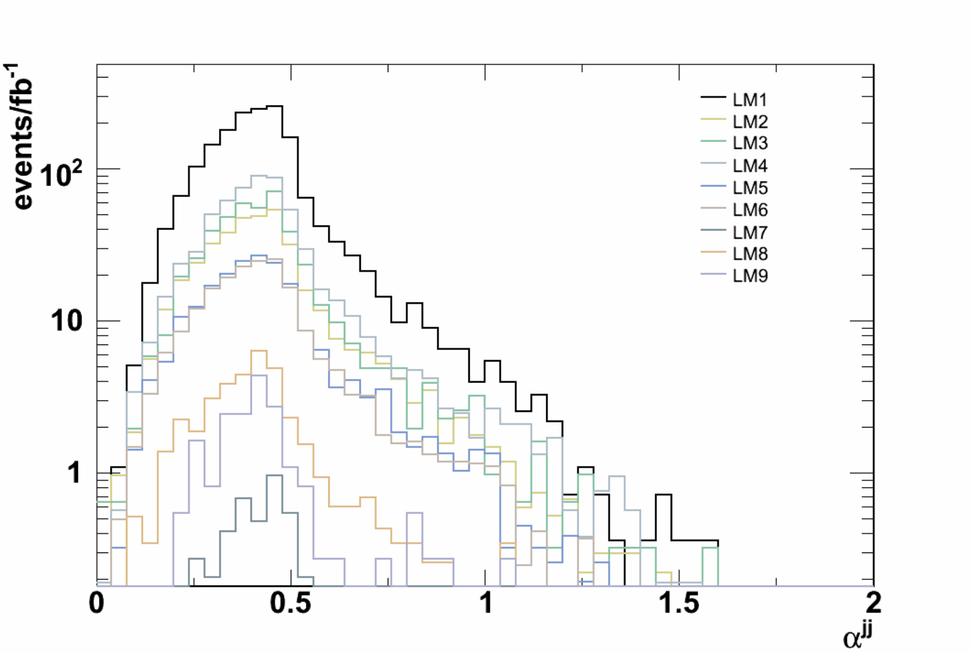

Figure 5.12: η^{j1} versus p_T^{j1} distributions for QCD (red boxes), EWK (blue boxes), invisible Z (green boxes), and LM1 (black boxes)

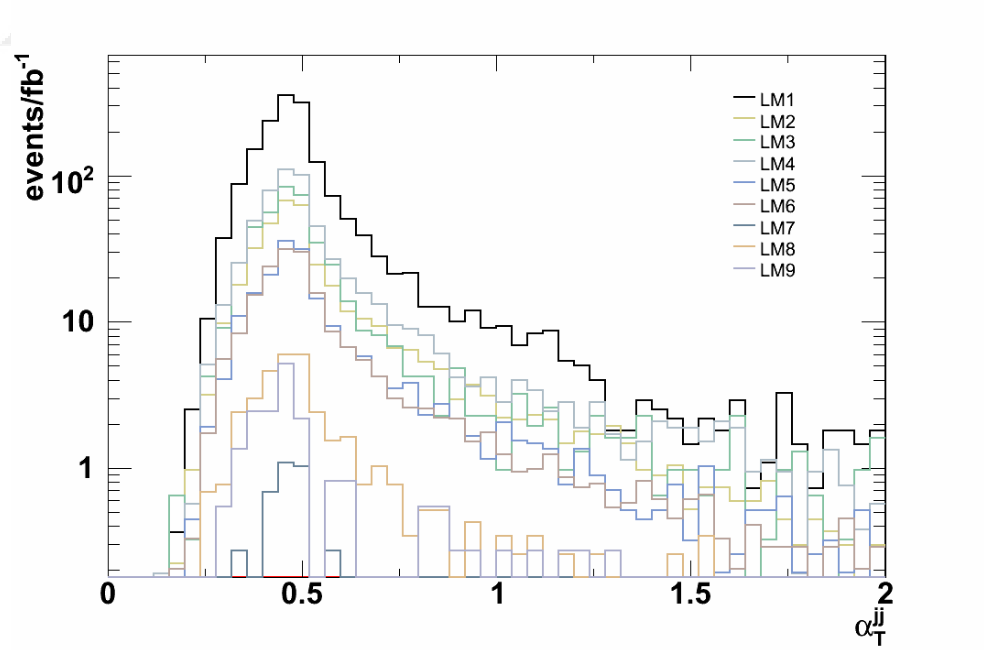

Figure 5.13: η^{j2} versus p_T^{j2} distributions for QCD (red boxes), EWK (blue boxes), invisible Z (green boxes), and LM1 (black boxes)

CHAPTER 6

EXTENSIONS TO 3-JET AND 4-JET EVENT TOPOLOGIES

6.1 3-jet Event Topology

6.1.1 Motivation

The success of SUSY di-jet study with alpha variables in terms of signal and background separation without using detector-escaping missing energy [70] inspired the extension of di-jet event topology to 3-jet event topology. By combining two of three jets into a single jet can easily reduce 3-jet decay channel to di-jet case. One decay path which would give three energetic jets is the creation of a squark and a gluino ($qg \rightarrow \tilde{q}\tilde{g}$). The gluino, being heavier than squark, decays into a quark and a squark, this squark decays into a quark and neutralino as similar to one discussed for di-jet case (Figure 6.1).

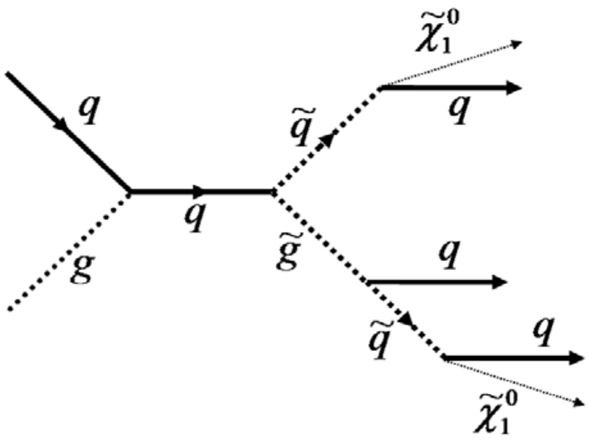

Figure 6.1: Squark-gluino production as an example decay chain for SUSY 3-jet topology

6.1.2 Event Kinematics and Selection

The event kinematics is based on three energetic jets. Three jets can be handled in a way that this topology can be investigated into similar to di-jet event topology by combining two of three jets into a single jet. Based on this requirement on event kinematics of three leading jets, we can now define new alpha variables (both normal and transverse ones) similar to ones used in Chapter 5. But in this case, different combination of jets to be reduced to a single jet should be considered. For that, there will be three normal alpha definitions and three corresponding transverse alphas with a total of six to be used and they are defined in this thesis as follows:

$$\alpha_{12}^{jjj} = \frac{min[E_T^{j3}, (E_T^{j1} + E_T^{j2})]}{M_{inv}^{jjj}}, \tag{6.1}$$

$$\alpha_{12,T}^{jjj} = \frac{min[E_T^{j3}, (E_T^{j1} + E_T^{j2})]}{M_{inv,T}^{jjj}}, \tag{6.2}$$

$$\alpha_{13}^{jjj} = \frac{min[E_T^{j2}, (E_T^{j1} + E_T^{j3})]}{M_{inv}^{jjj}}, \tag{6.3}$$

$$\alpha_{13,T}^{jjj} = \frac{min[E_T^{j2}, (E_T^{j1} + E_T^{j3})]}{M_{inv,T}^{jjj}}, \tag{6.4}$$

$$\alpha_{23}^{jjj} = \frac{min[E_T^{j1}, (E_T^{j2} + E_T^{j3})]}{M_{inv}^{jjj}}, \tag{6.5}$$

$$\alpha_{23,T}^{jjj} = \frac{min[E_T^{j1}, (E_T^{j2} + E_T^{j3})]}{M_{inv,T}^{jjj}}. \tag{6.6}$$

M_{inv}^{jjj} and $M_{inv,T}^{jjj}$ are the invariant mass and the transverse invariant mass of three leading jets system which are given as follows:

$$M_{inv}^{jjj} = \sqrt{(E^{j1} + E^{j2} + E^{j3})^2 - (\vec{p}^{j1} + \vec{p}^{j2} + \vec{p}^{j3})^2} \tag{6.7}$$

and

$$M_{inv,T}^{jjj} = \sqrt{(E_T^{j1} + E_T^{j2} + E_T^{j3})^2 - (\vec{p}_T^{j1} + \vec{p}_T^{j2} + \vec{p}_T^{j3})^2}. \tag{6.8}$$

As should be noticed that minimum combinations of transverse energies of jets are used in the numerators of alpha expressions above such that two jets could be combined into one jet and to be parallel to di-jet alpha definitions (transverse energy of second energetic jet was used in the numerators for di-jet alphas which was the smaller one). In addition to the above mentioned alpha variables, HT^{jjj} is to be used as scalar sum of transverse momentums of three leading jets and MHT^{jjj} is to be used as negative vector sum of transverse momentums of three leading jets. The two additional kinematical variables can be formulated as follows:

$$HT^{jjj} = p_T^{j1} + p_T^{j2} + p_T^{j3} \tag{6.9}$$

and

$$\overrightarrow{MHT}^{jjj} = -(\vec{p}_T^{j1} + \vec{p}_T^{j2} + \vec{p}_T^{j3}). \tag{6.10}$$

The event selection is similar to di-jet event topology including pre-selection, but this time, the third jet is allowed to pass through with $p_T^{j3} > 50$ GeV and the fourth jet is being vetoed with $p_T^{j4} < 50$ GeV. In addition, 2 jets and 1 jet high level triggers are used together, namely HLT2JET and HLT1JET triggers to select three leading jets system as being one different event selection from di-jet case. From the lesson learned from di-jet study, the first leading jet is still been considered inside a region of $|\eta^{j1}| < 2.5$ as can be treated to be signal-background optimization, and the second and third jets are considered with the requirement of $|\eta^{j2,j3}| < 5.0$. Moreover, the same data samples are used for three leading jets system study including SUSY LM1 signal sample, QCD sample from Gumbo, EWK sample from Chowder, and invisible Z sample. Thus, the full event selection can be summarized as follows:

- Pre-selection and HLT2JET and HLT1JET trigger paths,
- Vetoing electron, muon, and tau with $p_T < 10$ GeV,
- Three leading jets with $p_T > 50$ GeV and $F_{em} < 0.9$,
- Vetoing the fourth jet with $p_T < 50$ GeV,
- $|\eta^{j1}| < 2.5$,
- $|\eta^{j2,j3}| < 5.0$,
- $HT^{jjj} > 500$ GeV (signal-to-background optimization),
- $\Delta\phi(MHT^{jjj}, j) < 0.3$, where j can be any jet among three leading jets (insurance against jet mis-measurements).

6.1.3 Analysis Results of 3-jet System

Transverse momentum distributions of three leading jets and the fourth jet are given in Figure 6.2. In Figure 6.3, η distributions of three leading jets and a possible fourth jet though it is vetoed beforehand are given. SUSY LM1 point is more centrally distributed along η than SM backgrounds to SUSY. It is a matter of fact that first leading jet is more centrally scattered than second and third leading jets in the detector. Additionally, HT^{jjj} and MHT^{jjj} plots are given in Figure 6.4 and Figure 6.5 respectively. Here, $HT^{jjj} > 500$ GeV is already studied and known as signal-background optimization [27] and MHT^{jjj} distribution gives missing momentum vector for 3-jet event in the detector.

Having showed p_T and η distributions of three jets and a possible fourth jet, it is time to work on the main purpose of the analysis which is to use discriminating power of alpha variables defined for three leading jets system. For that one needs to see the distributions of alpha variables including normal and transverse ones in order to test whether these alphas can be used for signal background separation or not.

The first thing is to have a look at α_{12}^{jjj} and $\alpha_{12,T}^{jjj}$ distributions as in Figures 6.6 and 6.7 and compare them. Then, α_{12}^{jjj} is very weak in terms of separation all because of having no long tail after $\alpha_{12}^{jjj} > 0.5$ of SUSY LM1 point so as to have one difference from QCD background. Similarly, $\alpha_{12,T}^{jjj}$ can be used to divide signal and background to two separate regions, but QCD has no sharp drop around $\alpha_{12,T}^{jjj} = 0.5$ as it was in di-jet alphas.

The second couple of alphas are more powerful than that of first couple, this is because both α_{13}^{jjj} and $\alpha_{13,T}^{jjj}$ can be used to divide signal and background regions as it is shown in Figures 6.8 and 6.9.

The third couple, which is α_{23}^{jjj} and $\alpha_{23,T}^{jjj}$ seem to be the strongest one among other alphas defined, since SUSY signal has longer tail that can be studied easily for signal and background separation as shown in Figures 6.10 and 6.11.

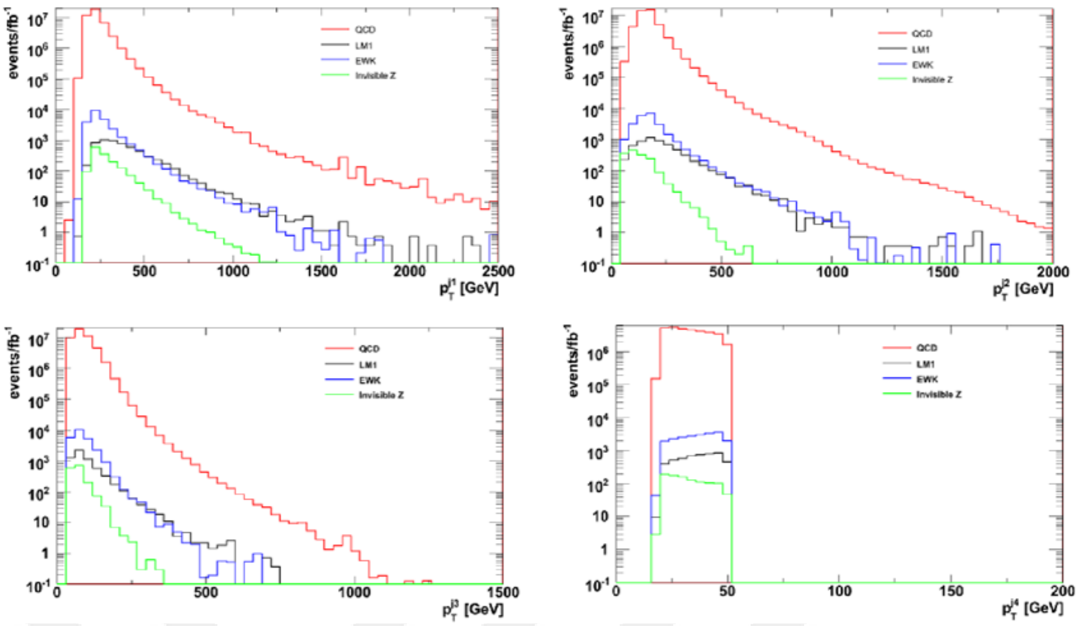

Figure 6.2: p_T distributions of three leading and a possible fourth jets

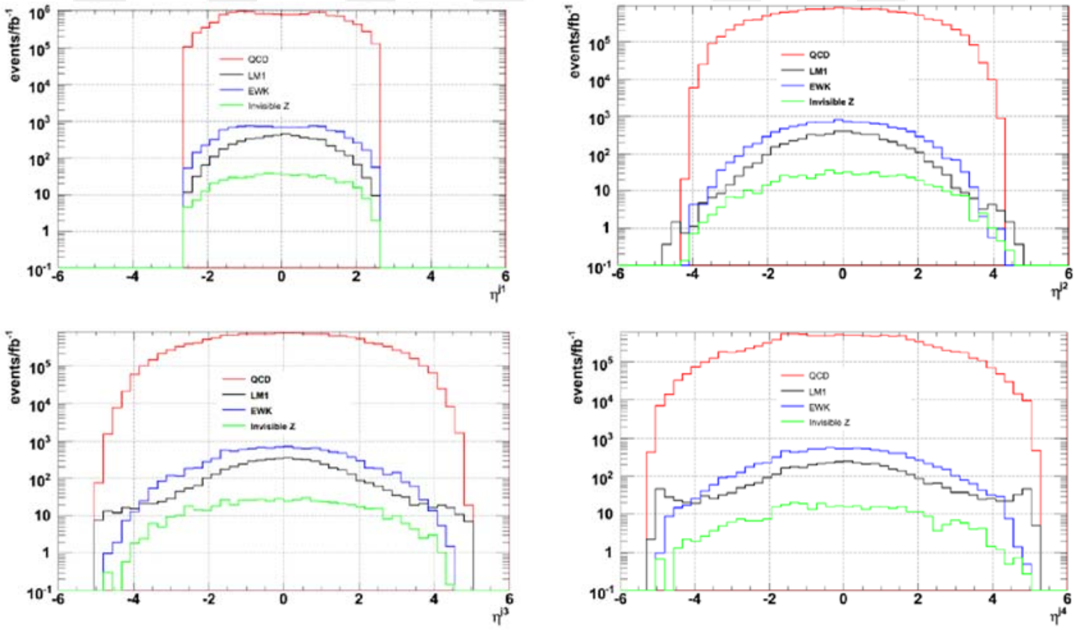

Figure 6.3: η distributions of three leading and a possible fourth jets

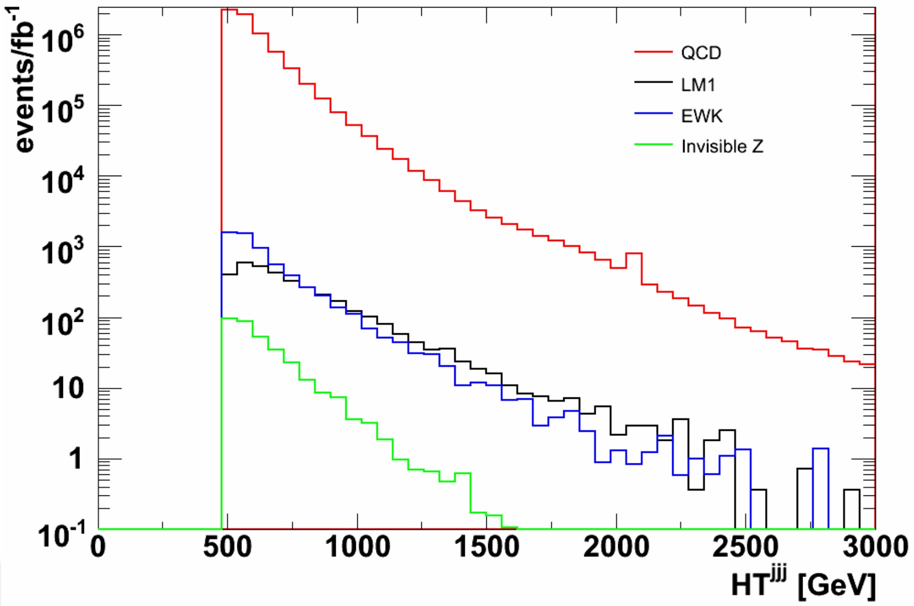

Figure 6.4: HT^{jjj} distribution for SM background and SUSY LM1 3-jet events

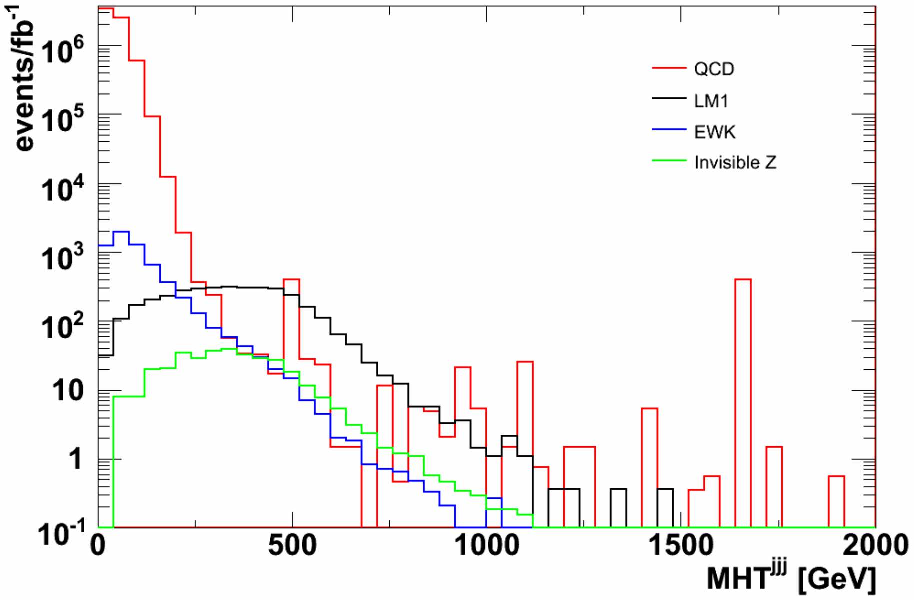

Figure 6.5: MHT^{jjj} distribution for SM background and SUSY LM1 3-jet events

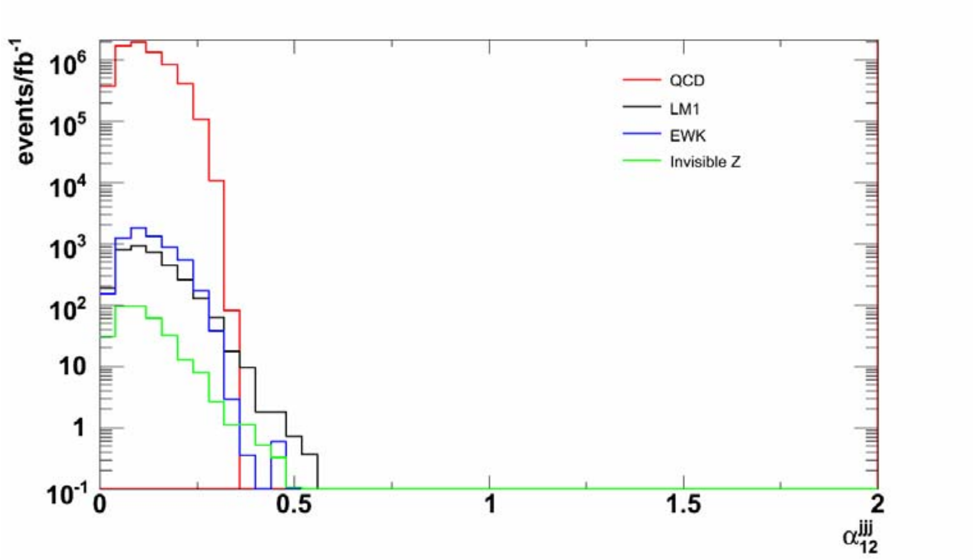

Figure 6.6: α_{12}^{jjj} distribution for SUSY LM1 and SM background

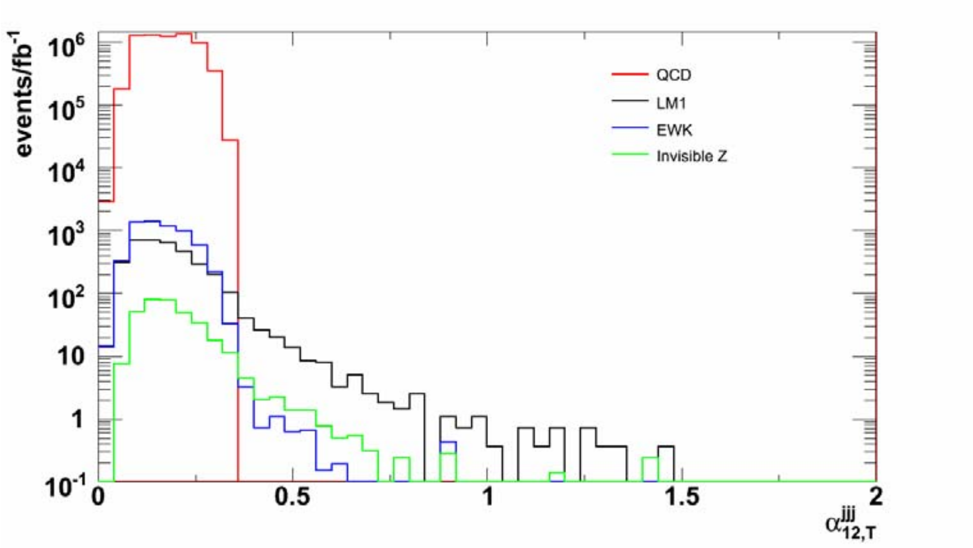

Figure 6.7: $\alpha_{12,T}^{jjj}$ distribution for SUSY LM1 and SM background

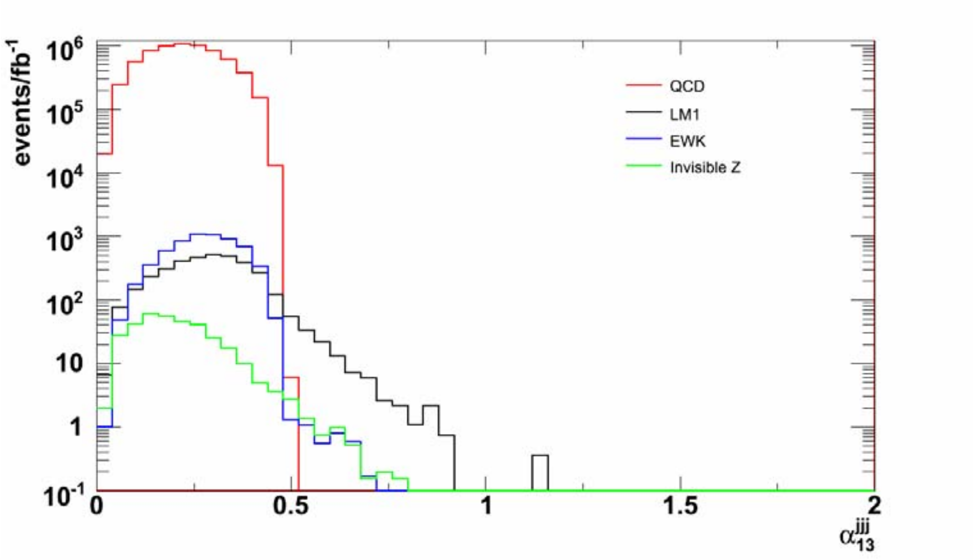

Figure 6.8: α_{13}^{jjj} distribution for SUSY LM1 and SM background

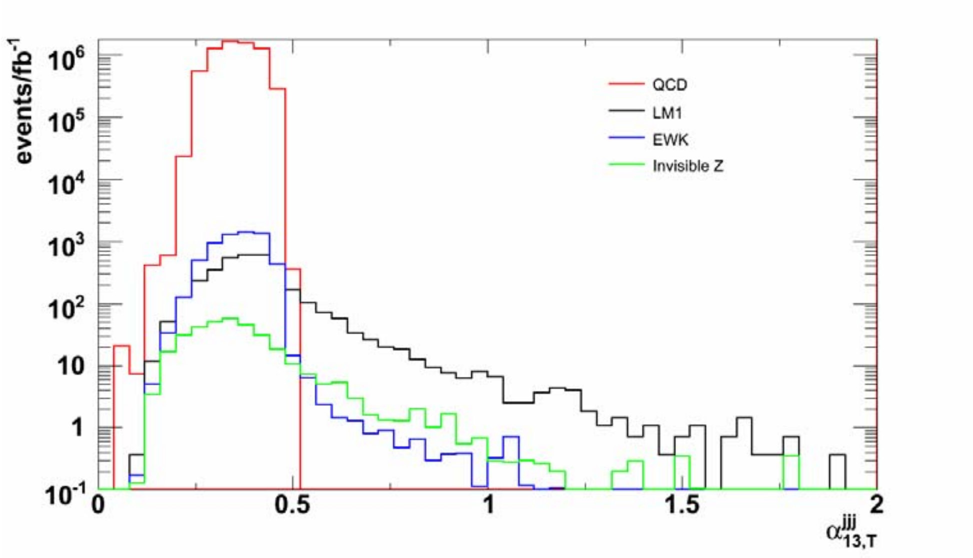

Figure 6.9: $\alpha_{13,T}^{jjj}$ distribution for SUSY LM1 and SM background

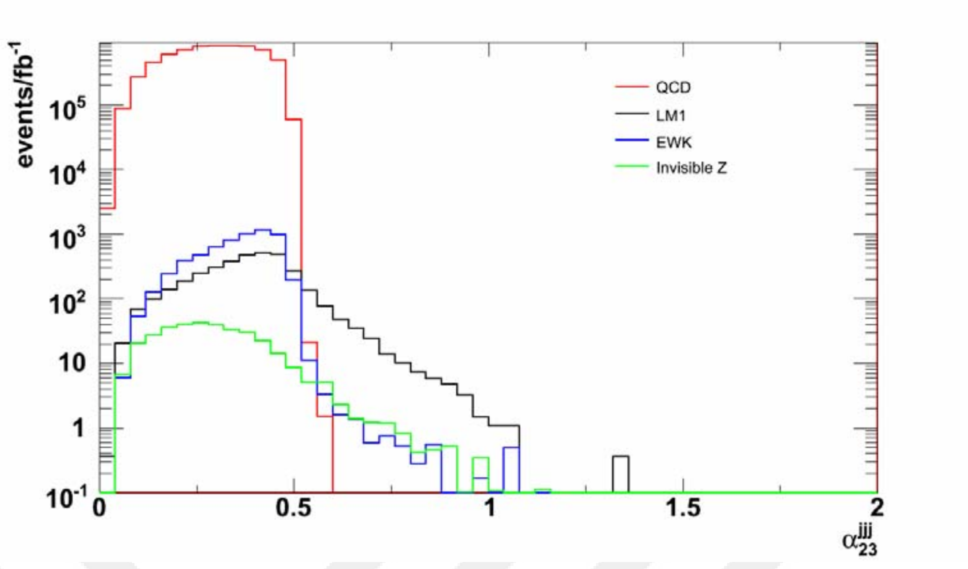

Figure 6.10: α_{23}^{jjj} distribution for SUSY LM1 and SM background

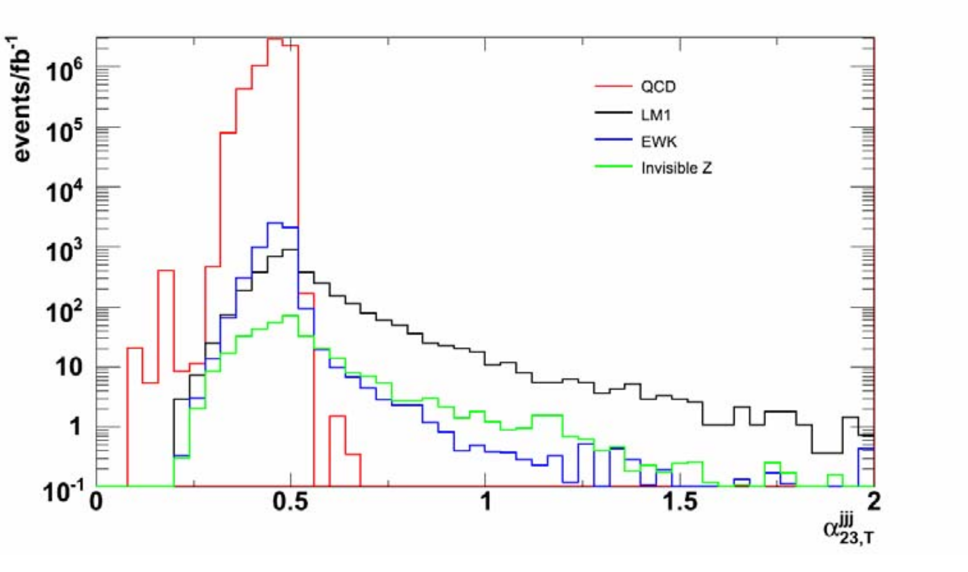

Figure 6.11: $\alpha_{23,T}^{jjj}$ distribution for SUSY LM1 and SM background

In all alpha plots, it should be noted that transverse alphas have longer SUSY signal tail than their corresponding normal alphas; this should be kept in mind at the time for signal-to-background calculation. Having clarified that α_{13}^{jjj}, $\alpha_{13,T}^{jjj}$, α_{23}^{jjj}, and $\alpha_{23,T}^{jjj}$ variables have a sharp drop at 0.5 (even if a little worsened from 0.5) for QCD and one can divide region of these alphas in two pieces as signal depleted and signal enriched regions. Thus, α_{12}^{jjj} and $\alpha_{12,T}^{jjj}$ are excluded for signal-to-background calculations in this study. It is the last thing which is worth noting that α_{13}^{jjj} and $\alpha_{13,T}^{jjj}$ can be used at 0.55 as a cut point for rejecting all QCD events, but the cut values for α_{23}^{jjj} and $\alpha_{23,T}^{jjj}$ seem to shift toward the value of 0.57 or above for leaving no QCD events surviving.

Having ruled out α_{12}^{jjj} and $\alpha_{12,T}^{jjj}$ variables by explaining that they do not have 0.5 cut off (very small cut off values than that) and do have short tails of alphas that meant less SUSY signal yield for signal-background separation, α_{13}^{jjj}, $\alpha_{13,T}^{jjj}$, α_{23}^{jjj}, and $\alpha_{23,T}^{jjj}$ values greater than 0.55 added to the cut flow in Table 6.1. As it is shown in the that $\alpha_{13}^{jjj} > 0.55$ cut yielded less SUSY signal but gave a high value of signal over background ratio. The corresponding transverse alpha, $\alpha_{13,T}^{jjj} > 0.55$ yielded more SUSY signal but less S/B. In both cases, there left zero QCD events surviving which is something good. For $\alpha_{23}^{jjj} > 0.55$ and $\alpha_{23,T}^{jjj} > 0.55$ cuts, caused high S/B ratios and significance values. However, there left 1.5 and 24 QCD events surviving, respectively, which are in contradiction with di-jet alpha cuts. For that reason, higher α_{23}^{jjj} and $\alpha_{23,T}^{jjj}$ cut values are added to the cut flow in order to reject all QCD events.

Table 6.1: Number of events surviving after full selection and each subsequent cut for SUSY and SM background with corresponding S/B and $S/\sqrt{B}$ values at $1fb^{-1}$ integrated luminosity.

Samples	Full selection	$\alpha_{13}^{jjj} > 0.55$	$\alpha_{13,T}^{jjj} > 0.55$	$\alpha_{23}^{jjj} > 0.55$	$\alpha_{23,T}^{jjj} > 0.55$
SUSY-LM1	3521	62	335	256	983
QCD	6.6×10^6	0	0	1.5	24
EWK	6059	2	12	11	66
Invisible Z	339	3	28	15	85
Total Bkg.	6.6×10^6	5	40	27.5	175
S/B		12.4	8.4	9.3	5.6
$S/\sqrt{B}$		27.7	53	48.8	74.3

In the Table 6.2, it is clearly seen that $\alpha_{23}^{jjj} > 0.60$ cut can dismiss all QCD event and produces higher S/B value than $\alpha_{23}^{jjj} > 0.55$ and $\alpha_{23}^{jjj} > 0.57$ can do, though there occurs a decrease in significance values. In addition, $\alpha_{23,T}^{jjj} > 0.65$ cut can also reject all QCD events and gives highest S/B ratio among those of $\alpha_{23}^{jjj} > 0.55$, $\alpha_{23}^{jjj} > 0.57$, and $\alpha_{23,T}^{jjj} > 0.60$ cuts. However, raising the cut off values affects number of events surviving for SUSY signal negatively for α_{23}^{jjj} > and $\alpha_{23,T}^{jjj}$ alpha values.

Putting all together, $\alpha_{23}^{jjj} > 0.60$ and $\alpha_{23,T}^{jjj} > 0.65$ cuts can only reject all QCD events and give S/B ratios of 10.3 and 7.2, respectively, which are high enough for early CMS data discovery. In both cases, significances values are very encouraging which are 40 and 59.3, respectively. Hence, it is all discussed that primary importance given to rejection of all QCD events and S/B ratio values, and secondary importance to significance values while deciding appropriate normal alpha and transverse alpha cuts.

Table 6.2: Number of events surviving after each subsequent α_{23}^{jjj} and $\alpha_{23,T}^{jjj}$ cut for SUSY and SM background with corresponding S/B and $S/\sqrt{B}$ values at $1fb^{-1}$ integrated luminosity.

Samples	$\alpha_{23}^{jjj} > 0.57$	$\alpha_{23}^{jjj} > 0.60$	$\alpha_{23,T}^{jjj} > 0.57$	$\alpha_{23,T}^{jjj} > 0.60$	$\alpha_{23,T}^{jjj} > 0.65$
SUSY-LM1	208	155	842	668	487
QCD	1.5	0	2	2	0
EWK	8.5	6	49	35	23
Invisible Z	12	9	73	60	44.5
Total Bkg.	22	15	124	97	67.5
S/B	9.5	10.3	6.8	6.9	7.2
$S/\sqrt{B}$	44.3	40	75.6	67.8	59.3

After giving cut flows of alpha variables for SM background and SUSY LM1 benchmark point, the other SUSY points can be considered with the same cuts of 3-jet alpha variables; α_{13}^{jjj}, $\alpha_{13,T}^{jjj}$, α_{23}^{jjj}, and $\alpha_{23,T}^{jjj}$ as shown in Figures 6.12, 6.13, 6.14, and 6.15 for comparison. The first thing is to have a look at signal yields of LM2-9 points for alpha cuts. In the Tables 6.3 and 6.4, LM2, LM3, and LM4 have the highest SUSY signal events among LM2-LM9 points after alpha cuts. For both signal over background and significance values, LM2, LM3, and LM4 have highest values even if that values are smaller than those of SUSY LM1 point. As it was found in di-jet study, LM7 can be excluded being very poor in terms of signal over background enhancement with alpha variables.

Hence, the success of alpha variables is not repetitive for LM2-9 SUSY points, but LM2, LM3, and LM4 can be alternatively used with SUSY LM1 point for comparison.

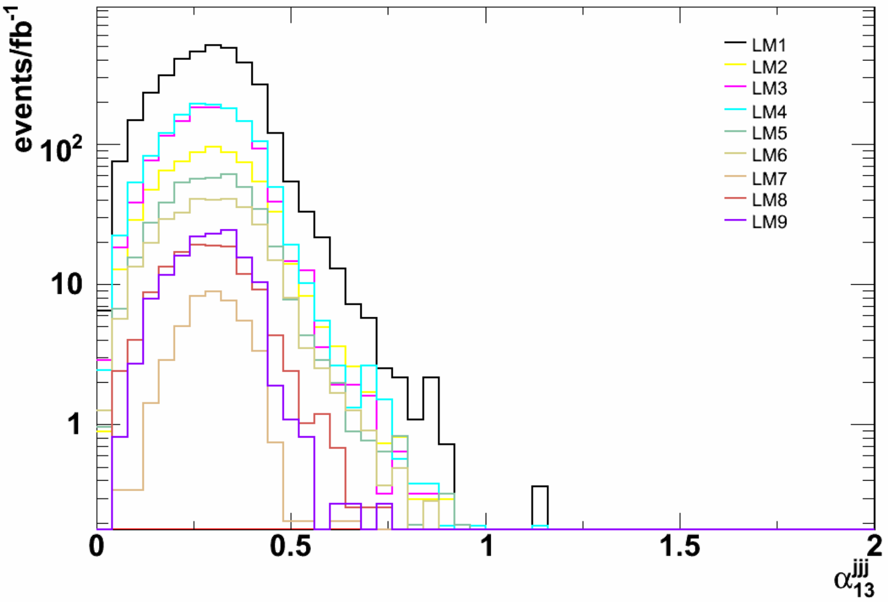

Figure 6.12: α_{13}^{jjj} distribution for SUSY LM1-9 points

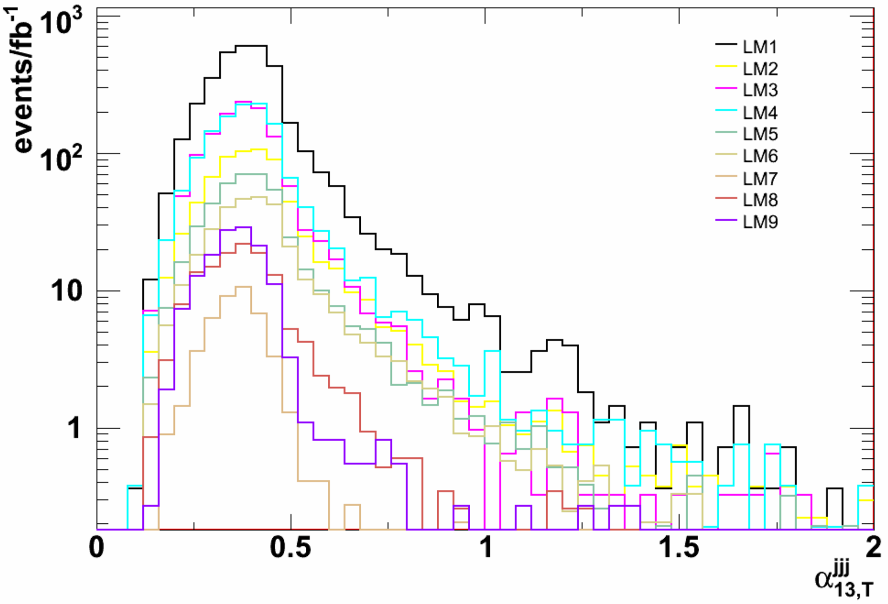

Figure 6.13: $\alpha_{13,T}^{jjj}$ distribution for SUSY LM1-9 points

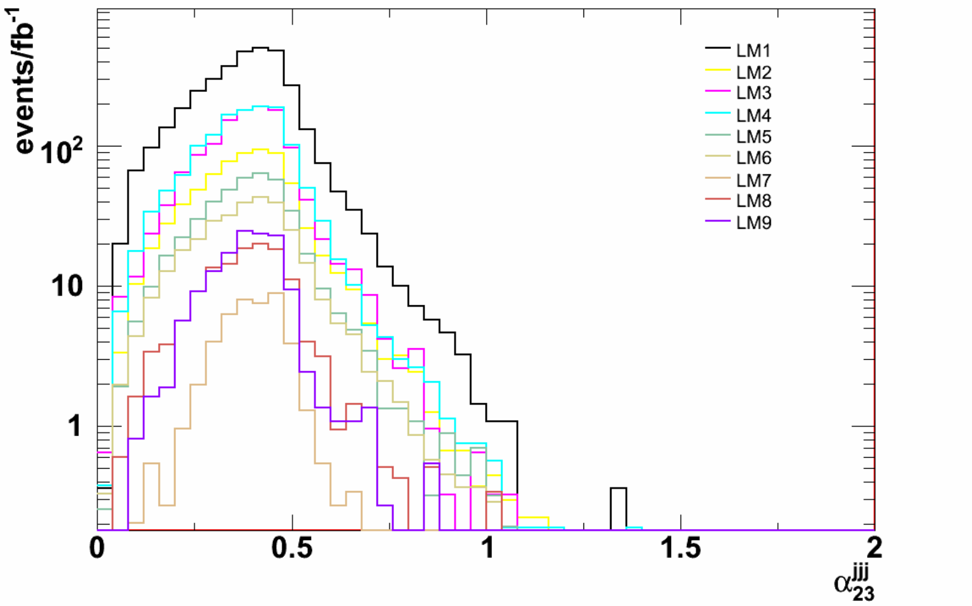

Figure 6.14: α_{23}^{jjj} distribution for SUSY LM1-9 points

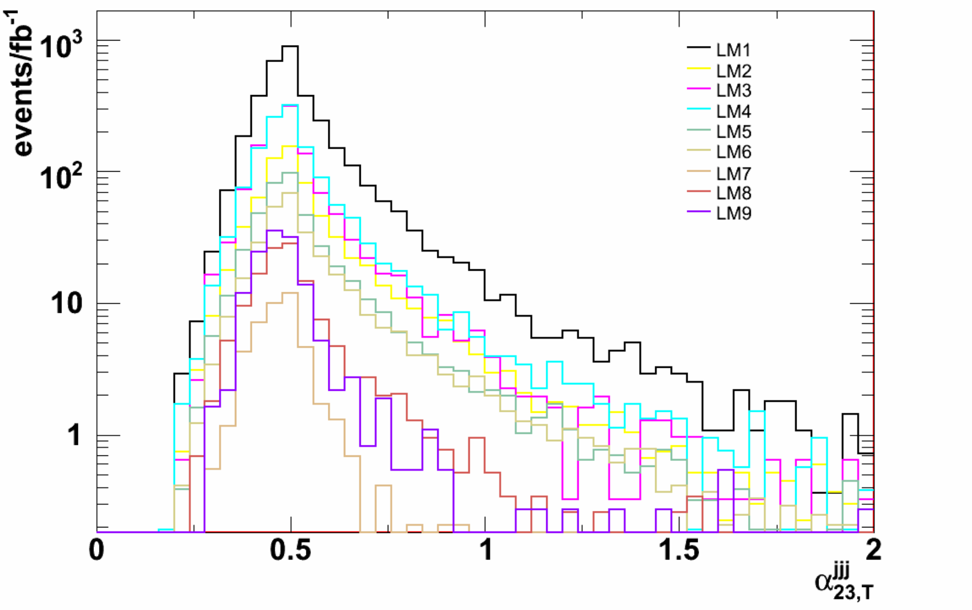

Figure 6.15: $\alpha_{23,T}^{jjj}$ distribution for SUSY LM1-9 points

Table 6.3: Signal yields, S/B ratios, and $S/\sqrt{B}$ values for LM2-9 signal points after $\alpha_{13}^{jjj} > 0.55$ and $\alpha_{13,T}^{jj} > 0.55$ cuts applied separately for (at 1 fb^{-1} integrated luminosity).

SUSY Samples	$\alpha_{13}^{jjj} > 0.55$			$\alpha_{13,T}^{jjj} > 0.55$		
	Yields	S/B	$S/\sqrt{B}$	Yields	S/B	$S/\sqrt{B}$
LM2	18	3.6	8	90	2.3	14.2
LM3	14	2.8	6.3	96	2.4	15.2
LM4	18	3.6	8	133	3.3	21
LM5	10	2	4.5	53	1.3	8.4
LM6	9	1.8	4	48	1.2	7.6
LM7	1	0.2	0.5	2	0	0.3
LM8	3	0.6	1.5	13	0.3	2
LM9	1	0.2	0.5	6	0	1

Table 6.4: Signal yields, S/B ratios, and $S/\sqrt{B}$ values for LM2-9 signal points after $\alpha_{23}^{jjj} > 0.60$ and $\alpha_{23,T}^{jj} > 0.65$ cuts applied separately for (at 1 fb^{-1} integrated luminosity).

SUSY Samples	$\alpha_{23}^{jjj} > 0.60$			$\alpha_{23,T}^{jjj} > 0.65$		
	Yields	S/B	$S/\sqrt{B}$	Yields	S/B	$S/\sqrt{B}$
LM2	40	2.7	10.3	122	1.8	15
LM3	49	3.3	12.6	138	2	17
LM4	47	3.1	12.1	186	2.7	23
LM5	21	1.4	5.4	72	1.1	9
LM6	19	1.3	4.9	62	1	7.5
LM7	1	0	0.3	3	0	0.4
LM8	6	0.4	1.6	17	0.2	2.1
LM9	4	0.3	1	10	0	1.2

6.2 4-jet Event Topology

6.2.1 Motivation

The success of 3-jet event decay channel with alpha variables in terms of signal and background separation without using detector-escaping missing energy [70] motivated the extension of di-jet case to 4-jet event topology. By combining each two jets of four jets into a single jet can easily reduce 4-jet decay channel to di-jet case, but with new modifications to alpha variables and directly to 4-jet event kinematics required. Further, the decay path which would offer four energetic jets is the creation of two gluinos ($q\bar{q} \to \tilde{g}\tilde{g}$). Each gluino, being heavier than a squark, decays into a quark and a squark, this squark decays into a quark and a neutralino. Totally, there yields four quarks and two neutralinos (imply missing energy). An example diagram to gluino-gluino production which dominates in 4-jet plus missing energy channel is shown in Figure 6.16.

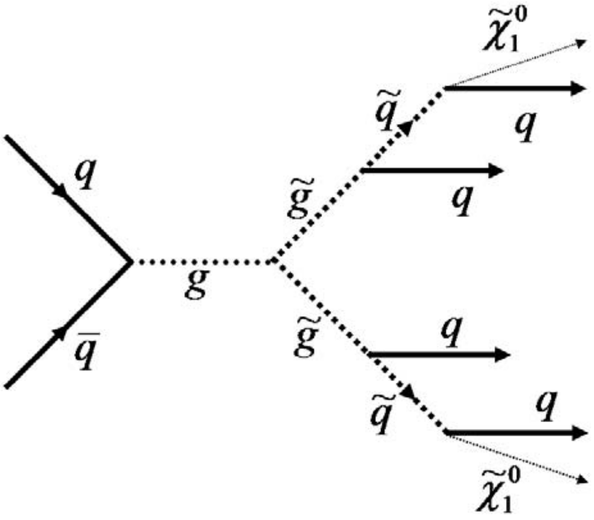

Figure 6.16: Gluino-gluino production as an example decay chain for SUSY 4-jet event topology

6.2.2 Event Kinematics and Selection

The event kinematics includes four leading jets as being a signature to SUSY in which the combinations of two of four jets into a single jet to reduce event kinematics to di-jet case considered. In particular, different combinations of jets are taken into account for the alpha kinematical variables. For that, there will be three normal alpha definitions and three corresponding transverse alphas with a total of six to be used and they are defined in this study as follows:

$$\alpha_{12}^{jjjj} = \frac{min[(E_T^{j1} + E_T^{j2}), (E_T^{j3} + E_T^{j4})]}{M_{inv}^{jjjj}}, \tag{6.11}$$

$$\alpha_{12,T}^{jjjj} = \frac{min[(E_T^{j1} + E_T^{j2}), (E_T^{j3} + E_T^{j4})]}{M_{inv,T}^{jjjj}}, \tag{6.12}$$

$$\alpha_{13}^{jjjj} = \frac{min[(E_T^{j1} + E_T^{j3}), (E_T^{j2} + E_T^{j4})]}{M_{inv}^{jjjj}}, \tag{6.13}$$

$$\alpha_{13,T}^{jjjj} = \frac{min[(E_T^{j1} + E_T^{j3}), (E_T^{j2} + E_T^{j4})]}{M_{inv,T}^{jjjj}}, \tag{6.14}$$

$$\alpha_{14}^{jjjj} = \frac{min[(E_T^{j1} + E_T^{j4}), (E_T^{j2} + E_T^{j3})]}{M_{inv}^{jjjj}}, \tag{6.15}$$

$$\alpha_{14,T}^{jjjj} = \frac{min[(E_T^{j1} + E_T^{j4}), (E_T^{j2} + E_T^{j3})]}{M_{inv,T}^{jjjj}}, \tag{6.16}$$

and where M_{inv}^{jjjj} and $M_{inv,T}^{jjjj}$ are the invariant mass and the transverse invariant mass of four leading jets system which are given as:

$$M_{inv}^{jjjj} = \sqrt{(E^{j1} + E^{j2} + E^{j3} + E^{j4})^2 - (\vec{p}^{j1} + \vec{p}^{j2} + \vec{p}^{j3} + \vec{p}^{j4})^2} \tag{6.17}$$

and

$$M_{inv,T}^{jjjj} = \sqrt{(E^{j1} + E^{j2} + E^{j3} + E^{j4})^2 - (\vec{p}_T^{j1} + \vec{p}_T^{j2} + \vec{p}_T^{j3} + \vec{p}_T^{j4})^2}. \tag{6.18}$$

As should be clarified that alpha variables are defined in a way as to consider each two jets are added in different combinations (permutations) in the numerators. For instance, α_{12}^{jjjj} is calculated as taking minimum value of transverse energy sum among the summations of first jet E_T and second jet E_T or third jet E_T and fourth jet E_T. In addition to the above mentioned alpha variables, HT^{jjjj} is to be used as scalar sum of transverse momentums of four leading jets and MHT^{jjjj} is to be used as negative vectorial sum of transverse momentums of four leading jets as being parallel to their uses in di-jet and 3-jet event topologies. The two additional kinematical variables can be formulated as follows:

$$HT^{jjjj} = p_T^{j1} + p_T^{j2} + p_T^{j3} + p_T^{j4} \tag{6.19}$$

and

$$\overrightarrow{MHT}^{jjjj} = -(\vec{p}_T^{j1} + \vec{p}_T^{j2} + \vec{p}_T^{j3} + \vec{p}_T^{j4}). \tag{6.20}$$

The event selection is similar to 3-jet event topology including pre-selection, but this time, the fourth jet is being allowed to pass through with $p_T^{j4} > 50$ GeV and the fifth jet is being vetoed with $p_T^{j5} < 50$ GeV. In addition, the same data samples are used for three leading jets system study including SUSY LM1 signal sample, QCD sample from Gumbo, EWK sample from Chowder, and invisible Z sample. Thus, keeping the same event selection of di-jet and 3-jet analyses, the full event selection can be summarized for 4-jet decay path as follows:

- Pre-selection and HLT2JET and HLT1JET trigger paths,
- Vetoing electron, muon, and tau with $p_T < 10$ GeV,
- Four leading jets with $p_T > 50$ GeV and $F_{em} < 0.9$,
- Vetoing the fifth jet with $p_T < 50$ GeV,
- $|\eta^{j1}| < 2.5$,
- $|\eta^{j2,j3,j4}| < 5.0$,
- $HT^{jjjj} > 500$ GeV (signal-to-background optimization),
- $\Delta\phi(MHT^{jjjj}, j) < 0.3$, where j can be any jet among three leading jets (insurance against jet mis-measurements).

6.2.3 Analysis Results of 4-jet System

Transverse momentum distribution of the fourth leading jet is given in Figure 6.17 with a lower range than those of the first, second, and third leading jets as expected. In Figure 6.18, η distribution of the fourth jet is given for SUSY signal LM1 and SM background with an interpretation that fourth jet can be found in a non-central region along longitudinal coordinate for SUSY signal point. Additionally, HT^{jjjj} and MHT^{jjjj} plots are given in Figure 6.19 and Figure 6.20 respectively. Here, $HT^{jjjj} > 500$ GeV is already studied and known as signal-background optimization and MHT^{jjjj} distribution gives missing momentum vector for 4-jet event in the detector.

Alpha variables have already been defined for 4-jet case, and three couples of alpha including both normal and transverse ones are being used to discriminate signal from background events. The first couple, which are α_{12}^{jjjj} and $\alpha_{12,T}^{jjjj}$ variables shown in Figures 6.21 and 6.22, respectively. Though these alphas have sharp edge of QCD events dropping around 0.5, there yields less SUSY signal after $\alpha_{12}^{jjjj} > 0.55$ and $\alpha_{12,T}^{jjjj} > 0.55$ cut off points, and the first couple of alphas is excluded in this study for signal over background calculations.

The second couple of alphas, which is α_{13}^{jjjj} and $\alpha_{13,T}^{jjjj}$ variables have higher signal events surviving as contrast to the first couple of alphas after $\alpha_{13}^{jjjj} > 0.55$ and $\alpha_{13,T}^{jjjj} > 0.55$ cut off points, as seen in Figures 6.23 and 6.24, respectively. The negative aspect of this couple comes with $\alpha_{13,T}^{jjjj}$ variable that is there survives some QCD events after $\alpha_{13,T}^{jjjj} > 0.55$ cut off point, which is also observed with transverse alphas of 3-jet event topology.

The last couple of alphas, which is α_{14}^{jjjj} and $\alpha_{14,T}^{jjjj}$ variables (Figures 6.25 and 6.26), which are also being used in this study such that SUSY signal has long tail after 0.55 that can be used to study signal-background separation. Having added α_{13}^{jjjj} , $\alpha_{13,T}^{jjjj}$, α_{14}^{jjjj}, and $\alpha_{14,T}^{jjjj}$ variables to the signal-background separation use list, one important thing is to state that transverse alphas are getting worsened after 0.55 cut point for 4-jet case, as also observed in 3-jet alpha study should not be a problem such that after the cut of 0.55 there will survive a small number of QCD events which affects S/B ratios much less.

Having deciding on which alphas are at first glance are useful to take into account, as similar to di-jet and 3-jet studies, S/B and significance values after these alpha cuts are presented in Table 6.5. The first thing is to notice that $\alpha_{13}^{jjjj} > 0.55$ and $\alpha_{14}^{jjjj} > 0.55$ cuts yielded a small number of SUSY LM1 events and indeed one can want to obtain a better result in terms of SUSY yielding number of events. However, signal over background and significance values are still high enough to be promising for early discovery. In addition, cuts applied on transverse alphas, $\alpha_{13,T}^{jjjj} > 0.55$ and $\alpha_{14,T}^{jjjj} > 0.55$, left high number of SUSY events surviving and produced high S/B and significance values. As opposed to normal alpha cuts, transverse alpha cuts are not able to reject all QCD events such that there left 0.5 QCD event after $\alpha_{13,T}^{jjjj} > 0.55$ cut that can be taken 0 and there left 2.5 QCD events after $\alpha_{14,T}^{jjjj} > 0.55$ cut.

Table 6.5: Number of events after full selection and 4-jet alpha cuts for SUSY and SM background with corresponding S/B and $S/\sqrt{B}$ values at $1 fb^{-1}$ integrated luminosity.

Samples	Full selection	$\alpha_{13}^{jjjj} > 0.55$	$\alpha_{13,T}^{jjjj} > 0.55$	$\alpha_{14}^{jjjj} > 0.55$	$\alpha_{14,T}^{jjjj} > 0.55$
SUSY-LM1	3007	26	316	62	572
QCD	4.6×10^{6}	0	0.5	0	2.5
EWK	8550	1	17	3	42
Invisible Z	144	1.5	15	3	26
Total Bkg.	4.6×10^{6}	2.5	32.5	6	70.5
S/B		10.4	9.7	10.3	8.1
$S/\sqrt{B}$		16.4	55.4	25.3	68.1

As it was done in di-jet and 3-jet analyses, numbers of events surviving alpha cuts for SUSY LM2-9 points are given in the Table 6.6. It is clearly seen that LM2-9 points have less number of events surviving after alpha cuts as compared to that of LM1 point. Moreover, only $\alpha_{14,T}^{jjjj} >$ 0.55 cut yields high number of events that can be taken into account with LM2, LM3, and LM4 while performing S/B calculations. For LM2-9 points, α_{13}^{jjjj} and $\alpha_{13,T}^{jjjj}$ distributions are given in Figures 6.27 and 6.28 while α_{14}^{jjjj} and $\alpha_{14,T}^{jjjj}$ distributions are presented in Figures 6.29 and 6.30.

Table 6.6: Signal yields for LM2-9 points after $\alpha_{13}^{jjjj} > 0.55$, $\alpha_{13,T}^{jjjj} > 0.55$, $\alpha_{14}^{jjjj} > 0.55$, and $\alpha_{14,T}^{jjjj} > 0.55$ cuts applied separately at 1 fb^{-1} integrated luminosity.

Samples	$\alpha_{13}^{jjjj} > 0.55$	$\alpha_{13,T}^{jjjj} > 0.55$	$\alpha_{14}^{jjjj} > 0.55$	$\alpha_{14,T}^{jjjj} > 0.55$
LM2	8	78	18	136
LM3	12	127	30	239
LM4	11	123	23	233
LM5	5	51	11	90
LM6	4	40	9	68
LM7	0	5	1	10
LM8	3	22	40	8
LM9	1	10	3	27

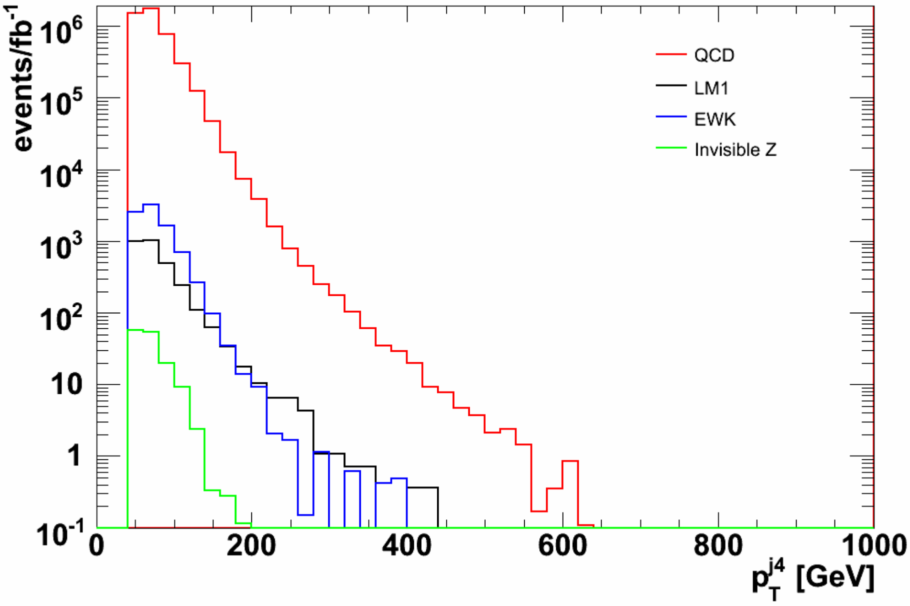

Figure 6.17: p_T distribution of the fourth jet

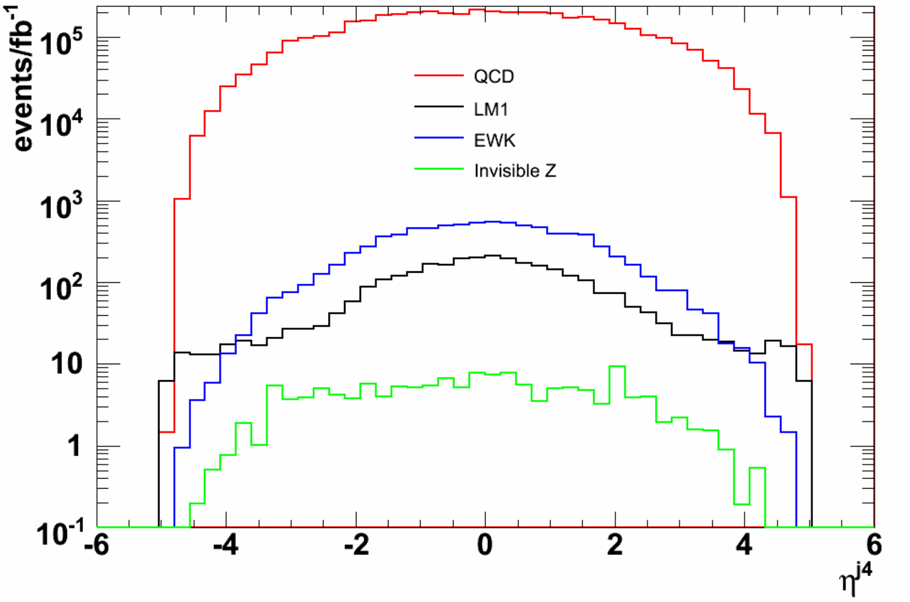

Figure 6.18: η distribution of the fourth jet

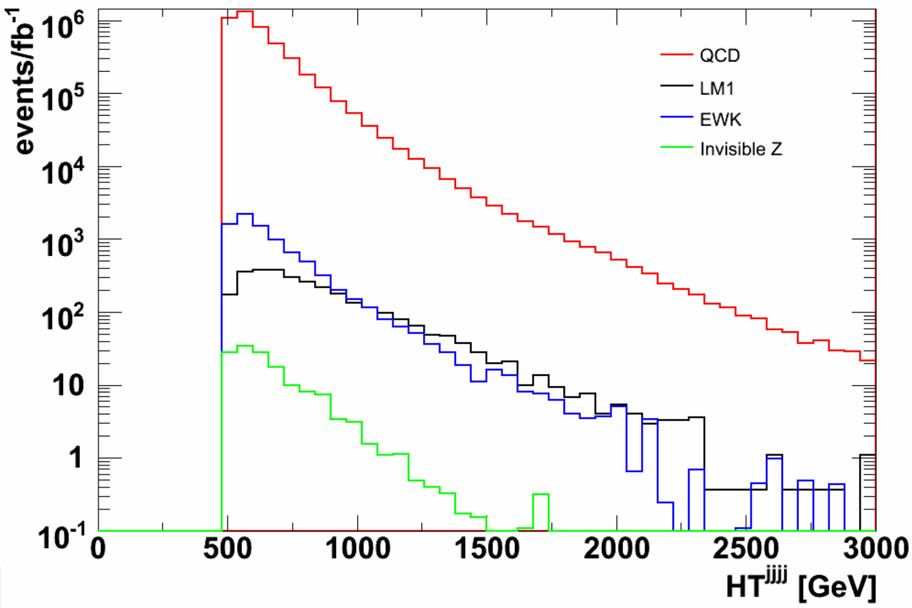

Figure 6.19: HT^{jjjj} distribution for SM background and SUSY LM1 4-jet events

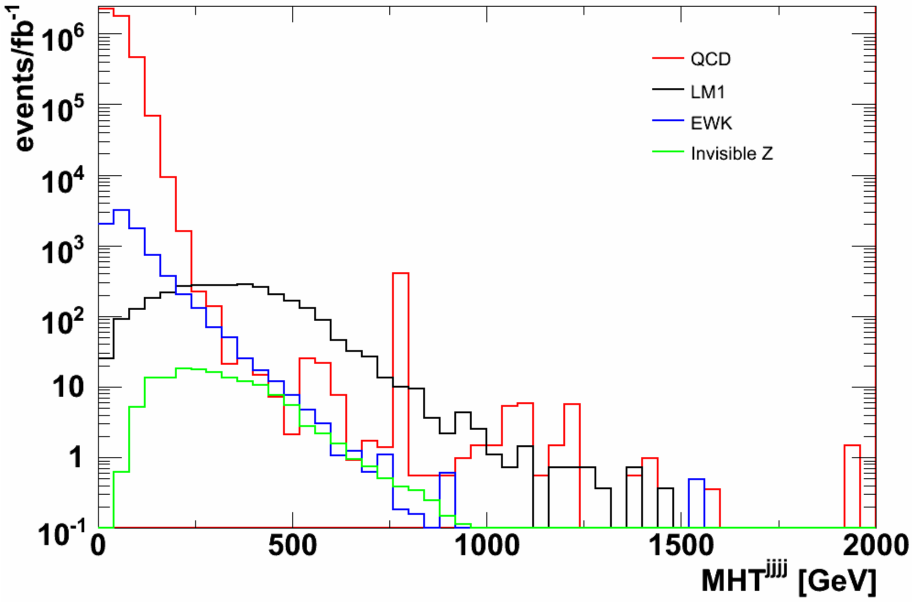

Figure 6.20: MHT^{jjjj} distribution for SM background and SUSY LM1 4-jet events

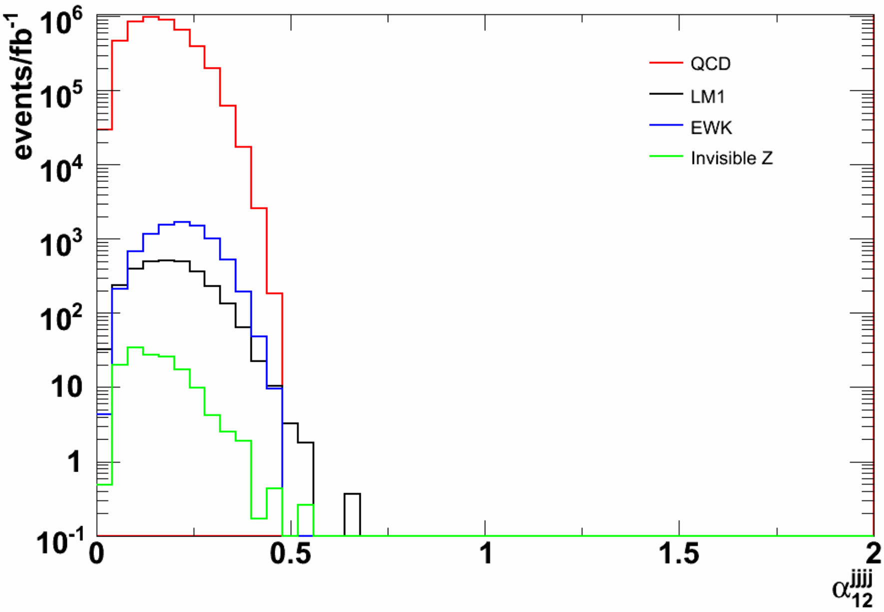

Figure 6.21: α_{12}^{jjjj} distribution for SUSY LM1 and SM background

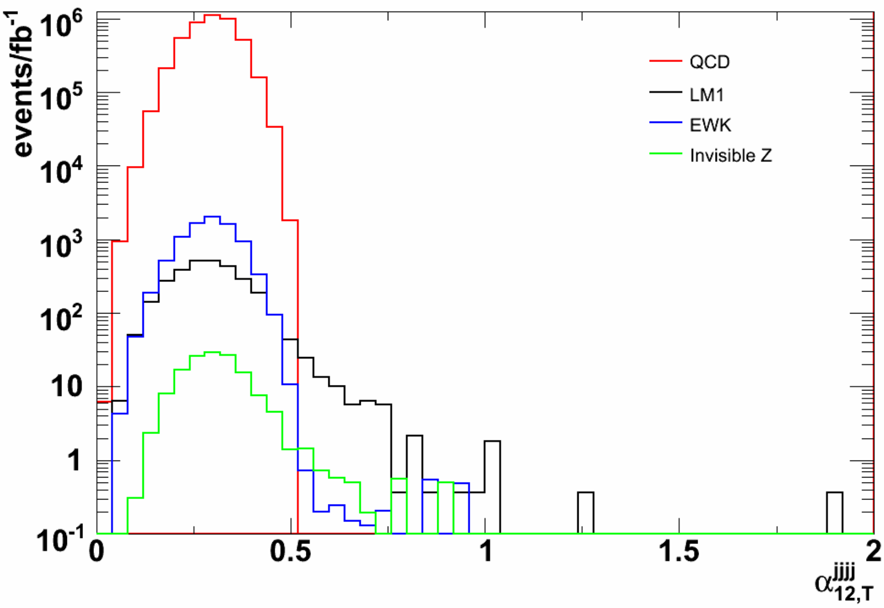

Figure 6.22: $\alpha_{12,T}^{jjjj}$ distribution for SUSY LM1 and SM background

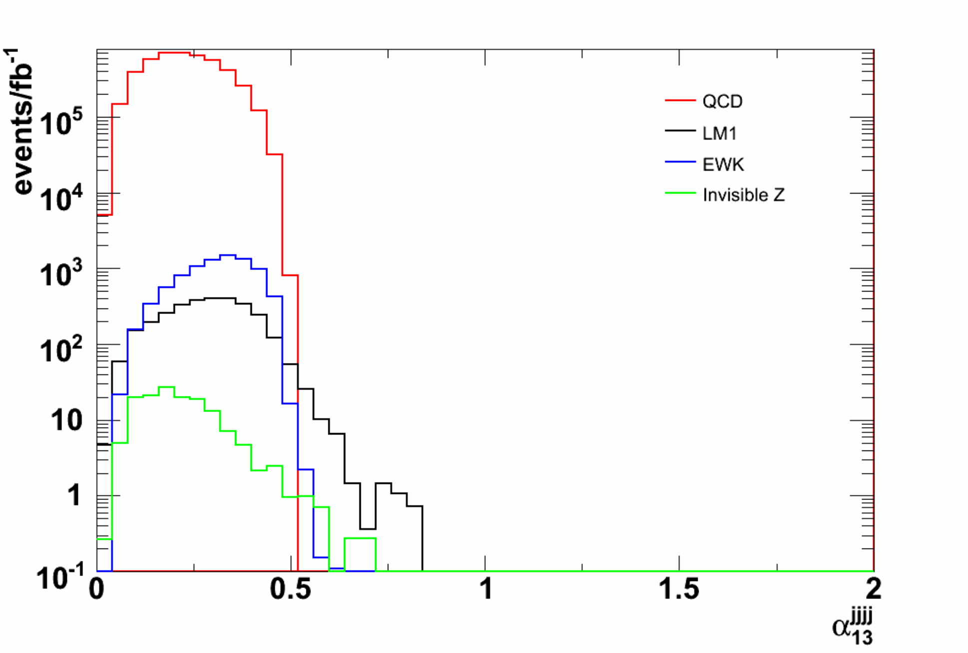

Figure 6.23: α_{13}^{jjjj} distribution for SUSY LM1 and SM background

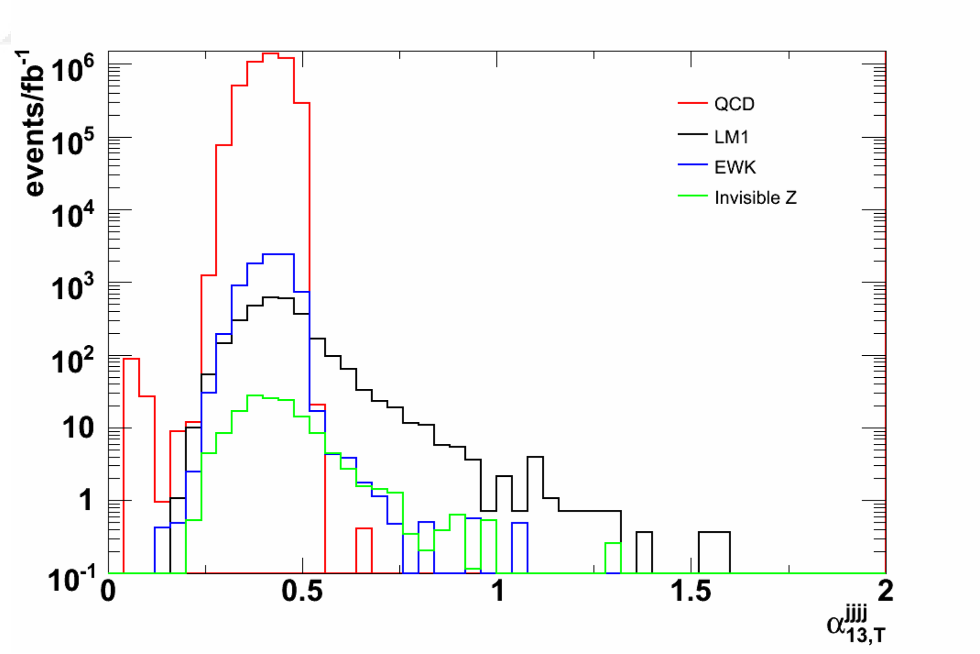

Figure 6.24: $\alpha_{13,T}^{jjjj}$ distribution for SUSY LM1 and SM background

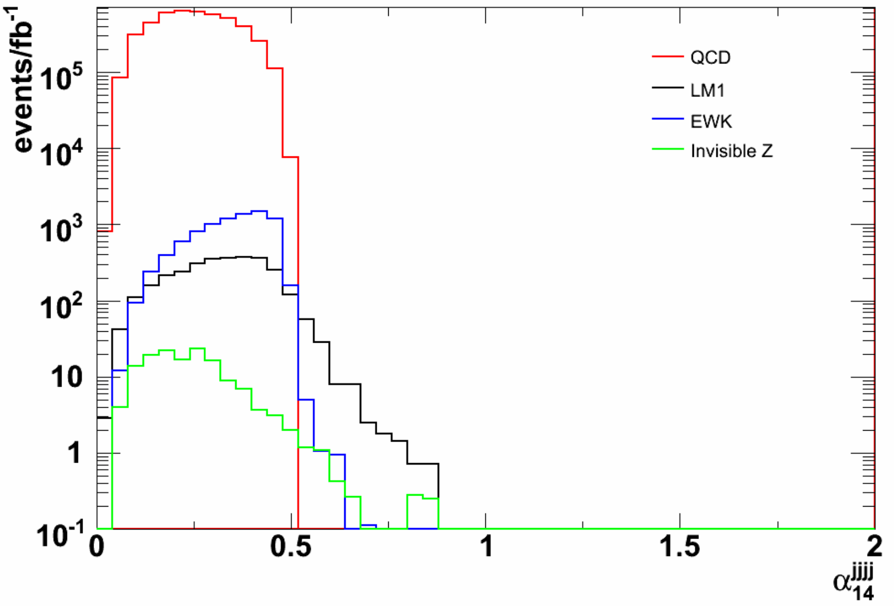

Figure 6.25: α_{14}^{jjjj} distribution for SUSY LM1 and SM background

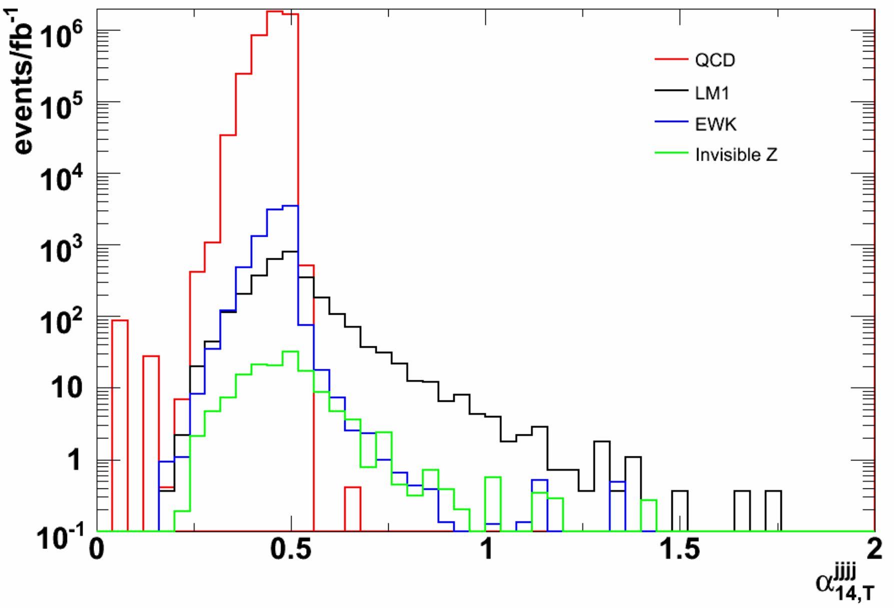

Figure 6.26: $\alpha_{14,T}^{jjjj}$ distribution for SUSY LM1 and SM background

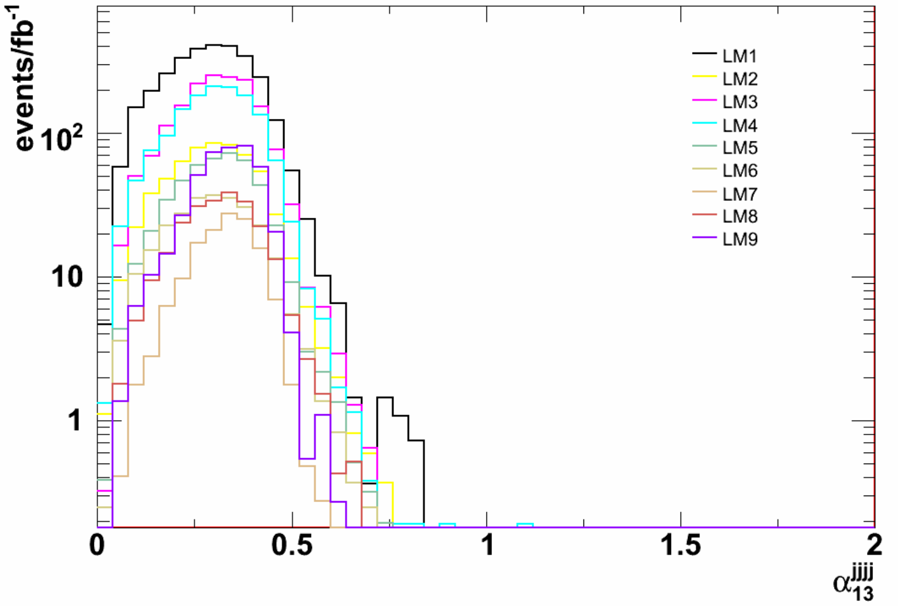

Figure 6.27: α_{13}^{jjjj} distribution for SUSY LM1-9 points

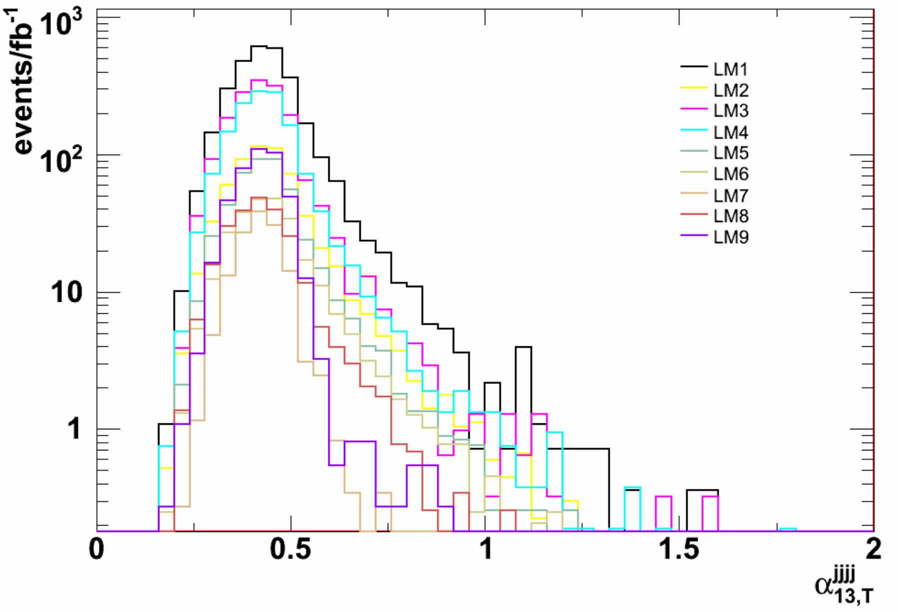

Figure 6.28: $\alpha_{13,T}^{jjjj}$ distribution for SUSY LM1-9 points

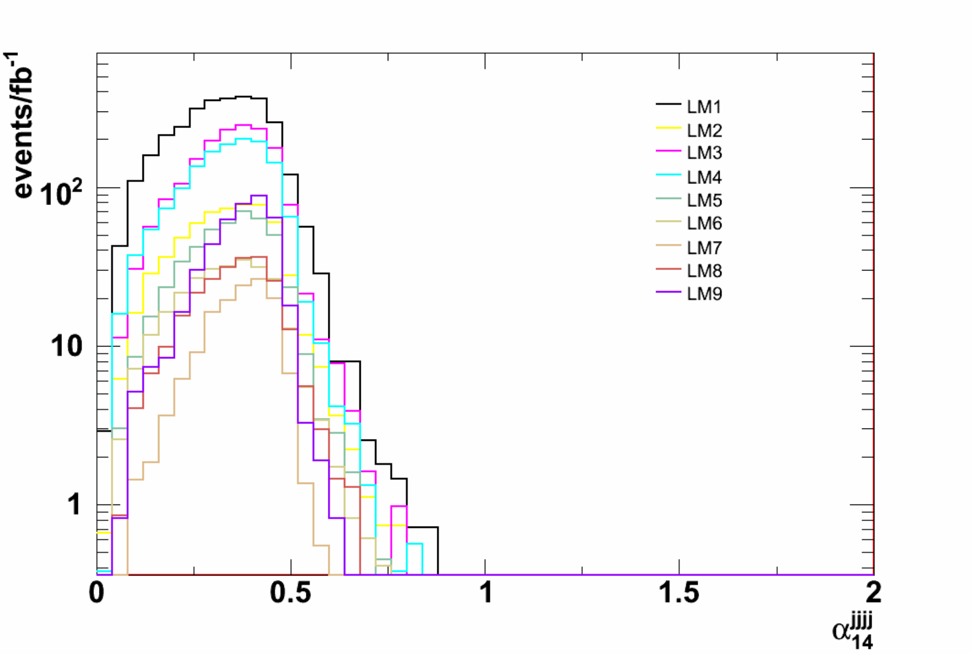

Figure 6.29: α_{14}^{jjjj} distribution for SUSY LM1-9 points

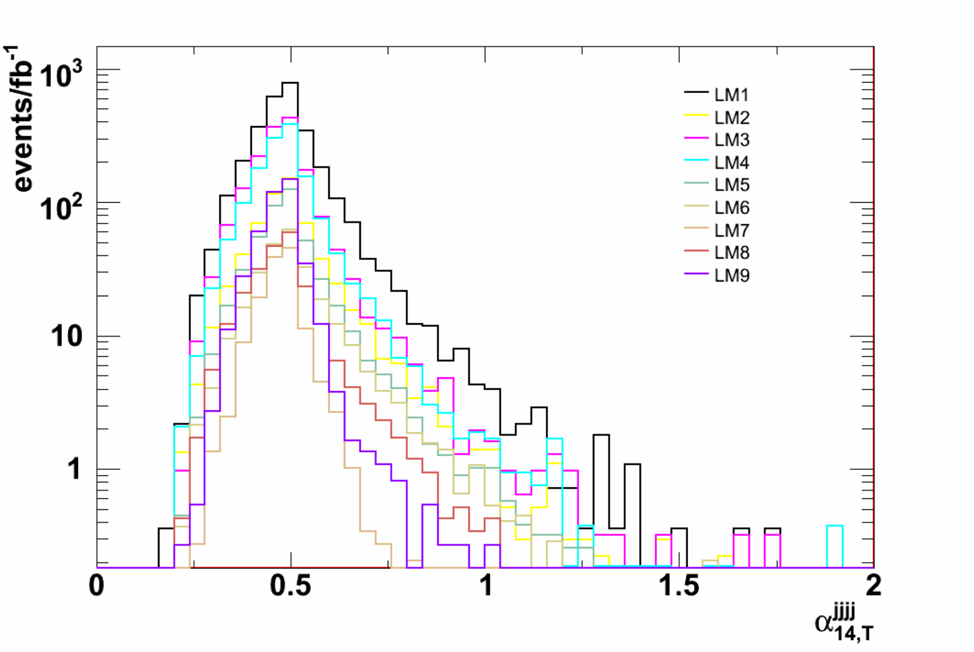

Figure 6.30: $\alpha_{14,T}^{jjjj}$ distribution for SUSY LM1-9 points

CHAPTER 7

CONCLUSIONS

This thesis showed that without using missing transverse energy, E_T^{miss}, which is carried by detector-escaping neutralino in the context of SUSY and already studied with CMS Physics TDR with number of jets bigger than or equal to 3 [27], it is possible to discriminate SUSY signal from SM background in di-jet decay channel with α^{jj} and α_T^{jj} variables. SUSY signal enriched region was found to be in both $\alpha^{jj} > 0.55$ and $\alpha_T^{jj} > 0.55$ and SUSY signal depleted region is that reverse. Another alternative background suppression region is discussed with the combination of $\alpha_T^{jj} > 0.55$ and $\Delta\phi^{jj} < \frac{2\pi}{3}$, wherein all QCD events can be dismissed. In addition to the discrimination power of alphas, these variables are also observed to be highly effective in signal to background optimization and the S/B ratios are calculated to be greater than 5.0 in all cases and significance is greater than 40.0 in all uses of cuts as well. Among LM2-9 SUSY signal points, it was shown that LM4, LM3, and LM2 can also be studied with alpha variables even they have smaller statistics than LM1 and LM7 can be excluded such that there yields no signal with standard alpha cuts discussed in the text.

The extension of di-jet study to 3-jet case with alpha variables is found to be very motivating in terms of handling high S/B and significance values. This thesis showed that the cuts necessary to reject all QCD events should be with $\alpha_{13}^{jjj} > 0.55$, $\alpha_{13,T}^{jjj} > 0.55$, $\alpha_{23}^{jjj} > 0.60$, and $\alpha_{23,T}^{jjj} > 0.65$. For α_{23}^{jjj} and $\alpha_{23,T}^{jjj}$ variables, the cut values are found to be greater than 0.55 value as being one important difference from di-jet study. In all these cuts, S/B ratios are found to be greater than 6.5 and significance values are shown to be greater than 25. Useful prospect of alpha variables defined for di-jet case in terms of signal-background separation has successfully extended to 3-jet event decay channel for SUSY, where one can easily define signal enriched and depleted regions for SUSY searches with three leading jets resulted from squark-gluino production by using the alpha variables and their corresponding cuts. Further, 3-jet alpha variables can be associated with other SUSY benchmark points like LM2, LM3, and LM4, but not having higher S/B and SUSY signal yielding events as it is found with LM1 point.

The use case of alpha variables with 4-jet event topology is still motivating in terms of high S/B values. It was shown that α_{13}^{jjjj} >0.55, $\alpha_{13,T}^{jjjj}$ >0.55, α_{14}^{jjjj} >0.55, and $\alpha_{14,T}^{jjjj}$ >0.55 cuts are still capable of discriminating SUSY signal from SM backgrounds. However, cuts of normal alphas, α_{13}^{jjjj} >0.55 and α_{14}^{jjjj} >0.55 are found to be as not powerful as cuts of transverse alphas concerning less numbers of SUSY LM1 signal events surviving after cuts on normal alphas. In all four alpha cuts, S/B ratios are found to be greater than 8 and significance values are greater that 16 (if we would exclude α_{13}^{jjjj} >0.55 cut, significance values will be greater than 25).

Having showed the discriminating power of alpha variables with di-jet, 3-jet, and finally with 4-jet event decay channels, it can be strongly inferred that use of alpha variables can be extended to multi-jet system trivially, once transverse momentum spectrums are well-defined by an appropriate CMS physics trigger. Therefore, n-jet system can also be a clear signature for SUSY searches in the fully hadronic channel with signal-background separation power of alpha variables.

REFERENCES

[1] D. J. Griffiths, *Introduction to Elementary Particles* (John Wiley and Sons, New York, 1987).

[2] W. N. Cottingham and D. A. Greenwood, *An Introduction to the Standard Model of Particle Physics* (Cambridge University Press, New York, 2007).

[3] B. R. Martin and G. Shaw, *Particle Physics* (John Wiley and Sons, New York, 1997).

[4] K. Gottfried and V. F. Weisskopf, *Concepts of Particle Physics, Volume II* (Oxford University Press, New York, 1986).

[5] Particle Data Group (PDG), http://pdg.lbl.gov/pdg.html, visited on November 13, 2008.

[6] F. Halzen and A. D. Martin, *Quarks and Leptons: An Introductory Course in Modern Particle Physics* (Wiley Text Books, New York, 1984).

[7] S. Glashow, Nucl. Phys. **B22** (1961) 579; S. Weinberg, Phys. Rev. Lett. **19** (1967) 1264; A. Salam, in Elementary Particle Theory, edited by N. Svartholm, (Almquist and Wiksell, Stockholm, 1968).

[8] P. Langacker, *hep-ph/0304186 v1* (2003).

[9] L. D. Faddeev and V. N. Popov, *Phys. Lett.* **B25** (1967) 29.

[10] R. K. Ellis, W. J. Stirling, B. R. Webber, *QCD and Collider Physics* (Cambridge University Press, New York, 1996).

[11] H. Baer and X. Tata, *Weak Scale Supersymmetry* (Cambridge University Press, New York, 2006).

[12] Y. Golfand and E. Likhtman, *JETP Lett.* **13**, 323 (1971); D. Volkov and V. Akulov, *Phys. Lett.* **B46**, 109 (1973).

[13] J. Wess and B. Zumino, *Nucl. Phys.* **B70**, 39 (1974).

[14] S. P. Martin, *hep-ph/9709356v5* (2008).

[15] P. West, *Introduction to Supersymmetry and Supergravity* (World Scientific, Philadelphia, 1986).

[16] J. Wess and J. Bagger, *Supersymmetry and Supergravity* (Princeton University Press, New Jersey, 1992).

[17] S. Weinberg, *The Quantum Theory of Fields, Volume III: Supersymmerty* (Cambridge University Press, New York, 2000).

[18] M. J. Ramsey-Musolf and S. Su, *hep-ph/0612057v1* (2008).

[19] M. E. Peskin, *hep-ph/0801.1928v1* (2008).

[20] I. J. R. Aitchison, *hep-ph/0505105v1* (2005).

[21] J. A. Bagger, *hep-ph/9604232v2* (1996).

[22] J. Terning, *Modern Supersymmetry* (Oxford University Press, New York, 2006).

[23] H. E. Haber, *hep-ph/9306207v1* (1993).

[24] M. Drees, *hep-ph/9611409v1* (1996).

[25] X. Tata, *hep-ph/9706307v1* (1997).

[26] H.P. Nilles, Phys. Rept. **110** (1984).

[27] CMS Collaboration, G.L. Bayatian et al., *CMS physics: Technical Design Report, Volume I*, CERN-LHCC-2006-001 (2007).

[28] LHC Project, http://lhc.web.cern.ch/lhc, visited on December 28, 2008.

[29] CERN, http://www.cern.ch, visited on December 23, 2008.

[30] The LEP Working Group for Higgs Boson Searches (ALEPH, DELPHI, L3 and OPAL Collaborations), *hep-ex/0306033* (2003).

[31] Fermilab D0 and CDF Collobarations Higgs Conference Note,

http://www-d0.fnal.gov/Run2Physics/WWW/results/prelim/HIGGS/H64, visited on December 12, 2008.

[32] CDF Collaboration, *Phys. Rev. Lett.* **74**, (1995) 2626.

[33] D0 Collaboration, *Phys. Rev. Lett.* **74**, (1995) 2632.

[34] LHC Design Report Volume I - III,

http://ab-div.web.cern.ch/ab-div/Publications/LHC-DesignReport.html, visited on December 21, 2008.

[35] CMS (Compact Muon Solenoid), http://cms.cern.ch/, visited on January 12, 2009.

[36] CMS Collaboration, *The CMS Physics Technical Design Report, Volume II*, CERN/LHCC 2006-001 (2006).

[37] CMS Collaboration, *The Tracker Project Technical Design Report*, CERN/LHCC 98-006 (1998).

[38] CMS Collaboration, *The Electromagnetic Calorimeter Technical Design Report*, CERN/LHCC 97-033 (1997).

[39] CMS Collaboration, *The Hadron Calorimeter Technical Design Report*, CERN/LHCC 97-031 (1997).

[40] CMS Collaboration, *The Muon Project Technical Design Report*, CERN/LHCC 97-32 (1997).

[41] CMS Collaboration, *CMS TriDAS Project, Technical Design Report Volume 1: The Trigger Systems*, CERN/LHCC 97-32 (1997).

[42] CMS Collaboration, *The Computing Project*, CERN-LHCC-2005-023 (2005).

[43] Worldwide LHC Computing Grid,
http://lcg.web.cern.ch/LCG/, visited on December 28, 2008.

[44] *LHC Computing Grid Technical Design Report*, CERN-LHCC-2005-024 (2005).

[45] Framework and Event Data Model Offline Guide,
https://twiki.cern.ch/twiki/bin/view/CMS/SWGuideFrameWork, visited on December 11, 2008.

[46] The ROOT System Home Page, http://root.cern.ch/, visited on December 23, 2008.

[47] CMS Data and Workload Management,
https://twiki.cern.ch/twiki/bin/view/CMS/DMWM, visited on December 12,2008.

[48] Physics and Data Quality Monitoring,
https://twiki.cern.ch/twiki/bin/view/CMS/DQMInfrastructure, visited on December 26, 2008.

[49] CMS Event Generation Offline Guide,
https://twiki.cern.ch/twiki/bin/view/CMS/SWGuideEventGeneration, visited on December 23, 2008.

[50] CMS Full Simulation Offline Guide,
https://twiki.cern.ch/twiki/bin/view/CMS/SWGuideSimulation, visited on December 23, 2008.

[51] S.Agostinelli et al., *Nucl. Instrum. Meth.* **A506**, 250 (2003).

[52] CMS Full Simulation Offline Guide,
https://twiki.cern.ch/twiki/bin/view/CMS/SWGuideFastSimulation, visited on December 2, 2008.

[53] CMS L1 Trigger Offline Software,
https://twiki.cern.ch/twiki/bin/view/CMS/SWGuideL1Trigger, visited on December 23, 2008.

[54] CMS: Calibration and Alignment,
https://twiki.cern.ch/twiki/bin/view/CMS/SWGuideCalAli, visited on December 29, 2008.

[55] CMS: Reconstruction Offline Guide,
https://twiki.cern.ch/twiki/bin/view/CMS/Reco, visited on December 13, 2008.

[56] CMS Physics Analysis Tools Offline Guide,
https://twiki.cern.ch/twiki/bin/view/CMS/SWGuidePhysicsTools, visited on November 26, 208.

[57] Iguana Home Page,
http://iguana.web.cern.ch/iguana/, visited on December 17, 2008.

[58] CMS PAT - Physics Analysis Toolkit,

https://twiki.cern.ch/twiki/bin/view/CMS/SWGuidePAT, visited on January 10, 2009.

[59] CMS PAT - Physics Analysis Toolkit Layers,

https://twiki.cern.ch/twiki/bin/view/CMS/SWGuidePATLayer, visited on November 10, 2008.

[60] Tools for SUSY analysis in the PAT,

https://twiki.cern.ch/twiki/bin/view/CMS/SusyPat, visited on January 1, 2009.

[61] Cross-Cleaning for SUSY analysis in the PAT,

https://twiki.cern.ch/twiki/bin/view/CMS/SusyPatCrossCleaner, visited on January 1, 2009.

[62] CSA07 Twiki Page,

https://twiki.cern.ch/twiki/bin/view/CMS/CSA07, visited on January 10, 2009.

[63] CMS CAF (CERN Analysis Facility),

https://twiki.cern.ch/twiki/bin/view/CMS/CAF, visited on January 10, 2009.

[64] Pythia Home Page,

http://home.thep.lu.se/ torbjorn/Pythia.html, visited on October 11, 2008.

[65] Prospino Home Page,

http://www.ph.ed.ac.uk/ tplehn/prospino/, visited on October 16, 2008.

[66] ALPGEN Home Page,

http://mlm.home.cern.ch/mlm/alpgen/, visited on October 27, 2008.

[67] Twiki documenting the SUSY activities at CAF,

https://twiki.cern.ch/twiki/bin/view/CMS/SusyCaf, visited on January 13, 2009.

[68] CMS SUSY CSA07 Merged Skims,

https://twiki.cern.ch/twiki/bin/view/CMS/SUSYBSMSkims, visited on November 12, 2008.

[69] L. Randall and D. Tucker-Smith, *hep-ph/0806.1049v1* (2008).

[70] H. Flaecher, J. Jones, T. Rommersckirchen and M. Stoye, *SUSY search with dijet events*, CMS AN-2008/071.

APPENDIX A

SUSY PAT EVENT SELECTORS

Table A.1: SUSY PAT Event selectors and corresponding variables.

Event selector name	Selection of interest
AlphaSelector	α variable
BJetEventSelector	b-tagged jets
ChargedFractionSelector	Minimum charged event fraction
DiLeptonEventSelector	2 leptons with p_T, η, and isolation of each
DPhiEventSelector	Difference in azimuth between two jets
EMFractionSelector	Electromagnetic fraction (F_{em}) of an event
HemisphereSelector	Hemisphere axis, $\Delta\phi$
HLTEventSelector	Specific high level trigger bits
HTEeventSelector	Scalar sum $E_T s$ of all jets
JetEventSelector	Cut on number, E_T, η, and F_{em} of jets
MetEventSelector	Calorimeter missing E_T, E_T^{miss}
MetJetEventSelector	E_T^{miss}+jet topology
MHTEventSelector	Negative vectorial sum $E_T s$ of all jets
MuonEventSelector	Cut on number, p_T, η, and isolation of muons
MaxNumJetsEventSelector	Cut on maximum number of jets (n+1 jet)
PrimaryVertexEventSelector	Primary vertex (at least one)

APPENDIX B

CMS SUSY GROUP SKIMS

Table B.1: CMS SUSY Group Skim Table.

Skim	Primary Datasets	Description
ElectronPhoton	PDElectron	Searches with electromagnetic object
ElectronPhoton	PDPhoton	Searches with electromagnetic object
ElectronPhoton-HLT	PDElectron	Searches with electrons
ElectronPhoton-HLT	PDPhoton	Searches with photons
JetMet	PDJetMet	Hadronic searches
JetMet	PDTau	Hadronic searches
JetMet-HLT	PDJetMet	Hadronic searches
Muon	PDMuon	Searches with muon
Muon-HLT	PDMuon	Searches with muon
MuonsHits	PDMuon	HSCP and TeV Muon
MuonHits	PDJetMet	HSCP and TeV Muon

Table B.2: CMS SUSY Group Skim Table (con't).

Skim	HLT Paths
ElectronPhoton	HLT1Electron, HLT1ElectronRelaxed, HLT2Electron, HLT2ElectronRelaxed, HLTXElectron1Jet, HLTXElectron2Jet, HLTXElectron3jet, HLT1EMHighEt, HLT1EMVeryHighET, HLTXElecronMuon, HLTXElectronMuonRelaxed
ElectronPhoton	HLT1PhotonRelaxed, HLT2PhotonRelaxed, HLT1Photon, HLT2Photon
ElectronPhoton -HLT	HLT1Electron, HLT1ElectronRelaxed, HLT2Electron, HLT2ElectronRelaxed, HLT1EMHighEt, HLT1EMVeryHighEt, HLTXElectron1Jet, HLTXElectron2Jet, HLTXElectronMuon, HLTXElectronMuonRelaxed, HLT1Photon, HLT1PhotonRelaxed, HLT2Photon, HLT2PhotonRelaxed, HLT1jet, HLT2jet, HLT3jet, HLT4jet, HLT1jet1MET, HLT2jet1MET,HLT1MET1HT, HLT2jetAco, HLT1jet1METAco, HLTS2jet1METNV, HLTS2jet1METAco, CandHLTSjet1MET1Aco, CandHLTSjet2MET1Aco, CandHLTS2jetAco, HLT1Tau
JetMet-HLT	HLT1MET, HLT1jet, HLT2jet, HLT3jet, HLT4jet, HLT2jet1MET, HLT1jet1MET, HLT1MET1HT, HLT2jetAco, HLT1jet1METAco, HLT1MET, HLT1jet, HLT2jet, HLT3jet, HLT4jet, HLT2jet1MET, HLTS2jet1METNV, HLTS2jet1METAco, CandHLTSjet1MET1Aco, CandHLTSjet2MET1Aco, CandHLTS2jetAco
Muon	HLTXMuonJets, HLT2MuonNonIso, HLT1MuonIso, HLT1MuonNonIso, HLT2MuonSameSign, HLTXElectronMuon, HLTXElectronMuonRelaxed
Muon-HLT	HLT1MuonIso, HLT2MuonIso, HLT2MuonNonIso, HLT2MuonSameSign, HLTXMuonJets, HLTXElectronMuon, HLTXElectronMuon Relaxed
MuonsHits	HLT1MuonIso, HLT1MuonNonIso, HLT2MuonNonIso, HLT2MuonSameSign
MuonHits	HLT1MET, HLT1jet1MET, HLT2jet1MET, HLT3jet1MET, HLT4jet1MET, HLT1MET1HT, HLT2jetvbfMET, HLT2jetAco, HLT1jet1METAco, HLTS2jet1METNV, HLTS2jet1METAco, CandHLTSjet1MET1Aco, CandHLTSjet2MET1Aco, CandHLTS2jetAco

APPENDIX C

KINEMATICS OF ALPHA VARIABLE

After the decay of a particle, the relativistic energy and momentum of the resulting particles is equal to that of original particle. This enables to work on the energy and momentum of the original particle, and hence its mass.

For massless final state particles in di-jet case ($m_1 = m_2 = 0$):

$$E^2 = m^2c^4 + \vec{p}^2c^2,$$

$$E^2 = \vec{p}^2,$$

$$E = |\vec{p}|. \tag{C.1}$$

Momentum of proton-proton initial state in the frame of detector equals to 0. Since, colliding protons have equal and opposite momentums.

$$\vec{p}_1 + \vec{p}_2 = 0,$$

$$\vec{p}_1 = -\vec{p}_2. \tag{C.2}$$

Additionaly,

$$\vec{p}_1 \cdot \vec{p}_2 = p_1 p_2 cos\varphi, \tag{C.3}$$

where φ is the angle between two momentum vectors. Using the substitutions $\vec{p}_1 = -\vec{p}_2$ and $p_1 = p_2$:

$$-\vec{p}_1 \cdot \vec{p}_1 = p_1 p_1 cos\varphi,$$

$$-\vec{p}_1^2 = p_1^2 cos\varphi,$$

$$\varphi = \pi. \tag{C.4}$$

And since we have (C.1), $E_1 = |\vec{p}_1| = |\vec{p}_2| = E_2$, the invariant mass of the two jets (Eq. 5.3), di-jet case, can be obtained as:

$$M_{inv}^{jj} = \sqrt{2E^{j1}E^{j2}(1 - cos\phi)}, \tag{C.5}$$

where ϕ is the angle between two jets in the final state of proton-proton collision. Finally, the form of α proceeds from Eq. 5.2 as:

$$\alpha = \frac{ET^{j2}}{\sqrt{2E^{j1}E^{j2}(1 - cos\phi)}}. \tag{C.6}$$

Hence, conservation of momentum principle hints that jets are produced back to back for a two-body final state, $\phi = \pi$:

$$\alpha = \frac{1}{2}\frac{E_T^{j2}}{E^{j2}}, \tag{C.7}$$

which has a maximum of 0.5 and a minimum of zero for final state particles ejected down the beam pipe, since $E_T \leq E$ and $E_T = E$ provided that $p_z = 0$.

Here are some useful kinematic equations to understand the relation between E_T and E.

$$p_T = \sqrt{p_x^2 + p_y^2} = psin\theta, \tag{C.8}$$

where, θ is the polar angle of cylindrical coordinate and

$$E_T^2 = m^2 + p_x^2 + p_y^2 = E^2 - p_z^2. \tag{C.9}$$

E_T can also be expressed in terms of E by using rapidity, y as:

$$E = E_T coshy \tag{C.10}$$

with

$$y = \frac{1}{2}ln\frac{E + p_z}{E - p_z}. \tag{C.11}$$